DEPARTAMENTO DE ASTROFÍSICA

Universidad de La Laguna

Spectroscopic and photometric characterization of primitive asteroid collisional families

Memoria que presenta
David Morate González
para optar al grado de
Doctor por la Universidad de La Laguna.

INSTITUTO Đ ASTROFISICA Đ CANARIAS
abril de 2018

Examination date: 25th May, 2018
Thesis supervisors: Julia de León Cruz & Javier Licandro Goldaracena

"Dan: It's the size of Texas, Mr President.
President: Dan, we didn't see this thing coming?
Dan: Well, our object collison budget's a million dollars, that allows us to track about 3% of the sky, and beg'n your pardon sir, but it's a big-ass sky."
Michael Bay. Armageddon.

Agradecimientos

Llegar hasta el final de este recorrido me hace pensar en todos los años que han pasado, desde el Santa Catalina hasta el IAC, pasando por el San José, la UVA y la UIB, y al mirar atrás aparece tal infinidad de personas que fueron marcando mi camino, que probablemente no alcance a mencionarlas a todas. Y alguien se quedaría fuera. Pero intentaré darles la importancia que merecen.

Primeramente, quiero agradecer a la Dra. Julia de León y al Dr. Javier Licandro por darme la oportunidad de trabajar con ellos en el IAC, por todo lo que me han enseñado, por ayudarme a llegar hasta aquí, y por considerarme un compañero de trabajo, además de su estudiante. Y por la paciencia que han tenido conmigo para que lleve a buen puerto esta tesis. ¡Ah! ¡Y por no usar nunca el látigo de siete puntas! (aún me pregunto dónde lo guardan...).

A todos los miembros del Grupo de Sistema Solar del IAC, (y a los de fuera también): Marcel, Juanlu, Vania, Noe, Humberto, Víctor.

Al grupo de planetarias del Observatorio Nacional de Rio, en especial al Dr. Jorge Carvano. Y a los alumnos de la pos-graduación, por tratarme como a uno más el tiempo que pasé allí. Especialmente a Mario y a Bita, por acogerme en mi primera visita a Brasil. Y cómo no, a Pli. Me alegro muchísimo de haberte conocido :)

No podría olvidar aquí a la Dra. Alicia Sintes, investigadora principal del GRG de la Universitat de les Illes Balears, quien, en 2013, me abrió las puertas del mundo de la investigación. Gracias, Alicia, por creer que yo era capaz de dedicarme a esto.

A Lourdes, Eva, e Irene, porque sin ellas la vida en el IAC habría sido bastante más complicada.

A todos los compañeros del Instituto de Astrofísica de Canarias y allegados que han sido parte de estos cuatro maravillosos años, por todos los buenos momentos que hemos pasado juntos. Sergio, Isma, Torni, Sara, Javi, Víctor, Rebe, Awe, Pato, Ernest, Dani, Patri, Ray, Aguado: mil gracias por haber estado ahí cuando lo necesité. Y muy en especial a Ferragamo: has sido todo lo que se puede esperar de un buen amigo, y más. Espero poder algún día felicitarte por una liga del Napoli, o que tu puedas hacer lo propio cuando el Pucela vuelva a primera :D (no sé yo cuál de las dos es más difícil...).

Al Pirata Brasileiro y al Luz Oscura, hogares nocturnos de estas ovejas descarriadas. Y a Rafa Pirata :P

A Suzane, por haber caminado a mi lado durante gran parte de este viaje.

A mis amigos de toda la vida: Maestu, Miki, y Monsalve. Es un placer haber compartido 25 años con vosotros. Porque vernos de guindas a brevas y

sentirse igual que siempre no tiene precio. Y porque vosotros me enseñasteis lo que es la amistad.

A los amigos de la UVA, en especal a Reme, y al Dr. Juan Borge (todo lo que tienes de buen amigo, lo tienes de malo jugando al fútbol). Todos grandes culpables de que haya llegado a escribir una tesis doctoral.

A todos mis profesores, desde preescolar hasta el Máster, porque sin personas que me enseñaran, no habría aprendido nada. En especial a Mª Carmen, que en paz descanse, por enseñarme a sumar y a divertirme aprendiendo. Y al Pelos, por hacerme la pregunta que me hizo querer ser científico.

A Mila, Julio, y Teo, por recibirme en Mallorca con los brazos abiertos y estar ahí siempre que os necesité.

Por último, gracias mamá, papá, y hermanita. A vosotros no os tengo que explicar por qué.

Aunque mi nombre esté en la portada, esta tesis también es de todas vosotras.

David Morate González, La Laguna, Mayo de 2018

Resumen

El estudio de asteroides cercanos a la Tierra, o NEAs (por sus siglas en inglés *near-Earth asteroids*), es de gran importancia por tres motivos principales. Primero, suponen un riesgo de impacto para la Tierra, y los daños derivados de una posible colisión dependerán de la velocidad de impacto, el tamaño, y la composición del objeto. Segundo, por su proximidad, son objetos accesibles para la visita de posibles misiones espaciales. Y tercero, por la posibilidad de utilizarlos como fuente de recursos "in situ" de cara al futuro (o ISRU, por sus siglas en inglés *in situ resource utilization*), que permitirían el establecimiento asequible de la exploración y operaciones extraterrestres al minimizar los materiales que se requerirían transportar desde la Tierra.

Las misiones OSIRIS-REx (NASA, lanzada en el año 2016) y Hayabusa 2 (JAXA, lanzada en el año 2014) visitarán dos NEAs primitivos: (101955) Bennu y (162173) Ryugu, respectivamente. Estas misiones tienen como objetivo principal recolectar material de la superficie de dichos objetos y traerlo de vuelta a la Tierra para su análisis. Estos asteroides son considerados primitivos debido a su bajo albedo y composición carbonácea, inferida a partir de sus características espectrales, similares a aquellas de las condritas carbonáceas (los meteoritos más primitivos y que menor evolución han sufrido desde las etapas primigenias del Sistema Solar). Varios estudios dinámicos sugieren que la población originaria de estos NEAs se encuentra en la parte interna del cinturón principal de asteroides, en el grupo de familias de bajo albedo y baja inclinación ($i < 8°$): el complejo Polana–Eulalia y las familias Erigone, Sulamitis y Clarissa.

Existe una escasez significativa de información a nivel composicional sobre las familias primitivas del cinturón principal, y por tanto, cualquier estudio dedicado, tanto espectroscópico como fotométrico, supondrá una contribución importante. Además, la conexión entre (101955) Bennu y (162173) Ryugu y las familias del cinturón interno es sugerente, pero no definitiva, y necesita confirmación y estudios detallados. El objetivo, por tanto, de esta tesis, es estudiar y caracterizar las fuentes más probables de estos NEAs primitivos, así como proporcionar información sobre otras posibles fuentes de asteroides primitivos a lo largo del cinturón principal.

Los trabajos de análisis en los que se basa esta tesis son una continuación directa de los estudios comenzados con el complejo Polana–Eulalia, la parte de bajo albedo ($p_V < 0.1$) de la familia Nysa, situada en la región interna del cinturón de asteroides. Este estudio previo al trabajo de esta tesis mostró que el complejo Polana–Eulalia estaba compuesto, en su mayor parte, por asteroides del tipo C y B (objetos primitivos), presentando homogeneidad en la muestra

obtenida.

Esta tesis es un compendio de tres artículos, donde se han utilizado dos técnicas distintas: (1) a través de espectroscopía en el rango espectral visible (0.5–0.9 μm), y con datos del Gran Telescopio Canarias (GTC), se analizó la composición de tres familias de asteroides situadas en la parte interna del cinturón principal (Erigone, Sulamitis y Clarissa); y (2) a través de los datos de colores infrarrojos (0.9–2.4 μm) en el catálogo MOVIS (Moving Objects from VISTA), se analizaron las familias de asteroides presentes en dicho catálogo.

El estudio de la familia colisional de Erigone mostró que un 87% de los objetos observados tienen espectros típicos de asteroides primitivos, consistentes con el espectro de (163) Erigone, el cuerpo progenitor. Además, encontramos un alto porcentaje de miembros de la familia (50%) que poseen características espectrales relacionadas con la presencia de minerales hidratados en su superficie. A partir del análisis de las familias Sulamitis y Clarissa, las más pequeñas del grupo de posibles fuentes de Bennu y Ryugu, encontramos que un 60% de los asteroides observados de la familia de Sulamitis muestran signos de alteración acuosa en sus superficies, al contrario que la mayoría de los asteroides de la familia Clarissa, que no presentan signos de dicha alteración. De acuerdo a los espectros en el rango visible obtenidos para los miembros de las familias primitivas de la región interna del cinturón principal estudiadas hasta ahora, podemos diferenciar dos grupos: los tipo-Polana (Polana y Clarissa), que presentan espectros sin bandas de absorción, taxonómicamente homogéneos, y sin alteración acuosa; y los tipo-Erigone (Erigone y Sulamitis), que presentan mayor diversidad taxonómica en sus espectros, y una gran mayoría de espectros con la banda de alteración acuosa. El estudio llevado a cabo a partir de los datos infrarrojos del catálogo MOVIS permitió caracterizar 43 familias a lo largo de todo el cinturón principal: 15 primitivas, 19 rocosas, y 9 que se definieron como mezclas de las composiciones teóricas propuestas.

Los resultados de esta tesis constituyen una de las contribuciones más significativas que se han realizado sobre el estudio composicional de las familias de asteroides primitivos. Además, las investigaciones sobre los orígenes más probables de los NEAs (101955) Bennu y (162173) Ryugu serán de gran ayuda a la hora de comprobar los modelos dinámicos que explican las rutas de transporte de asteroides desde el cinturón principal hasta la zona de los NEAs. Nuestros resultados serán especialmente relevantes para la interpretación de las imágenes y espectros que serán obtenidos "in situ" por las misiones espaciales OSIRIS-REx y Hayabusa 2 durante los encuentros con sus objetivos, proporcionando un contexto general a los datos producidos.

Summary

The study of near-Earth asteroids (NEAs) is very important, due to three main reasons. First, they pose an impact risk for Earth, and damage produced by a possible collision will depend on the speed of the impact, the size of the object, and its composition. Second, given their proximity, they are easy access targets for the visit of space missions. And third, these objects are possible sources of in-situ resources for future space missions (or ISRU, for in-situ resource utilization), that would enable the affordable establishment of extraterrestrial exploration and operations by minimizing the materials carried from Earth.

Space missions OSIRIS-REx (NASA, launched on 2016) and Hayabusa 2 (JAXA, launched on 2014) will visit two primitive NEAs: (101955) Bennu and (162173) Ryugu, respectively. The main goal of these missions is to collect a sample of surface material from these NEAs and bring it back to Earth for analysis. These asteroids are considered "primitive" due to their low albedo and carbonaceous composition, inferred from their spectral characteristics, similar to those of the carbonaceous chondrites (the most primitive meteorites, that have undergone almost no evolution since the early stages of the Solar System). Several dynamic studies suggest that these NEAs originate in the inner part of the main asteroid belt, within the low-albedo low-inclination families ($i < 8°$): the Polana–Eulalia complex, and the Erigone, Sulamitis, and Clarissa families.

There is a significant lack of compositional information for asteroids in the primitive families in the main belt, and therefore any spectroscopic or photometric survey in this sense will be a major contribution. The link between primitive NEAs and primitive families is suggestive but not definitive, so it needs confirmation and detailed study. The main objective of this thesis work is to study and characterize the most likely origin of (101955) Bennu and (162173) Ryugu, targets of the sample-return space missions OSIRIS-REx and Hayabusa 2, as well as to provide information about other possible sources of primitive asteroids throughout the main belt.

This thesis work is a direct follow-up of the studies on the Polana–Eulalia complex, the low-albedo ($p_V < 0.1$) part of the Nysa family, located in the inner region of the main belt. This initial study showed that the Polana–Eulalia complex is mainly composed of C- and B-type asteroids (primitive objects), presenting spectral homogeneity.

This thesis is a compendium of three papers, published in the Astronomy & Astrophyisics journal. Two different approaches to the analysis have been used: (1) through visible spectroscopy (0.5–0.9 μm), using data obtained with the Gran Telescopio Canarias (GTC), we analayzed three asteroid families located in the inner region of the main belt (Erigone, Sulamitis, and Clarissa); and

(2) through near-infrared photometry (0.9–2.4 μm) we analyzed the asteroid families observed in the MOVIS (Moving Objects from VISTA) catalog.

The results regarding the Erigone collisional family showed that, approximately, 87% of the observed objects have typical primitive asteroid spectra, consistent with the spectrum of (163) Erigone, the parent body. In addition, we found a significant percentage of family members (50%) with spectral features related to the presence of hydrated minerals on their surfaces. After the analysis of the Sulamitis and Clarissa families, the smallest of the possible NEAs sources, we found that about 60% of the observed asteroids in the Sulamitis family show signs of aqueous alteration on their surfaces, while almost all of the objects in the Clarissa family do not show any evidences of hydration. Also, according to the visible spectra obtained for the members of the primitive families in the inner main belt studied so far, we can differentiate between two groups: the Polana-like group (Polana and Clarissa), which presents homogeneous, featureless spectra in a continuum of slopes from blue to moderately red, and no aqueous alteration, and the Erigone-like group (Erigone and Sulamitis), showing a spectral diversity among primitive taxonomic classes and a majority of spectra with the aqueous alteration band. The study on the near-infrared data of the MOVIS catalog allowed us to characterize 43 families through the whole main belt: 15 primitive, 19 rocky, and 9 that were defined as "mixtures" of the proposed theoretical compositions.

The results of this thesis constitute one of the most significant contributions that have been made up to now to the compositional study of primitive asteroid families. Besides, the investigations about the most probable origins of NEAs (101955) Bennu and (162173) Ryugu will be of great help to test the dynamical models which explain the asteroidal transport routes from the main belt to the near-Earth space. Our results will be specially relevant for the interpretation of the images and spectra obtained in situ by the spacecrafts OSIRIS-REx and Hayabusa 2 during their encounters with their targets, placing the mission's data within the big picture of the evolutionary history of the Solar System.

Contents

Chapter 1

Introduction

Asteroids are irregularly-shaped bodies with no atmosphere orbiting the Sun, with sizes ranging from a few meters up to hundreds of kilometers. Nowadays these objects are thought to be the leftovers of the planetary formation processes, this is, fragments of bodies that never managed to acquire enough mass to accrete into a single planetary sized body. The major part of the asteroidal mass in the Solar System is located in between the orbits of Mars and Jupiter, in a region known as the main belt, which extends between 2.0 and 3.3 A.U. from the Sun. In this introductory chapter, we give a historical preamble, and then we present the state-of-the-art on asteroid research.

1.1 A peek at the history

In the year 1766, in a translation of the book *Contemplation de la Nature* by Charles Bonnet, the astronomer Johann Daniel Titius added the following text of his own:

> *Take notice of the distances of the planets from one another, and recognize that almost all are separated from one another in a proportion which matches their bodily magnitudes. Divide the distance from the Sun to Saturn into 100 parts; then Mercury is separated by four such parts from the Sun, Venus by 4+3=7 such parts, the Earth by 4+6=10, Mars by 4+12=16. But notice that from Mars to Jupiter there comes a deviation from this so exact progression. From Mars there follows a space of 4+24=28 such parts, but so*

> *far no planet was sighted there. [...] Let us therefore assume that this space without doubt belongs to the still undiscovered satellites of Mars, let us also add that perhaps Jupiter still has around itself some smaller ones which have not been sighted yet by any telescope. Next to this for us still unexplored space there rises Jupiter's sphere of influence at 4+48=52 parts; and that of Saturn at 4+96=100 parts.*

Later, in 1772, the astronomer Johann Elert Bode, published the second edition of his astronomical compendium titled *Anleitung zur Kenntniss des gestirnten Himmel* (Instructions for the Knowledge of the Starry Sky), where he added a footnote, very similar to Titius's text. In later versions of his book, Bode would credit Titius for this. However, recent research showed that a similar version of this text was included in 1724 book *Vernünftige Gedanken von den Absichten der natürlichen Dinge* (Rational Thoughts on the Intentions of Natural Things) by phillosopher Christian Wolff. The empiric formula which represents this 'law' (which is, in fact, an approximation) and describes the heliocentric distances of the planets in the Solar System is:

$$d = 0.4 + (0.3 \times N) \tag{1.1}$$

where $N = 0, 1, 2, 4, 8, ...$, and d is given in astronomical units (A.U.). The results of this computation fitted quite well all the distances from the Sun to the planets known at that time (see Table 1.1). The interesting fact about this misnamed 'law' is the lack of a planet, predicted to be located between Mars and Jupiter, at 2.8 A.U. from the Sun.

Table 1.1: Heliocentric distances according to Titius-Bode law, compared to the actual distances.

Planet	N	Predicted distance (A.U.)	Actual distance (A.U.)
Mercury	0	0.4	0.39
Venus	1	0.7	0.72
Earth	2	1.0	1.00
Mars	4	1.6	1.52
-	8	2.8	2.77 (Ceres)
Jupiter	16	5.2	5.20
Saturn	32	10.0	9.54
Uranus	64	19.6	19.19
Neptune	128	38.8	30.07

However, it was not until 1781, when the astronomer Sir William Herschel discovered Uranus at the predicted distance, that the scientific community gave validity to the Titius-Bode formula. This fact prompted the starting point for the *missing planet* hunt: several astronomers from the period began to search the sky for the planet, at a predicted distance of ∼2.8 A.U.

At the end of the 18th century, astronomer Baron Franz Xaver von Zach, convinced that there was a missing planet between Mars and Jupiter, realized that an organized search was required. He then invited astronomers from different countries to a meeting in 1798 that is now recognized as the first astronomical conference ever held. This meeting led to the formal creation in 1800 of the *Vereinigten Astronomischen Gesselschaft* ('United Astronomical Society'), popularly known as the *Celestial Police*. Unluckily, they did not succeed in their goal. Before they could even begin their search, in 1801, Giuseppe Piazzi, director of the observatory of Palermo, announced the discovery of a star-like object, which moved relative to the rest of stars in the sky. Piazzi, considering it as a comet, continued to observe this object for several nights, sharing his findings with Bode, who concluded that it was the aforementioned *missing planet*. Later that year, mathematician Johann Carl Friedrich Gauss used these observations to calculate the orbit of this unknown object. Thanks to this, this object was observed again one year after its discovery by astronomer Heinrich Wilhelm Matthias Olbers. The new *planet* was named after Ceres, the Roman goddess of agriculture, grain crops, fertility and motherly relationships.

Olbers continued to observe the new object for several months. During this time, in March 1802, he found another *planet*, which he named Pallas, after the Greek goddess of wisdom, handicraft, and warfare. Herschel's observations proved that the size of the two objects was in fact much smaller than that of the other planets, so he proposed a new naming to the scientific community: asteroids. However, this word was actually coined by the son of a Herschel's friend, Greek scholar Charles Burney Jr., who created the term asteroid in 1802[1], from the greek word $\alpha\sigma\tau\epsilon\rho\omega\iota\delta$, which means "star-like" (Cunningham 2016).

The discovery of asteroids continued along the first decade of the 19th century: in 1804, astronomer Karl Ludwig Harding found a third object, Juno, and in 1807, Olbers found the fourth, Vesta. It was Olbers himself who, at the time, proposed the first theory for the origins of these asteroids, suggesting they were the remaining debris of a planet orbiting the Sun between Mars and Jupiter.

[1] Few days after the discovery of Pallas, according to the correspondence between Herschel and his father.

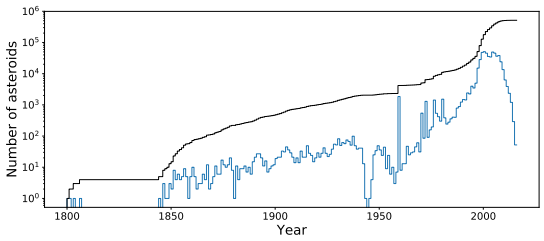

Figure 1.1: Yearly rate (blue) and cumulative number (black) of numbered minor planets discovered in each year, up to 2016. Note that this is not the same as the number of objects given permanent numbers in a given year. Data extracted from `https://www.minorplanetcenter.net/iau/lists/NumberedPerYear.html`.

Prior to 1891, a few more than 300 asteroids were discovered, and, with the arrival of astronomical photography, astronomer Max Wolf discovered, by himself, a total of 228 asteroids, starting with (323) Brucia, in December 1891. The number of minor planets discovered through the first half of the XXth century increased steadily but slowly, and it was not until the second half of the century that this number grew exponentially, as a result of the appearance of CCD cameras and computers, which represented a turning point, due to the creation of surveys and databases exclusively dedicated to this matter.

In the present day, the Minor Planet Center (MPC), founded in 1947, is the official worldwide organization in charge of collecting observational data for minor planets (such as asteroids and comets), calculating their orbits and publishing this information. At the moment this thesis is being written, the Minor Planet Center reports more than 755000 discoveries of minor planets (see Fig. 1.1).

1.2 Small bodies of the Solar System

Asteroids are considered to be one of the most pristine materials present in the Solar System, remnants of the processes that followed the condensation of the proto-planetary nebula and the formation of the planets. Since then, asteroids have undergone little or none geological and thermal transformations. However, these objects have experienced intense collisional evolution that affected their shape, size and superficial composition, among other properties. Some of them contain organic compounds and even water, and knowledge of these traits would contribute to the understanding of how life appeared on Earth. Moreover, there

is a population of asteroids whose orbits cross that of the Earth (which we refer to as near-Earth asteroids, or NEAs), representing a threat to humanity. Also, asteroids might prove to be exploitable sources of components for life support, propellants, or even construction, in the course of human or robotic space exploration, providing a way to replace materials that would otherwise be brought from Earth. Therefore, the study of asteroids will shed light on the evolutionary history of the Solar System, prevent our planet from possible risks in the form of dangerous impacts, and even provide in situ resources for future space exploration missions.

Despite the scientific developments in the last few decades, several questions remain unanswered: *What are the conditions for planet formation and the emergence of life?*, *How did the Solar System evolved, what were its initial stages, conditions, and processes, and the nature of the interstellar matter that was incorporated?*, *What Solar System bodies endanger Earth's biosphere, and what mechanisms shield it?* Asteroid research can be used to investigate the answers to these and other questions.

1.2.1 Asteroids location

Nowadays, the most widely accepted theory for the origin of asteroids in the Solar System states that these objects are planetesimals that never managed to accrete into a single body. This former planet candidate was to be located between the orbits of Mars and Jupiter, where the current asteroid population in the Solar System is mostly concentrated, in what we call the asteroid main belt, a region limited by the gravitational influence of these two planets. This region can be divided in three sub-regions:

- **Inner Main Belt (IMB):** it is limited by the secular resonance ν_6 with Saturn, at around 2.1 A.U., and the 3:1 mean motion resonance with Jupiter, at approximately 2.5 A.U.
- **Mid Main Belt (MMB):** region limited by two mean motion resonances with Jupiter, the 3:1 and the 5:2, this is, between 2.5 and ∼2.82 A.U.
- **Outer Main Belt (OMB):** it is the outermost region of the main belt, also limited by two mean motion resonances with Jupiter, in this case the 5:2 and the 2:1, between ∼2.82 and ∼3.26 A.U.

Besides these three sub-regions, we can point out at least four more groups of asteroids in the region between Mars and Jupiter: Hungarias, located at ∼2.1

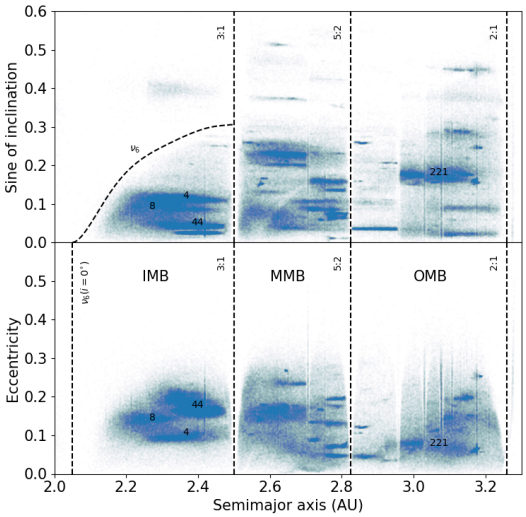

Figure 1.2: Orbital distribution of asteroids in the main belt, according to their proper elements. Data extracted from `http://hamilton.dm.unipi.it/astdys/index.php?pc=5`. The largest asteroid families are marked with the numbers of their parent bodies: (4) Vesta, (8) Flora, (44) Nysa, (221) Eos. The dashed black lines represent the main resonances acting in the main belt.

A.U.; Cybeles, between 3.3 and 3.7 A.U.; Hildas, approximately at 4.0 A.U., in the mean motion resonance 3:2; and Trojans, at the Lagrangian points L4 and L5 of Jupiter's orbit. In addition to the asteroids in the main belt, there exist other regions in the Solar System populated by small objects. NEAs have orbits that are very close to Earth (see Sect. 1.2.2), having perihelion distances of $q < 1.3$ A.U. Mars-Crossers are objects whose orbits approach or intersect the orbit of Mars, and have perihelion distances $1.3 < q < 1.66$ A.U. Other populations of small bodies are the Centaurs, located between the orbits of Jupiter and Neptune, presenting intermediate characteristics between asteroids and comets, and the trans-Neptunian objects (TNOs), beyond the orbit of Neptune and up to 50 A.U., composed largely of ices (water, methane,

or nitrogen) mixed with silicates (de León et al. 2017).

In Fig. 1.2 we can see the distribution of asteroids in the main belt, according to their proper orbital elements. These orbital parameters are constants of motion of an object in space that remain practically unchanged over an astronomically long timescale. Their main use is the study of asteroid families, which, in Fig. 1.2, are the regions with high density of points (see Sect. 1.2.3). It is easy to recognize the limits of each part of the main belt. These bordering areas, which separate the IMB, MMB, and OMB, are caused by the mean motion resonances[2] with Jupiter, and by the secular resonance[3] ν_6 with Saturn, as stated before. They are known as Kirkwood gaps (Kirkwood 1867). In particular, as we will see in the corresponding section, the IMB plays a fundamental role in the replenishment of the NEA population, due to the prominent resonances bounding this region.

1.2.2 Near-Earth objects

Near-Earth objects (NEOs) are, as the name indicates, small bodies in the Solar System whose orbits are "near" to that of the Earth. By definition, near-Earth objects are asteroids (or comets) with perihelion distance $q \leq 1.3$ A.U. Most of the NEOs are asteroids (NEAs). These are divided into several groups according to their perihelion and aphelion distances, and their semimajor axis, a (see Table 1.2).

Although all these objects are in near-Earth orbits, only Atens and Apollos cross Earth's path, and the probabilities of impact in the near future are very low. However, if a large enough asteroid was to hit the Earth, the impact would pose a threat for life in our planet. Because of this, understanding their compositional characteristics is primordial in order to establish the possible consequences of a hypothetical impact. Also, the analysis of the surface minerals will provide information about the heating mechanisms and aqueous alteration processes that these objects have undergone through the Solar System history. In addition, the compositional studies, combined with dynamical models, might help to trace these objects back to their sources, and will shed light on the transport mechanisms that operate in the Solar System.

[2]Mean motion resonances occur when two orbiting bodies apply a regular, periodic, gravitational influence on each other, because their orbital periods are related by a ratio of small integers (3:1, 5:2, or 2:1).

[3]Secular resonances occur when the precession velocity of two orbits is synchronized (a precession of the perihelion, for example). A small body in secular resonance with a much larger one will precess at the same rate as the large body. Over relatively short time periods (of the order of 10^6 yr) a secular resonance will change the eccentricity and inclination of the small body.

Table 1.2: Different NEAs populations, according to their orbital parameters.

Population	a (AU)	q (AU)	Q (AU)
Atiras	<1.0	-	<0.983
Atens	<1.0	-	≥0.983
Apollos	>1.0	<1.017	1.00
Amors	>1.0	1.017–1.3	1.52

The sources of NEAs have been the subject of speculation for many years. In the 1970s, it was conjectured that many NEAs were extinct cometary nuclei, because limited knowledge existed on how objects migrate from the main belt to the near-Earth space (Wetherill 1976). The first indication that resonances can force main belt asteroids to cross the orbits of the planets came from J. G. Williams (see Wetherill 1979) and Wisdom (1983). Following these works, several studies confirmed, both analytically and numerically, two efficient transport routes for the origin of NEAs: the ν_6 secular resonance with Saturn, and the 3:1 mean motion resonance with Jupiter. Using these advances, Wetherill, in the 1980s, hypothesized that NEAs were resupplied via a two-step process: first, catastrophic collisions and/or cratering events in the main belt injected debris into main belt resonances, and then, resonant motion would move the fragments into the near-Earth space.

Another important mechanism that comes into play in this process, and that takes place in the delivery of objects into the NEA population, is the Yarkovsky effect (Bottke et al. 2002b). This effect, first proposed by Ivan Osipovich Yarkovsky (1844–1902) around 1900, and discussed decades later by Opik (1951), is produced by a thermal radiation force that causes objects to undergo semimajor axis drift and spinup/spindown as a function of their spin, orbit, and material properties. This mechanism can disperse asteroid families, causing their members (with diameters $D < 20$ km) to drift away from their parent bodies, until they get trapped in mean motion and secular resonances within the main belt, regions that, as mentioned before, are efficient transport routes for asteroids into the near-Earth space.

Thus, asteroid families, which are originated after catastrophic collisions within the main belt, whose leftovers drift away into chaotic resonances due to the Yarkovsky effect, are preferred over single objects as near-Earth asteroids sources.

1.2.3 Asteroid families

At the beginning of the XXth century, the Japanese researcher Kiyotsugu Hirayama was the first to use the concept of proper orbital elements to identify groups of asteroids sharing very similar orbital properties (Hirayama 1918, 1923, 1928). These groupings, known today as asteroid families, are thought to be the direct result of energetic collisional events. Along the last century, the efforts in characterizing asteroid families have been numerous, and different identification methods were devised. However, it was in the early 1990s when, due to the availability of large datasets of asteroid proper elements (Milani & Knezevic 1990, 1992) and the simultaneous development of better techniques for asteroid family identification (Zappala et al. 1990; Zappala & Cellino 1994), promising new perspectives on the study of these groupings were opened.

Developments in spectroscopic techniques allowed to find, through observations performed by Binzel & Xu (1993), the first confirmation of the collisional origin of a family: the Vesta family. The spectroscopic study of these collisional groupings have steadily increased since then, focused on characterizing the overall mineralogical composition of different families, and at the same time looking for possible evidence of thermal differentiation of the original parent bodies.

If asteroid families are really fragments of disrupted parent bodies (which seems a quite accurate theory given the evidence obtained up to now) then the family members will give us information about the interiors of the original asteroids. Thus, the spectroscopic study of asteroid families provides a unique opportunity to obtain information about the inner layers of the family parent body. That is, by looking at asteroid families, we are looking at '*dissected*' asteroids.

Families are usually named after the largest asteroid inside the defined collisional group. The most prominent families, according to their number of members (>9000), are Nysa, Vesta, Flora, and Eos (see Fig. 1.2). Asteroid families appear as clusters of points in the proper orbital elements space. Considering the asteroids distribution shown in Fig. 1.2, the presence of a significant number of families through the whole main belt seems obvious. Statistical investigations show that almost half of the asteroids occur in families.

The standard method to identify asteroid families consists of the computation of proper elements, or other elements unchanging with time, for asteroids with well-known orbits; identification of clusters or groups of asteroids in proper elements space; and finally, establishing the statistical significance of the identified groups (see Nesvorný et al. 2015 and references therein). There are a total of 122 asteroid families identified in Nesvorný et al. (2015), although other

authors propose different numbers.

1.3 Asteroid physical characterization

There exist several remote observational techniques that are used to physically and dynamically characterize asteroids: light-curve measurements to obtain rotation periods, astrometry to obtain accurate orbits and positions, spectral measurements to infer superficial composition, etc. The most used technics are photometry and spectroscopy.

A lot of information about asteroids can be inferred by simply measuring the light that comes from them. This technique, known as photometry, consists of accounting for their brightness in a visual or photographic way, or as it is mostly done nowadays, through the use of CCD cameras. If some color-filter is applied, the light is limited inside some specific wavelengths, and through the use of several filters, one can obtain a very low resolution spectrum. This technique would be known as spectrophotometry. Through the addition of slits, prisms, and more recently, grisms (which are combinations of prisms and gratings), it is possible to obtain spectra of asteroids at selected wavelengths.

The first spectrophotometric data of asteroids dates back to 1929. Bobrovnikoff used photographic techniques to observe the region between 0.4–0.5 μm of several asteroids, finding diverse spectral properties among the observed sample (Bobrovnikoff 1929). However, it was not until the year 1950 that the observations of asteroids in different photometric filters (UBV) would plant the seeds of the asteroid taxonomies.

In 1970, the first reflectance spectrum of an asteroid, (4) Vesta, was published by McCord et al. (1970), using spectrophotometry of 24 narrow-band filters in the spectral range 0.3–1.1 μm. Zellner (1973) was the first to notice some bimodality on the polarimetric albedos of asteroids, recognizing two groups: some dark carbonaceous objects, and some bright rocky ones. Then, in 1975, Chapman et al. (1975) performed a comprehensive analysis of the spectrophotometric data in 24 filters, polarimetry, and radiometry available at that moment, compiling data for a sample of 110 asteroids, and proposing the first nomenclature based on letters: C for carbonaceous objects, S for stony, and U for unknown (objects that did not match either of the other two categories).

On the year 1980 the Eight Color Asteroid Survey (ECAS) was completed (Zellner et al. 1985). A total of 589 minor planets were observed using eight photometric filters with passbands ranging from 0.34 to 1.04 μm. This gave birth to the first widely used taxonomic system: the Tholen taxonomy.

1.3.1 Asteroid taxonomies

The goal of asteroid taxonomy (term formed from the Greek words $\tau\alpha\xi\iota\sigma$, taxis, which means arrangement, and $\nu o\mu\iota\alpha$, nomia, which means method) is to identify groups of asteroids that share similar surface compositions. This "arrangement method" is the first step for further studies of comparative planetology. The classification is performed by statistically processing the spectrophotometric, spectral, or polarimetric data of a significant number of objects. In the case of asteroids, a precise taxonomic system gives an approach to a specific mineralogy for each of the defined classes.

One of the techniques used to characterize the surface of asteroids is reflectance spectroscopy in the visible and near-infrared wavelength regions. Diagnostic features in spectra related to electronic and vibrational transitions within minerals or molecules are detectable in the 0.35–2.50 μm spectral range. The overlapping of the absorption bands from different mineral species provides a distinctive signature of the asteroid surface. Olivine, pyroxene (clino- and ortho-pyroxene), iron-nickel (Fe-Ni) metal, spinel, and feldspar are some of the most important minerals that can be identified by carefully analyzing asteroids' reflectance spectra (McSween 1999).

Historically, the most widely used taxonomies are the following: Tholen (1984), which used data from the Eight Color Asteroid Survey (Zellner et al. 1985); Bus & Binzel (2002), which used data from the Small Main-Belt Asteroid Spectroscopic Survey–SMASS (Xu et al. 1995); and DeMeo et al. (2009), which is an extension of the previous taxonomy scheme into the near-infrared. These three taxonomies are based on the color or spectral slope of the asteroid, the presence or not of a 1 μm absorption feature associated to silicates (pyroxene and olivine) and the presence of an absorption band in the ultraviolet region, that produces a decrease of reflectance below 0.5 μm. Here we give a brief description of each of these three taxonomies:

- **Tholen:** This classification, proposed by David J. Tholen in his PhD thesis, in 1984, was inferred from narrow-band filter spectrophotometry in the wavelength range 0.3–1.0 μm. This taxonomy presents 14 classes, each designated by a single letter. In addition to the S and C classes (already defined in previous works), Tholen identified another 6 groups: A, B, D, F, G, and T. Using albedo information, another three classes, with featureless spectra, where identified: E, M, and P. The last three classes were each defined according to just one spectrum: (4) Vesta, V; (1862) Apollo, Q; (349) Dembowska, R. This was the most widely used taxonomy for over a decade.

- **Bus:** This is a more recent taxonomy introduced by Schelte J. Bus and Richard P. Binzel in 2002 (Bus & Binzel 2002), based on the Small Main-Belt Asteroid Spectroscopic Survey (Xu et al. 1995). This survey produced spectra of a far higher resolution than ECAS, and was able to resolve a variety of narrow spectral features. However, a somewhat smaller range of wavelengths (0.44 μm to 0.92 μm) was observed. Also, albedos were not considered. Attempting to keep to the Tholen taxonomy as much as possible given the differing data, asteroids were sorted into the 26 types shown in Table 1.3. The majority of bodies fall again into the broad C and S complexes, with a few unusual bodies categorized into several smaller types.

- **Bus–DeMeo:** This is an extension of the taxonomy defined by Bus and Binzel into the near-infrared, up to 2.45 μm (DeMeo et al. 2009). The authors used a total of 371 asteriod spectra to create this taxonomy. Almost all of the spectral classes overlap with those from the Bus & Binzel (2002) taxonomy, except for the S_v type, which is new, at the expense of the S_k and S_l classes, which were removed, and the L_d type, which was integrated into the L and D classes.

In Table 1.3 we present a summary of these taxonomies, with the proposed spectral classes and their characteristics.

There exist other taxonomic classifications, for example those from DeMeo & Carry (2013) and Carvano et al. (2010), that exploit very large datasets, such as the Sloan Digital Sky Survey (York et al. 2000). Although not as precise as the spectroscopy-based taxonomies, due to the use of only five broad-band filters, these taxonomies might provide very good approximative classifications for tens of thousands of asteroids, making up for the lack of mineralogical information by improving the statistics in a significant manner.

Asteroids present different compositions depending on their distance to the Sun at the time of formation, with objects formed closer to the Sun having rocky, anhydrous silicate-rich mineralogies while those formed further from the Sun preserving their carbon compounds and hydrated minerals (lower temperatures). This explains the distribution of taxonomies in the main belt, with the majority of S-complex asteroids concentrating in the IMB while the primitive, C-complex asteroids being mostly found in the MMB and OMB. However, current theories to explain the dynamical evolution of our solar system include planetary migration episodes that might have mixed-up asteroids in the main belt and incorporate primitive, C-complex asteroids to the IMB in a later stage. This will explain the presence of primitive asteroids in that region.

Table 1.3: Table comparing the main taxonomies and their respective proposed mineralogical compositions. From De Prá (2017), adapted from DeMeo et al. (2015).

Complex	Tholen 0.35-1.0 μm	Bus 0.4-0.9 μm	Bus-DeMeo 0.45-2.5 μm	Proposed mineralogy
C	F, B, C, G	B, C, C_b, C_g, C_{gh}, C_h	B, C, C_b, C_g, C_{gh}, C_h	Opaque materials, carbon, phyllosilicates. Some weak absorption bands point to the presence of olivine and pyroxene.
S	S	S, S_a, S_q, S_r, S_k, S_l	S, S_a, S_q, S_r, S_v	Olivine and pyroxene.
X	E, M, P	X, X_c, X_e, X_k	X, X_c, X_e, X_k	E: Related to enstatite meteorites. P: Opaque material, carbon. M: Metallic meteorites?
Individual classes	T, D, O, R, V, A	T, D, Q, O, R, V, A, K, L, L_d	T, D, Q, O, R, V, A, K, L	T: ? D: Opaque materials, organics. Q: LL ordinary chondrites. O: Pyroxene, olivine. R: Olivine, pyroxene. V: HEDs meteorites. A: Pallasite, brachinite, R chondrites, olivine. K: CO and CV carbonaceous chondrites, olivine. L: CAIs, spinel-rich.

Through the main text of this work we use the words "rocky" and "primitive" to refer to two different types of asteroids, inferred from the aforementioned taxonomies. Rocky asteroids are objects with typically high albedos ($p_V > 0.2$), composed mainly of silicate minerals. Their spectra show moderately steep slopes below 0.7μm, and present weak to very strong absorption features around 1 and 2 μm, indicative of the presence of olivine and pyroxene. All the S-types and subclasses (S-complex), as well as high-albedo X-types (M-types in the Tholen taxonomy), A, K, L, Q, V, and R-types, are included in the group of rocky asteroids. Primitive asteroids, on the other hand, are completely distinct objects, with featureless spectra, composed mainly of carbonaceous material. In the following section we give an in-depth description of primitive objects, on which the present thesis work is focused.

1.4 Primitive asteroids

We denominate "primitive asteroids" to those objects with typically low albedos ($p_V < 0.15$), which are believed to be composed of the most primitive materials. These objects contain pristine substances that have undergone very little processing since the Solar System formation 4.5 billion years ago. Therefore, the study of primitive asteroids can reveal information about the origin and evolution of our planetary system since its early stages.

Primitive asteroids are found in the dark taxonomic classes, that include the C-types and all the subclasses, the B-type asteroids, with a characteristic negative slope in the visible, low-albedo X-types, T- and D-type asteroids. These objects present featureless spectra in the visible wavelengths, with slopes ranging from blue to red (negative to positive), except for the presence of broad and shallow absorption bands associated to hydrated silicates. In addition, various studies on asteroids classified as B-types in the visible spectral range have demonstrated that these objects can show considerable diversity in their near-infrared spectra (Clark et al. 2010; de León et al. 2012).

Primitive asteroids are commonly associated with carbonaceous chondrites (a class of chondritic[4] meteorites), on the basis of similarities in overall spectral shapes (one of the usual techniques to infer the mineralogical compositions of asteroids is the comparison with meteorite spectra). Carbonaceous chondrites are the most primitive materials in the Solar System. They were formed in oxygen-rich regions of the early Solar System, and are composed of carbon-rich

[4]Chondrites are non-metallic meteorites that have not been modified due to melting or differentiation of the original body. They were formed when various types of dust and small grains that were present in the early Solar System accreted to form asteroids.

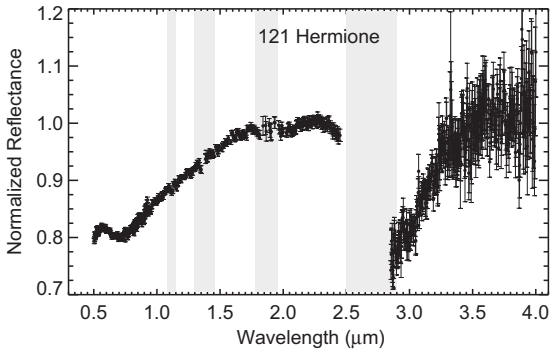

Figure 1.3: Visible to near-infrared spectrum of primitive asteroid (121) Hermione, adapted from Takir & Emery (2012). Here we can appreciate both typical absorption bands, one centered at 0.7 μm, and another centered around 3 μm, indicative of water bearing silicates.

materials condensed under low temperature and pressure conditions. Carbonaceous chondrites include a diversity of subgroups that exhibit different degrees of aqueous and/or thermal alteration, but are generally characterized by an overall dark appearance (Cloutis et al. 2011). In the same way, spectra of primitive asteroids show signatures of more or less aqueous alteration. Recently, two studies discovered water-ice and organic molecules on two outer-belt primitive asteroids, (24) Themis and (65) Cybele (Campins et al. 2010b; Licandro et al. 2011). Although water-ice is not expected on inner-belt asteroids (mainly due to their proximity to the Sun, which might have caused its sublimation), spectral features due to organics and hydrated silicates are indeed observed. Using ECAS data, Vilas & Gaffey (1989) identified for the first time a shallow absorption band centered around 0.7 μm, associated to phyllosilicates (see Fig. 1.3). This type of minerals are formed through a slow chemical alteration caused by the presence of liquid water. This means that, in the case that an asteroid spectrum presents this absorption band, water was present on the asteroid's surface at some point during its lifetime.

Another spectral feature which is an unambiguous indicator of the presence of water or aqueously altered minerals on the surface of asteroids is an absorption band around 3 μm (see Fig. 1.3). However, this spectral feature might be difficult to observe using ground-based telescopes, due to the atmospheric ab-

sorption bands, which operate in that wavelength region. Therefore, according to Rivkin et al. (2015), the 0.7 μm absorption feature can be used as a proxy for hydration. Takir & Emery (2012) showed that the presence of the 0.7 μm band was 100% correlated with the presence of the 3 μm band, but this does not work on the opposite way. Thus, the 0.7 μm band gives an estimate of the inferior limit of hydration in the main belt.

Mapping the frequency of phyllosilicates on asteroids' surfaces is a way to constrain the past and present water volume in the main belt. Since carbonaceous asteroids are an important source of volatiles and organic matter, a complete understanding of these materials might provide answers to the role of primitive bodies as building blocks for planets and life.

1.4.1 Space missions to primitive NEAs

Their proximity to Earth's orbit makes some NEAs accessible to spacecrafts. Primitive asteroids have already been visited over the course of space missions: the NEAR Shoemaker probe (Cheng 2002) performed a flyby to the C-type asteroid (253) Mathilde in 1997, returning imaging and gravitational data allowing calculations of Mathilde's dimensions and mass, and the Dawn spacecraft (Russell et al. 2015) arrived to (1) Ceres in 2015, mapping the surface of the asteroid while orbiting the object. This mission is still ongoing, and it will be possibly extended until the second half of 2018.

In order to bring surface material from primitive asteroids back to Earth, two sample-return missions to primitive NEAs have been devised: Japanese Aerospace Exploration Agency Hayabusa 2, and NASA Origins, Spectral Interpretation, Resource Identification, Security-Regolith Explorer (OSIRIS-REx). The Hayabusa 2 mission, launched succesfully on December 3, 2014, will arrive at primitive C-type NEA (162173) Ryugu in 2018 (Tsuda et al. 2013). It will orbit the object for approximately one year before returning a sample from its surface in 2020[5]. The NASA mission, OSIRIS-REx, was launched on September 8, 2016 (see Fig. 1.4), and will also arrive in 2018 at another primitive asteroid, B-type (101955) Bennu (Lauretta et al. 2010, 2017). It will also orbit the target around one year, before collecting a surface sample that will be returned to Earth for analysis in 2023. The Hayabusa 2 and OSIRIS-REx missions will provide a huge wealth of information that will help to understand both the role that primitive asteroids may have played in the origin of life on

[5]This is not the first sample-return mission developed by the Japanese Aerospace Exploration Agency. In 2003, the Hayabusa spacecraft was launched, arriving at S-type asteroid (25143) Itokawa in 2005, collecting a sample of material from its surface, and bringing it back to Earth for analysis in 2010.

Figure 1.4: OSIRIS-REx launch (September 8, 2016) from Cape Canaveral Air Force Station, Florida. Image extracted from Lauretta et al. (2017).

Earth and how they served as one of the fundamental "building blocks" of planet formation.

The science outcome of the missions will also improve our ability to compute the long-term ephemeris of objects like Bennu or Ryugu, whose orbits cross the path of the Earth, and also help to predict their future trajectories, determining whether an impact is possible within the next several hundreds of years. In addition, NEAs might provide resources, such as water and organic molecules, that can support future attempts of Solar System exploration. The missions will investigate the resource potential of the targets and extrapolate this knowledge to other accessible NEAs.

1.5 PRIMASS

The work presented in this thesis is part of our PRIMitive Asteroids Spectroscopic Survey (PRIMASS). This survey started in 2010, to characterize the proposed origin of asteroids (101955) Bennu and (162173) Ryugu in the Polana family. Once this initial objective was fulfilled, this survey continued to collect spectra of primitive asteroids all through the main belt. The aim of this survey is to provide the community with a comprehensive collection of data that enable us to study the surface composition of primitive asteroids by means of

visible and near-infrared spectroscopy.

Near-Earth asteroids (101955) Bennu and (162173) Ryugu have been linked to five distinct possible sources: a group of four low-albedo collisional families in the inner main belt (Polana–Eulalia, Erigone, Sulamitis, and Clarissa), and a population of low-albedo and low-inclination background asteroids in the same region (Campins et al. 2010a, 2013).

Based on this association, (101955) Bennu and (162173) Ryugu were probably part of two larger carbonaceous parent asteroids (diameter>100 km) in the inner main belt, that were catastrophically disrupted 0.7–2 Gyr ago. The fragments that became both NEAs were eventually delivered to the near-Earth space via a combination of Yarkovsky-induced drift and interaction with giant-planet gravitational resonances (Bottke et al. 2015). The study and characterization of the originating populations of both NEAs will significantly enhance the scientific outcome of the missions: we will be able to trace these NEAs back to their parent families, confirming the dynamical and evolutionary theories about their origins.

PRIMASS is already the largest spectral database of primitive asteroids, with more than 530 spectra (>90% of the asteroids had no spectroscopic data before) in the inner and outer belt. Several publications are part of this survey: de León et al. (2016); Pinilla-Alonso et al. (2016); De Prá et al. (2017), and, as a part of this thesis, Morate et al. (2016) and Morate et al. (2018a). The survey is on-going and, considering the current awarded time, the number of proposals submitted to different Time Allocation Committees, and our rate of success, we estimate that PRIMASS will contain more than 700 spectra of primitive asteroids by the end of 2019.

We note that the first family dataset that we used as reference for PRIMASS was Nesvorny (2012), where the only low-albedo groups identified in the inner region of the main belt were the Polana, Erigone, Sulamitis, and Clarissa families, which are the ones investigated in this thesis work. However, in Nesvorný et al. (2015), four new small low-albedo families were identified in the inner belt, located at inclination $i > 8°$: Klio, Chaldaea, Svea, and Chimaera. Although these families are not object of study of the present work, they will be addressed in the near future, as we point out in Chapter 7.

1.5.1 The Polana–Eulalia complex

In the context of PRIMASS, the first step was the spectral analysis of the Polana family, identified as one of the likely origins of asteroids (101955) Bennu (Campins et al. 2010a) and (162173) Ryugu (Campins et al. 2013).

While gathering spectral data for this family, a new dynamical study was

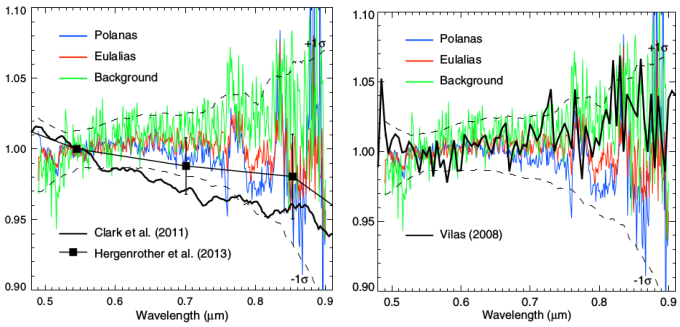

Figure 1.5: Mean spectra of asteroids in the Polana–Eulalia complex compared to the visible spectrum (Clark et al. 2011) and the ECAS photometry (Hergenrother et al. 2013) of Bennu (left panel), and the visible spectrum of Ryugu in the right panel (Vilas 2008). Adapted from de León et al. (2016).

published by Walsh et al. (2013). These authors concluded that the so-called Polana family was indeed two families occupying the same region in the orbital parameters space: the "new Polana" family, with asteroid (142) Polana as parent body, and the Eulalia family, with asteroid (495) Eulalia as parent body. Walsh et al. (2013) also suggested that membership to each of these families could be determined by means of visible and near-infrared spectroscopy. The region occupied by the "new Polana" and Eulalia families (Polana–Eulalia complex, hereafter), was analyzed by means of visible (de León et al. 2016) and near-infrared (Pinilla-Alonso et al. 2016) spectroscopy.

In de León et al. (2016), a total of 65 asteroids were observed in the visible spectral range in a coordinated observational campaign with the 10.4 m Gran Telescopio Canarias (GTC), the 3.6 m New Technology Telescope (NTT), and the 3.6 m Telescopio Nazionale Galileo (TNG). The sample comprised 37 asteroids from the Eulalia group, 20 from the Polana group, and 8 background objects. The spectral analysis of the sample showed that, in spite of the presence of distinct dynamical groups, the asteroids in that region presented spectral homogeneity at visible wavelengths, showing a continuum of spectral slopes, from blue to moderately red, typical of primitive asteroids classified as B- and C-types. Thus, it is not possible to distinguish between members of the Polana and the Eulalia families using visible spectroscopy alone. In addition, the spectral data available for asteroids (101955) Bennu and (162173) Ryugu

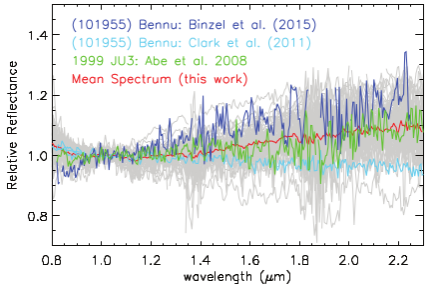

Figure 1.6: Comparison of (101955) Bennu and (162173) Ryugu with the spectra of the Polana–Eulalia complex (grey). The mean spectrum of the sample is depicted in red. The dark blue spectrum of Bennu is from Binzel et al. (2015), and the cyan spectrum is from Clark et al. (2011). The Ryugu spectrum, in green, is from Abe et al. (2008). Figure extracted from Pinilla-Alonso et al. (2016).

were compatible with the spectra of the asteroids in this region (see Fig. 1.5).

In Pinilla-Alonso et al. (2016) they observed 63 asteroids in the near-infrared spectral range, obtained with the 3.0 m NASA Infrared Telescope Facility (IRTF) and the TNG. The study of near-infrared spectra of asteroids in this region showed similar results to those obtained from visible spectra: the sample of observed asteroids presented spectral homogeneity, with a continuum of neutral to moderately-red concave-up spectra, and this homogeneity was independent of membership to the families (Eulalias or Polanas were not distinguishable). Also, the near-infrared spectra of (101955) Bennu and (162173) Ryugu are very similar to the average near-infrared spectrum of the sample, which would be compatible with an origin in this region of the inner belt (see Fig. 1.6).

The following step was to observe and study the rest of the inner belt primitive families. This thesis is the continuation of that work: a compendium of three articles, published in Astronomy & Astrophysics[6], that are the fruits of this research. In Chapter 2 we summarize the main goals of this thesis. In Chapter 3 we give a description of the observational techniques and the methods of analysis used in this thesis. Chapter 4 includes the published results obtained from the analysis of the Erigone collisional family, in Chapter 5 we show the results obtained from the analysis of the Sulamitis and Clarissa families, and in Chapter 6 we present the characterization of a significant number

[6] https://www.aanda.org

of collisional families through the whole main asteroid belt by means of near-infrared photometry. In Chapter 7 we present the conclusions of this thesis work and future perspectives.

Chapter 2

Objectives

As stated in Sect. 1.5, this thesis has been conducted within the context of the PRIMASS survey. As such, the main goal of the work presented here is to contribute to improve the understanding of primitive asteroids in general, and collisional families of primitive asteroids in particular, as well as their presence and distribution in the main asteroid belt. The objectives of this thesis can then be summarized in the following points:

- To perform a spectral characterization of the Erigone, Sulamitis, and Clarissa collisional families located in the inner main belt, as a continuation of the work started with the Polana–Eulalia complex. This will provide a general context to, and will enhance, the science return of both OSIRIS-REx and Hayabusa 2 missions. Results obtained from this spectral characterization will also serve as tests and will put constraints to the dynamical models that explain the origins and evolution of asteroids (101955) Bennu and (162173) Ryugu (Bottke et al. 2015).
- To search for other potential sources of primitive asteroids in the main belt. This implies the characterization by means of spectroscopic and/or photometric data of families in the central and outer regions of the main asteroid belt, in addition to those in the inner main belt.

Chapter 3

Methodology

The work presented in this thesis has been carried out using different methods of analysis, databases, and statistical approaches. Although some of them were briefly introduced in the previous chapter, we make here a detailed description of the most important procedures that we used in the papers that comprise the thesis: the spectroscopic observations, the tool used for taxonomical analysis, the obtention, current status, and usage of the MOVIS catalog, and the hydration band detection pipeline.

3.1 Spectroscopic observations

All the asteroid spectra present in this thesis work[1] have been obtained using the OSIRIS instrument[2], at the 10.4 m Gran Telescopio Canarias (GTC). This telescope, located at the El Roque de los Muchachos Observatory (ORM), in the island of La Palma (Spain) is the largest optical telescope in the world. A total of 198 spectra of asteroids were obtained with the GTC.

The observations were part of a "filler" program that spanned the semesters 2014B, 2015A, 2015B, and 2016A. The aim of this type of program (done in service mode) is to obtain data with a good signal to noise ratio for targets that are relatively bright for a 10 m-class telescope in non-optimal conditions, like seeing larger than 1.5", bright nights, or partial cirrus coverage. In our case, we typically selected for our observations asteroids with magnitudes $18 < m_V < 21$,

[1] Except for one of the two spectra of (752) Sulamitis, and the two spectra from the SMASS database.

[2] The specifications of the instrument are described in Chapter 4.

bright asteroids for the GTC. Exposure times varied depending on the target brightness: the total exposure times were in the range 900–1800s, usually divided in three exposures. However, since the sky conditions might vary from one night to another, the spectra quality might be different. The observing conditions for every asteroid are shown in the corresponding tables in Chapters 4 and 5.

The observational procedure was the following:

- First, we needed to identify our target. For this, the telescope was pointed to the object field according to its ephemeris, obtained from the Minor Planet Center[3] or the Horizons [4] webpages. Then, an image was acquired. After this, the telescope pointed to a solar analog star to obtain its spectrum, that was used for calibration purposes, as we will see later. We then returned to the asteroid field and another image was taken. By comparing both images of the same field, we identified the asteroid moving with respect to the stars[5].
- Then, the asteroid movement was tracked using its predicted velocities in right ascension and declination, and the asteroid was centered in the slit position. The slit was oriented to the parallactic angle, to minimize loses due to atmospheric differential refraction. This effect is due to the fact that the light from objects outside the atmosphere, when travelling through the different atmospheric layers, is deflected, producing an apparent displacement in the images. This effect is different depending on the wavelength, and the direction of the dispersion is perpendicular to the observational horizon. In all the cases, we used either a 5"- or a 2.5"-width slit.
- Once the slit was inserted, another image of the asteroid was taken, to check if it was in the right position. To increase the signal to noise ratio of the final spectrum, to improve the sky subtraction, and to minimize fringing effects[6], a series of three spectra were taken, offsetting the telescope 10" in the slit direction.

[3] `https://www.minorplanetcenter.net/iau/MPEph/MPEph.html`

[4] `https://ssd.jpl.nasa.gov/horizons.cgi`

[5] There are some online tools, such as Astfinder (`http://asteroid.lowell.edu/cgi-bin/astfinder`), that might help to identify the target, showing the predicted field.

[6] This effect is produced in the CCD detectors due to the interferences generated between the incident light and the internal reflections. The amplitude of the fringe interferences depend, among other things, on the quantum efficiency of the detector, and it is larger for redder wavelengths in CCD detectors in the visible range.

To calibrate the obtained asteroid spectra, in addition to the usual bias and flat-field images (and in exchange of the usual flux-standard stars, commonly used in other astronomy fields), we need to obtain spectra of solar analogs, i.e., stars with spectra very similar to that of the Sun. Since asteroids reflect the light of the Sun on their surfaces, rather than emitting light themselves (at least in non-thermal wavelengths, i.e., below 5μm), the solar contribution needs to be removed from the asteroid spectra. This is done through the observation of at least one solar analog star (preferably more than one) during the night. These stars are observed at airmasses similar to those of the objects. The different solar analogs that we used in this thesis work are shown in the corresponding tables in Chapters 4 and 5.

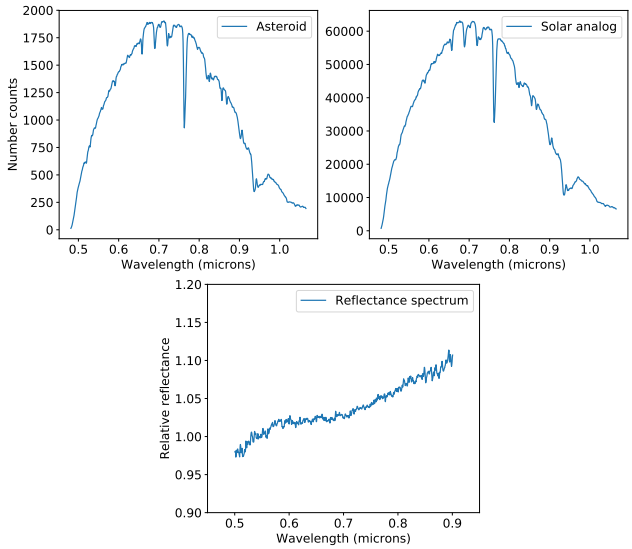

Figure 3.1: Graphical representation of the obtention of the asteroid's reflectance spectrum. The asteroid spectrum (before removing the Sun contribution) is plotted in the upper left panel. The solar analog spectrum is depicted in the upper right panel (note that both spectra are very similar). The final reflectance spectrum after the division is shown in the bottom panel.

In order to remove the solar contribution from the asteroid data, we simply divide the asteroid spectrum by that of the solar analog, and then normalize the

resulting spectrum at 0.55 μm[7], obtaining what we know as "reflectance spectrum". In Figure 3.1 we show an example of this procedure. This reflectance spectrum is then analyzed, looking for characteristic features that will help to determine the asteroid's surface composition, and classify it according to the different taxonomies at hand (see Sections 1.3.1 and 3.2).

3.2 Taxonomical classification

In Chapters 4 and 5, after obtaining the asteroid spectra, we performed a taxonomical classification, in order to infer the possible surface composition of the objects. This classification has been carried out using an online tool, M4AST (Modeling for Asteroids), dedicated to asteroid spectra and developed by Popescu et al. (2012).

M4AST consists of a database containing data from different observational programs and a set of tools for spectral analysis and interpretation. M4AST covers several aspects related to the statistics of asteroids: taxonomy, curve matching with laboratory spectra of meteorites, etc. This tool was conceived to be available via a web interface and is offered for the scientific community[8].

In order to perform the taxonomical analysis, we first uploaded into the database the spectrum that we wanted to analyze. This spectrum must have at least two columns, indicating the reflectance at the corresponding wavelengths. It might also include the measurement errors as a third column. The spectrum is uploaded as a temporary file into the tool's database, and it is given a temporary name, which will be used for the analysis.

After uploading the spectrum, it is possible to perform different actions on it: plotting the data, concatenating it with another spectrum, comparing it with meteorite spectra, and the one in which we are interested, that is, classifying the spectrum according to a taxonomical schema. For this, it is possible to choose between three different options: Bus–DeMeo (DeMeo et al. 2009), and two less used taxonomies, G13, and G9 (Fulchignoni et al. 2000). The taxonomic classes are defined in different wavelength intervals: 0.45–2.45 μm for Bus–DeMeo taxonomy, 0.337–2.359 μm for G13 taxonomy, and 0.337–1.041 for G9 taxonomy.

The classification according to the Bus–DeMeo taxonomy (the one that we used for our analysis) is determined by comparing the asteroid spectrum with the templates of each taxonomic class. For this, a χ^2 curve matching approach is used. An example of the output of the procedure is shown in Fig. 3.2,

[7] Central wavelength of the Johnson V filter, adopted reference for normalization.
[8] `http://m4ast.imcce.fr`

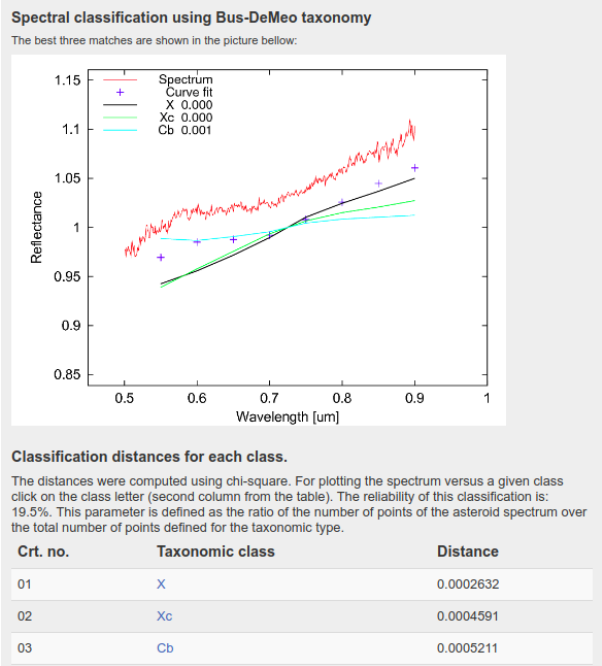

Figure 3.2: Screenshot of the typical output of the taxonomical analysis tool that we used to classify the spectra of this thesis. The spectrum, as well as the fit, and the three best-fitting templates, are shown in the figure. Below this figure, the taxonomical classes of these templates, as well as the residuals of the fitting process, are also shown. The offset between the uploaded spectrum and the templates (and the spectrum fit) is due to the fact that the latter are normalized according to the mean value of the spectrum.

where the most similar taxonomical classes and their corresponding errors are provided.

Our spectra have data only in the visible wavelength range (i.e., between 0.5–0.9 μm). The Bus–DeMeo taxonomy extends into the near-infrared, but the classes present in this taxonomy overlap with those from the Bus taxonomy (Bus & Binzel 2002), defined in the same wavelength range as our spectra (0.44–0.92 μm). Thus, we have considered the M4AST output for the Bus–DeMeo taxonomy equivalent to the Bus taxonomy, classifying the spectra according to

this last one. In Fig. 3.3 we show the template spectra of this taxonomy.

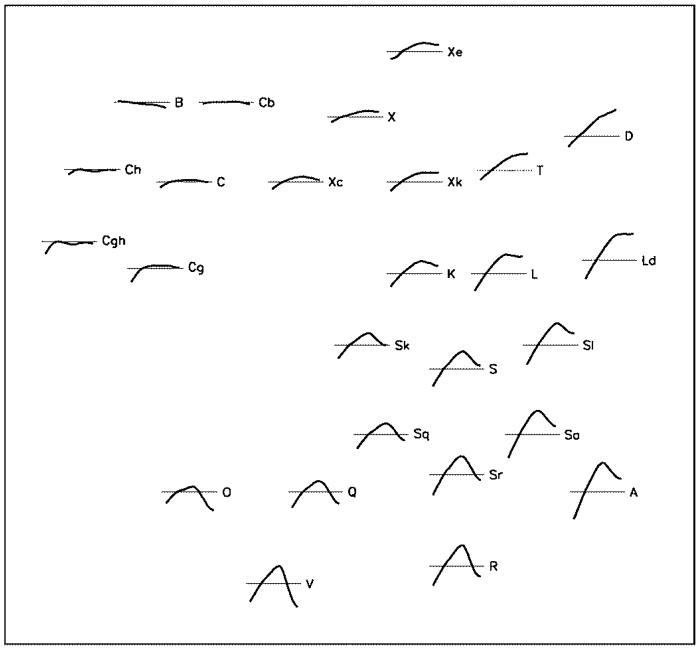

Figure 3.3: All 26 taxonomic classes in the Bus taxonomy. The horizontal lines to which each spectrum is referenced represents a normalized reflectance of 1.00. Extracted from Bus & Binzel (2002).

3.3 Detection of hydration bands

As stated in Sect. 1.4, spectra of primitive asteroids present diagnostic features associated with more or less aqueous alteration, and identified for the first time using ECAS data (Vilas & Gaffey 1989). One of this features, a shallow absorption band centered around 0.7 μm, is related to the presence of aqueously altered minerals in the asteroid's surface. The 0.7 μm band, present in the

spectra of a fraction of primitive asteroids, helped us to map the aqueous alteration frequency within the asteroid families.

In order to study this aqueous alteration feature in the families, we developed a detection pipeline, based on previous works (Carvano et al. 2003; Fornasier et al. 2014), that allows us to detect this hydration band within the limits of the signal to noise ratio of the spectra. This detection method was first used for the analysis of the Erigone family (see Chapter 4). For the subsequent analysis of the Sulamitis and Clarissa families (Chapter 5), the detection pipeline was improved. We describe here this improved version of the method.

The pipeline takes as input the normalized reflectance spectra of the observed asteroids, and it can be summarized in the following steps:

1. We randomly remove 10% of the points from the spectrum.

2. We compute a fourth-order polynomial fit to the spectrum (0.5–0.9 μm).

3. We also compute the continuum of the spectrum. This is done by fitting a straight line tangent to the polynomial fit in the local maxima (around 0.55 μm and 0.87 μm), which are the limits of the 0.7 μm absorption band. In some cases, the polynomial fit did not have one of the two local maxima, although the absorption band was clearly seen in the spectrum. For such cases, we just use the reflectance values in the regions delimiting the band (0.54–0.56 μm on the left side and 0.86–0.88 μm on the right), and compute a straight line.

4. Once the continuum is fitted, we remove it from the spectrum by dividing the reflectance data by the continuum straight line.

5. We repeat steps 3 and 4 once, in order to accurately remove the continuum slope from the spectrum.

6. Running a Monte Carlo simulation, we repeat 1000 times steps 1 to 5, computing each time the depth and the central wavelength position of the absorption band. The central wavelength position corresponds to the position of the local minimum of the band after the continuum removal. The band depth is computed as the difference, in %, between a reflectance value of 1 and the reflectance value at this minimum.

7. The final values for the band depth and central wavelength are computed as the mean values obtained for the full Monte Carlo run, and the errors are the corresponding 1σ standard deviations of the mean.

8. We compute the standard deviation of the fit residuals within the band (i.e., the fourth order polynomial fit minus the spectrum, between 0.53 and 0.84 μm), and then we compare this result with the mean value obtained for the band depth. Whenever the computed band depth is larger (considering its associated error) than the computed residual, we consider that the band is real (positive detection). On the contrary, cases where the depth is smaller than the residual, are considered as negative detections (no band).

9. Those cases where the value of the residual is inside the interval of the band depth $\pm$ its corresponding error are marked as dubious, needing for visual inspection to decide if the band is real or not.

A graphical representation of this procedure is shown in Fig. 3.4. Although both previous and current versions of the pipeline yielded similar results, we consider that the current version of the detection method follows a more rigurous approach, as it takes into account the signal to noise ratio of each spectrum individually, rather than establishing an a-priori detection threshold based on the noise level of the data.

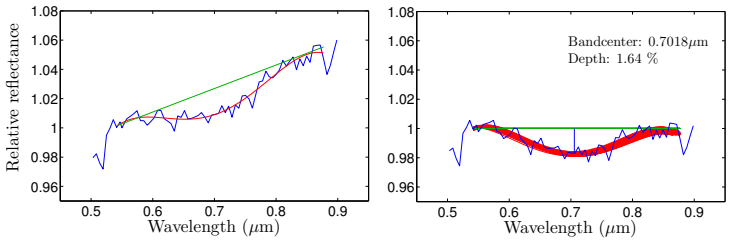

Figure 3.4: Graphical representation of the detection method followed to compute the central wavelength position and depth of the 0.7 μm absorption band on the spectra of asteroid (72384). Left panel shows the straight line (green) used to remove the continuum from the fitted absorption band (red curve). Right panel shows the result of this continuum removal and the iterative procedure using a Monte Carlo model to compute the band parameters. Extracted from Morate et al. (2016).

3.4 The MOVIS catalog

In 2016 our group published the first version of the Moving Objects from VISTA (MOVIS) catalog, a database with near-infrared photometry in four infrared

filters (Y,J,H and Ks), which provides information for 39 947 Solar System objects (Popescu et al. 2016).

This catalog was created using the data obtained by a survey in the near-infrared, performed by the VISTA (Visible and Infrared Survey Telescope for Astronomy) telescope. This is a wide field survey telescope, located at the Cerro Paranal Observatory in Chile, with a mirror diameter of 4.1 m. It is equipped with a 1.65° field of view near-infrared camera, and with the broad band filters Z, Y, J, H, and Ks. Six large public surveys are running on VISTA (Sutherland et al. 2015): UltraVISTA, VIKING (VISTA Kilo-Degree Infrared Galaxy Survey), VMC (VISTA Magellanic Survey), VVV (VISTA Variables in the Via Lactea), VHS (VISTA Hemisphere Survey), and VIDEO (VISTA Deep Extragalactic Observations Survey). These surveys aim to provide data for several fields, ranging from low-mass stars to large-scale structure of the Universe, covering different sky areas and depths. The MOVIS catalog was created using data from the VISTA-VHS, which aims to cover the largest sky area out of the six running surveys, around 19 000 square degrees in the southern hemisphere (McMahon et al. 2013).

The pipeline used to retrieve photometric data of moving objects from this survey provided a set of three catalogs, which are already available at the CDS[9] the detections catalog (MOVIS-D), the magnitudes catalog (MOVIS-M), and the colors catalog (MOVIS-C). The full process to obtain the catalogs is explained in Popescu et al. (2016). In short, this pipeline finds the objects based on their ephemeris, then cross-checks this information with the VHS data, removes wrong associations, and does a post-processing: it combines and averages the photometric data, and then it computes the colors of the objects. The reliability of the pipeline is evaluated by investigating the error distributions and comparing the results with the data in the 2MASS catalog. The first version of the MOVIS catalog presented data corresponding to 39 947 Solar System objects. This version was built over a data release that covered approximately 40% of the total planned VISTA-VHS survey.

The analysis that we carried out in Chapter 6 was performed using an updated version of the MOVIS catalog, based on the VHSv20161007 data release of the VISTA-VHS survey. This updated version of the catalog presented photometric data for 53 436 asteroids: 57 NEAs, 431 Mars Crossers, 612 Hungaria asteroids, 51 381 main belt asteroids, 218 Cybele asteroids, 267 Hilda asteroids, 434 Trojans, 7 Centaurs, and 29 Kuiper belt objects.

In Figure 3.5 we show the sky coverage of the VHSv20161007. This accounts

[9] Centre de Données astronomiques de Strasbourg (Strasbourg astronomical Data Center): http://cds.u-strasbg.fr

for approximately 14 200 square degrees, or about 75% of the original area that the survey intends to cover. At the moment this thesis is being written, the survey operations have already finished. We expect to find between 60 000 and 70 000 Solar System objects in the final version of the MOVIS catalog.

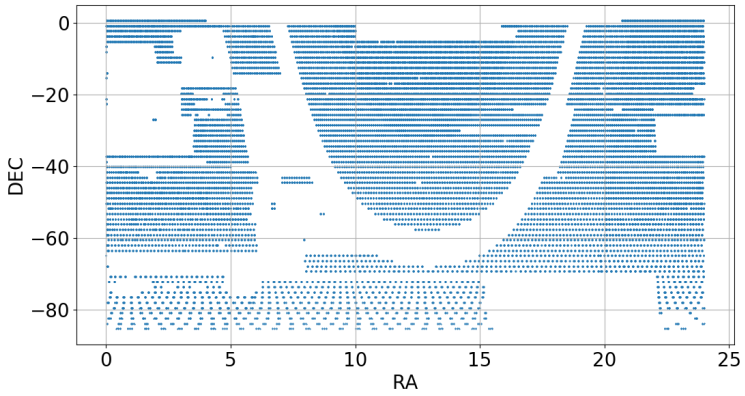

Figure 3.5: Sky coverage of the VISTA-VHS data release that we used to carry out the analysis in Chapter 6. Each point in this plot is one telescope pointing to obtain images with a 1.65° field of view.

A first analysis on the data of the MOVIS-C catalog is carried out in Popescu et al. (2016). As seen there, the colors in the MOVIS catalog allow us to separate between different compositional groups, mainly C-, S-, and V-type asteroids (or as stated in Chapter 6, primitive, rocky, and basaltic).

Out of the several color-color diagrams represented in Popescu et al. (2016), the one that best separates these three main groups of asteroids in the inner belt is the one shown in Fig. 3.6. The straight line in the right panel is computed by performing a linear fit to the colors of some objects with known taxonomic types, located just on each side of this S/C division (Fig. 3.6, left panel). The linear fit obtained follows the expression

$$(Y - J) = 0.412^{\pm 0.046}(J - Ks) + 0.155^{\pm 0.016} \tag{3.1}$$

Here we can see that there is a clear separation between three clusters of points, which are linked to C/X-types, S-types, and V-types. Based on this color-color diagram, we decided to create a near-infrared parameter, the ML^*, using the data in the MOVIS-C catalog to simplify the study of the asteroid

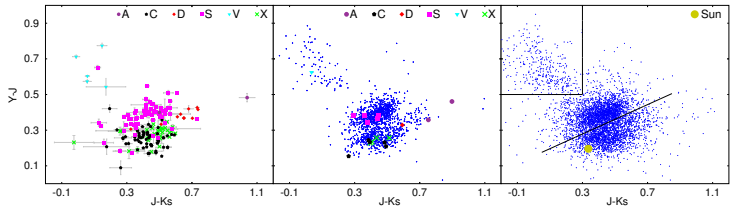

Figure 3.6: $(J-K)$ vs. $(Y-J)$ plots of the MOVIS-C data for different cases: the colors of asteroids with visible spectra, having an assigned taxonomic type (left panel), the colors computed for the template spectra of the taxonomic classes from DeMeo et al. (2009) compared with the MOVIS-C data with color errors less than 0.033 (central panel), and the MOVIS-C data obtained with a color error less than 0.1 compared to the colors of the Sun (right panel). Adapted from Popescu et al. (2016).

families present in the MOVIS catalog: we transformed a 2D-space into a 1D-space, providing a faster approach to the analysis of overall family composition.

The definition and computation of the ML^* parameter is detailed in Chapter 6. A graphical representation of this parametrization is shown in Fig. 3.7. We give here a brief description on the obtention procedure:

1. We selected the subset of asteroids with computed colors $(Y-J)$ and $(J-Ks)$ having errors smaller than some determined threshold.

2. On this subset, several density estimations using different resolutions were performed on its $(Y-J)$ vs. $(J-Ks)$ diagram. Then, we computed the positions of the density maxima for the two main clusters present in the diagram, associated with rocky and primitive asteroids (Popescu et al. 2016).

3. We then computed the angle between the line that connects these two maxima and the x-axis. Next, we rotated the system according to this angle, selecting the new y-axis as our parameter.

4. We arbitrarily forced our parameter to be zero at the separation between the two main clusters. To do this, we performed a new density estimation, computing the required offset selecting the point of minimum density between the two peaks of this unidimensional distribution.

The final defintion of our near-infrared parameter was

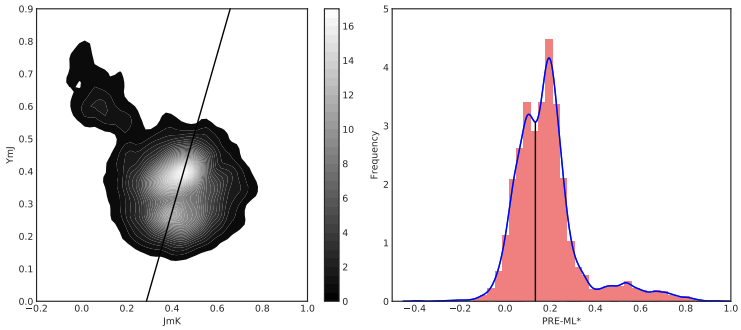

Figure 3.7: Graphical representation of the procedure followed to parametrize the near-infrared colors in MOVIS. The left panel shows the density estimation plot of the $(J-K)$ vs. $(Y-J)$ diagram. Brighter regions correspond to higher density of points. The straight line connects the two main cluster centers (peaks of maximum density). The third cluster $(Y-J>0.5)$ corresponds to basaltic asteroids. The right panel shows the unidimensional density estimation for the ML^* before the computation of the required offset. The vertical black line indicates the point where the density is minimum between the two maxima. Extracted from Morate et al. (2018b).

$$ML^* = 0.931(Y-J) - 0.364(J-Ks) - 0.142 \tag{3.2}$$

We note that, for the case where $ML^* = 0$, Eq. 3.2 is almost coincident with Eq. 3.1.

The ML^* alone allows us, via Kolmogorov-Smirnov tests on the parameter distribution, to distinguish between four different asteroid populations: two primitive (that we denoted as P1 and P2), one rocky, and one basaltic population. This provided a simple compositional characterization of the families with enough observed members (and good enough data quality) within the MOVIS catalog.

Chapter 4

Compositional study of asteroids in the Erigone collisional family using visible spectroscopy at the 10.4 m GTC

In this first paper we conducted a dedicated survey, using the 10.4 m Gran Telescopio Canarias, to obtain spectra of 101 asteroids from the Erigone primitive family. This collisional family is one of the possible sources of the targets of space missions OSIRIS-REx and Hayabusa 2, (101955) Bennu and (162173) Ryugu, respectively. We characterized this family to constrain its possible relationship with these asteroids. We also developed a pipeline, based on previous works, to detect absorption bands related to hydrated minerals in the spectra of the observed primitive objects.

A&A 586, A129 (2016)
DOI: 10.1051/0004-6361/201527453

Astronomy & Astrophysics

Compositional study of asteroids in the Erigone collisional family using visible spectroscopy at the 10.4 m GTC

David Morate[1,2], Julia de León[1,2], Mário De Prá[3], Javier Licandro[1,2], Antonio Cabrera-Lavers[1,4], Humberto Campins[5], Noemí Pinilla-Alonso[6], and Víctor Alí-Lagoa[7]

[1] Instituto de Astrofísica de Canarias (IAC), C/vía Láctea s/n, 38205 La Laguna, Tenerife, Spain
e-mail: damog@iac.es
[2] Departamento de Astrofísica, Universidad de La Laguna, 38205 La Laguna, Tenerife, Spain
[3] Observatório Nacional, Coordenação de Astronomia e Astrofísica, 20921-400 Rio de Janeiro, Brazil
[4] GTC Project Office, 38205 La Laguna, Tenerife, Spain
[5] Physics Department, University of Central Florida, PO Box 162385, Orlando, FL 32816-2385, USA
[6] Department of Earth and Planetary Sciences, University of Tennessee, Knoxville, 37996 TN, USA
[7] Laboratoire Lagrange, OCA, Boulevard de l'Observatoire, BP 4229 06304 Nice Cedex 04, France

Received 25 September 2015 / Accepted 10 December 2015

ABSTRACT

Two primitive near-Earth asteroids, (101955) Bennu and (162173) Ryugu, will be visited by a spacecraft with the aim of returning samples back to Earth. Since these objects are believed to originate in the inner main belt primitive collisional families (Erigone, Polana, Clarissa, and Sulamitis) or in the background of asteroids outside these families, the characterization of these primitive populations will enhance the scientific return of the missions. The main goal of this work is to shed light on the composition of the Erigone collisional family by means of visible spectroscopy. Asteroid (163) Erigone has been classified as a primitive object, and we expect the members of this family to be consistent with the spectral type of the parent body. We have obtained visible spectra (0.5–0.9 μm) for 101 members of the Erigone family, using the OSIRIS instrument at the 10.4 m Gran Telescopio Canarias. We found that 87% of the objects have typically primitive visible spectra consistent with that of (163) Erigone. In addition, we found that a significant fraction of these objects (~50%) present evidence of aqueous alteration.

Key words. minor planets, asteroids: general – methods: data analysis – techniques: spectroscopic

1. Introduction

Primitive asteroids are considered to be composed of the most pristine materials in the Solar System, being remnants of the processes that followed the condensation of the protoplanetary nebula and the formation of the planets. The materials on these objects have been altered over time by different processes, such as space weathering and aqueous alteration (Fornasier et al. 2014). Aqueous alteration mainly acts on primitive asteroids (C, B, and low-albedo X-types, according to the DeMeo et al. (2009) classification scheme), producing a low-temperature (<320 K) chemical alteration of the materials that is due to the presence of liquid water. This water acts as a solvent and generates hydrated materials such as phyllosilicates, sulfates, oxides, carbonates, and hydroxides. The presence of hydrated materials thus implies that liquid water was present in the primordial asteroids, produced by the melting of water ice by a heating source (Fornasier et al. 2014). The most unambiguous indicator of hydration is the 3 μm hydration band observed in infrared photometry and spectroscopy of many primitive asteroids. This feature is correlated with the 0.7 μm $Fe^{2+} \rightarrow Fe^{+3}$ oxidized iron absorption band observed in the visible spectra of these asteroids (Vilas 1994; Howell et al. 2011; Rivkin 2012).

Except for this aqueous alteration, primitive asteroids have undergone minimal geological or thermal evolution, experiencing, on the contrary, an intense collisional evolution that affected their shape, size, and surface composition. Therefore, studying the products of these collisional events and their mineralogical compositions will shed light on the evolutionary history of the Solar System.

Asteroid collisional families are groups of asteroids sharing very similar orbital properties (Hirayama 1918) that are thought to be the direct result of energetic collisional events. Spectroscopic observations provided the first confirmation of the collisional origin of a family: the Vesta family (Binzel & Xu 1993). The number of spectroscopic studies of collisional families has steadily increased since then, focusing on the characterization of their mineralogy. Additionally, considering that near-Earth asteroids (NEAs) come primarily from the main asteroid belt (Bottke et al. 2002), collisional families are good sources of NEAs, as they generate plenty of small fragments during their formation. Families located close to particular resonances in the belt can easily send these fragments to the near-Earth space. In this sense, the inner asteroid belt (the region located between the ν_6 resonance, near 2.15 AU, and the 3:1 mean-motion resonance with Jupiter, at 2.5 AU) is considered as a primary source of NEAs (Bottke et al. 2002).

The NASA OSIRIS-REx (Lauretta et al. 2010) and JAXA[1] Hayabusa 2 (Tsuda et al. 2013) sample-return missions have targeted two NEAs: (101955) Bennu and (162173) Ryugu,

[1] Japan Aerospace Exploration Agency.

A&A 586, A129 (2016)

respectively. These are primitive asteroids that are believed to originate in the inner belt, where five distinct sources have been identified: four primitive collisional families (Polana, Erigone, Sulamitis, and Clarissa) and a population of low-albedo and low-inclination background asteroids (Campins et al. 2010, 2013; Bottke et al. 2015). Identifying and characterizing the populations from which these two NEAs might originate will enhance the science return of both missions.

With this main objective in mind, we initiated a spectroscopic survey in the visible and the near-infrared in 2010 to characterize the primitive collisional families in the inner belt and the low-albedo background population (PRIMitive Asteroid Spectroscopic Survey, PRIMASS). We started with the largest one, the Polana family (Pinilla-Alonso et al. 2016; de León et al. 2016), using, among others, visible spectra obtained with the 10.4 m Gran Telescopio Canarias, which is located at the El Roque de los Muchachos Observatory on the island of La Palma (Spain). We found that despite the dynamical and collisional complexity of the Polana family (Walsh et al. 2013; Milani et al. 2014; Dykhuis & Greenberg 2015), there is a spectral homogeneity both in the visible and near-infrared wavelengths: all the asteroids show a continuum in spectral slopes from blue to moderately red that is typical of B- and C-type primitive asteroids.

To continue with the PRIMASS survey, we have observed and characterized the Erigone family, the second largest of the four primitive collisional families in the inner belt. We have performed our analysis using data obtained with the 10.4 m Gran Telescopio Canarias during the semester 2014B (September 2014–February 2015). In Sect. 2 we describe the observations and the data reduction. In Sect. 3 we present the analysis performed on the data, including taxonomical classification, computation of spectral slopes, and analysis of aqueous alteration. In Sect. 4 we discuss the obtained results, and in Sect. 5 we summarize the conclusions.

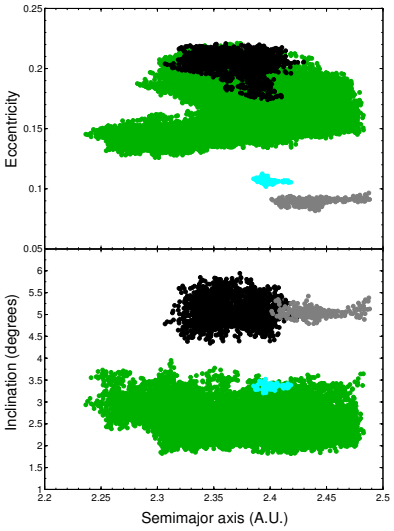

Fig. 1. Proper semimajor axis (a) versus proper eccentricity (e) and proper inclination (i) for the primitive asteroid families in the inner main belt. The Erigone family is depicted in black. The Polana (Nysa-Polana complex in this plot), Sulamitis, and Clarissa families are depicted in green, gray, and cyan, respectively.

2. Observations and data reduction

The sample of asteroids we observed in this study has been selected using the Minor Planet Physical Properties Catalogue[2] (MP^{3}C), which acknowledges the NASA Planetary Data System (PDS) as a data source. Orbital data of the asteroid families are extracted from a dataset containing asteroid dynamical families including both analytic and synthetic proper elements. These families were computed by David Nesvorny (Nesvorny 2012) using his code based on the hierarchical clustering method (HCM), as described in Zappala et al. (1990) and Zappala & Cellino (1994). The MP^{3}C catalog also provides information on the absolute magnitude H, the diameter D, and the geometric albedo p_V. For the diameters and albedos we used the values provided by WISE (Wide-field Infrared Survey Explorer, Masiero et al. 2011). Family membership is based on values of the synthetic proper elements, that is, on the semimajor axis (a), eccentricity (e) and inclination (i), and also on the absolute magnitude as a function of semimajor axis (a, H). According to these parameters, the Erigone family contains a total of 1785 asteroids.

The selection criterion was quite simple. The Erigone collisional family is a primitive one according to the information we currently have: from the list of 1785 members of the family, 1015 have no albedo information, but from the remaining 770 objects, 692 have geometric albedo values $p_V < 0.1$. In addition, 156 objects have SDSS color-based taxonomies, the majority of them belonging to primitive classes (91 C-types, 10 B-types, 7 X-types, 39 S-types, 5 L-types, 2 K-types, 1 V-type, and 1 A-type). Therefore, we selected those asteroids with geometric albedo $p_V < 0.1$. Observations were made in service mode on different nights (see details in the next section). From the previous list of asteroids, we selected those with an apparent visual magnitude in the range $18 < m_V < 21$ for a good compromise between the number of asteroids observed and the signal-to-noise ratios of the spectra. This means that for some of the nights there were no visible asteroids fulfilling these criteria. In these cases (16 in total), we first tried to find objects with an SDSS color-based taxonomical classification available (preferentially C-types). When this information was not available, we selected objects with $p_V > 0.1$. Our last option was to select objects without information on their albedo. We describe this small subsample in detail in Sect. 3.

[2] http://mp3c.oca.eu/MP3C/

2.1. Observations

We obtained low-to-intermediate resolution visible spectroscopy for a total of 101 asteroids using the Optical System for Imaging and Low Resolution Integrated Spectroscopy (OSIRIS) camera spectrograph (Cepa et al. 2000; Cepa 2010) at the 10.4 m Gran Telescopio Canarias (GTC), located at the El Roque de los Muchachos Observatory (ORM) in La Palma, Canary Islands, Spain. The OSIRIS instrument consists of a mosaic of two

Marconi CCD detectors, each with 2048 × 4096 pixels and a total unvignetted field of view of 7.8×7.8 arcmin. The single pixel physical size is 15 μm, giving a plate scale of 0.127″/pix. To increase the signal-to-noise ratio for our observations, we selected the 2 × 2 binning mode with a readout speed of 200 kHz (which has a gain of 0.95 e-/ADU and a readout noise of 4.5 e-), which corresponds to the standard operation mode of the instrument.

All the spectra were obtained using the OSIRIS R300R grism, which produces a dispersion of 7.74 Å/pix for a 0.6″ slit (in the worst-case scenario, a seeing of 3.0″ would translate into a resolution of 38.7 Å/pix), with a spectral coverage from 4800 to 10 000 Å. The R300R grism is used in combination with a second-order spectral filter. However, the spectrum is still slightly contaminated, with a distinguishable contribution for wavelengths at 4800–4900 Å and 9600–9800 Å. To be conservative, we therefore did not consider data beyond 9000 Å here. A 5.0″ slit was used to account for possible variable seeing conditions, and it was oriented to the parallactic angle to minimize loses due to atmospheric dispersion. Series of three spectra (whenever possible) were taken for all the targets, with exposure times ranging from 150–600 s, depending on the target brightness. Observational details are listed in Table C.1. Information includes asteroid number, date of observation, starting UT, airmass, exposure time, solar analog stars, and seeing at the moment of the observations. Consecutive spectra were shifted in the slit direction by 10 arcsecs to improve the sky subtraction and fringing correction.

Observations were made in service mode (within GTC programs GTC39-14B and GTC18-15A) on different nights from September[3] 2014 to May 2015. Night conditions were very variable, covering a wide range of different weather conditions. This was because the program was classified as a "filler" (*C* band) program within the GTC nightly operation schedule. The aim of this type of program is to obtain spectra with a high signal-to-noise ratio for targets that are relatively bright for a 10 m-class telescope such as GTC in non-optimal weather conditions, which would include a high seeing value (higher than 1.5 arcsec), bright moon, or some cirrus coverage. Because of this, spectra quality might vary from one night to another (see Table C.1, last column). Since the weather conditions (i.e., clouds, sky brightness, etc.) are the main constraint during the observation, this variation is unrelated to the target brightness. For completeness, we included in this study the visible spectra of asteroids (163) Erigone, the parent body of the family, and (571) Dulcinea, the second largest asteroid in the family, both from the SMASS II catalog[4]. There were no other asteroids from the Erigone family with published visible spectra. All in all, our sample of asteroids from the Erigone collisional family includes a total of 103 objects.

2.2. Data reduction

A reduction pipeline for asteroid spectroscopic data obtained with the GTC was developed to optimize the reduction process. This pipeline combines standard IRAF[5] tasks and some MATLAB functions.

[3] Some of the asteroids were observed during August 2014 upon request from the GTC operations team to fill observational gaps during particular nights.
[4] Available at http://smass.mit.edu/catalog.php
[5] IRAF is distributed by the National Optical Astronomy Observatories, which are operated by the Association of Universities for Research in Astronomy, Inc., under cooperative agreement with the National Science Foundation.

Table 1. Equatorial coordinates of the solar analog stars used to obtain the reflectance spectra of the observed asteroids.

ID	Star	α	δ
1	SA 93-101	01:53:18.0	+00:22:25
2	SA 98-978	06:51:34.0	–00:11:28
3	SA 102-1081	10:57:04.4	–00:13:10
4	SA 110-361	18:42:45.0	+00:08:04
5	SA 112-1333	20:43:11.8	+00:26:15
6	SA 115-271	23:42:41.8	+00:45:10
7	SA 107-998	15:38:16.4	+00:15:23

With the IRAF tasks included in our pipeline, images were initially bias- and flat-field corrected using lamp flats from the GTC instrument calibration module. Sky background was then subtracted, and a one-dimensional spectrum was extracted with an extraction aperture that varied depending on the seeing of the corresponding night. After the extraction, the one-dimensional spectra were wavelength calibrated with Xe+Ne+HgAr lamps. As a final step, the three spectra of the same object, when available, were averaged to obtain one final spectrum of the asteroid.

To correct for telluric absorptions and obtain relative reflectance spectra, at least one solar analog star from the Landolt catalog (Landolt 1992) was observed each night. When possible, more than one solar analog star was observed to improve the quality of the final spectra and to minimize potential variations in spectral slope introduced by the use of one single star. These stars were observed using the same spectral configuration as for the asteroids, and at a similar airmass. The list of the solar analogs used in this study is shown in Table 1.

The MATLAB routines in our pipeline were used to align the spectra of the objects and the corresponding solar analog with the theoretical wavelength positions of the telluric lines at 6867.19 and 7593.70 Å. After they were aligned, the spectrum of the object was divided by that of the solar analog, and the result was normalized to unity at 0.55 μm. When more than one solar analog was observed, we divided the spectrum of the asteroid by the spectra of the stars and checked against any possible variations in spectral slopes, which were on the order of 0.6%/1000 Å. A variation smaller than 1%/1000 Å is typically considered as a good value.

After we obtained the final spectrum for each object, we applied a binning to each spectrum, taking intervals of 11 points as the bin size. Then, the reflectance value corresponding to the central wavelength of the bin size was substituted with the median reflectance value to avoid spectral disturbances, and thus making the resulting spectrum more robust. To choose the binning size, we selected the worst spectrum in our sample and applied different binning sizes until its quality improved. Since the finest spectral feature we wished to measure, the 0.7 μm band, has an approximate width of 2000 Å, we consider that the selected binning is sufficient to improve the quality of the spectra and to not affect the obtained results. The spectral range extends from 0.5 to 0.9 μm, with a step of 0.0055 μm. Spectra are shown in Figs. A.1 and B.1.

3. Analysis and results

After computing the final spectra, a taxonomic classification was made using M4AST[6], which is an online tool for modeling asteroid spectra (Popescu et al. 2012). The method used by the

[6] http://m4ast.imcce.fr/

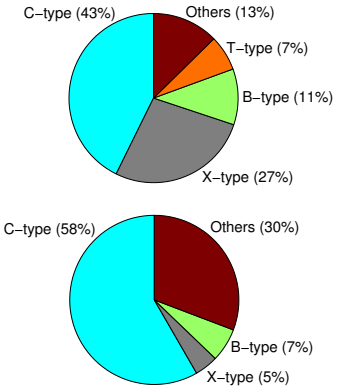

Fig. 2. Distribution of the taxonomical classes for the Erigone family. The *top panel* shows the distribution for the sample of 103 asteroids we studied here. The *bottom panel* shows the distribution for the color-based taxonomy from the SDSS data (the X class in the SDSS classification includes the T-type from the Bus taxonomy). The "Others" class includes all non-primitive taxonomies (S-types, V-types, and L-types).

M4AST tool to classify asteroid spectra is the following: first, the spectrum is fitted with a polynomial curve, and then this curve is compared to each of the classes defined by the DeMeo et al. (2009) taxonomy at the corresponding wavelengths. The tool then selects the taxonomical class producing the smallest standard deviation.

We worked with spectra in the visible wavelength range and therefore applied the Bus & Binzel (2002) taxonomy, in which most of the classes overlap with those of DeMeo et al. (2009). We individually checked those cases in which the taxonomical classes were exclusive to the DeMeo et al. (2009) taxonomy and visually classified them according to Bus & Binzel (2002).

To obtain robust results, both original and binned spectra were classified using the M4AST tool. A χ^2 method (Bevington & Robinson 1992) was used to test how well the spectra fit the templates. The chosen result corresponded to the smallest standard deviation. Whenever a spectrum was very different from the best-fitting template, or when the standard deviations were very similar for two or more taxonomical classes, we simplified the method: the binned spectrum was fit to a third-order polynomial, and then the procedure was repeated. The taxonomical classification obtained for each asteroid is shown in the last column of Table C.2.

The classification yielded a total of 44 C-type asteroids (including the subclasses Cb, Cg, Ch, and Cgh), 28 X-type asteroids (and subclasses Xc and Xk), 11 B-types, 7 T-types, and 13 objects with non-primitive classifications: 6 S-types (and subclasses), 1 V-type, and 6 L-types. These results are illustrated with a pie chart in Fig. 2 (upper panel). As expected from our selection criterion (objects with $p_V < 0.1$), the majority of the asteroids belong to primitive taxonomical classes (C-, B-, X-, and T-). As mentioned in Sect. 2 and because of observational constraints, 16 asteroids from the 101 observed did not fulfill the selection criteria. Their taxonomical classification is shown in Table 2. Moreover, the three asteroids with $p_V > 0.1$ correspond to non-primitive classes. The remaining ten asteroids without albedo information show a mixture of taxonomies, with two C-types, two X-types, two S-types, three L-types, and one V-type. From the total of 86 asteroids with $p_V < 0.1$, only one single object has a non-primitive classification, which is an L-type.

Table 2. Asteroids in our sample without information on their visible geometric albedo or whose albedo value is higher than 10% ($p_V > 0.1$).

Asteroid	p_v	SDSS Class.	M4AST Class.
38661	–	S	Sr
39895	–	S	S
56349	–	C	B
186446	–	C	Ch
18759	0.303	–	Sr
24037	0.129	–	L
132383	0.356	–	L
38106	–	–	L
50068	–	–	L
66403	–	–	Ch
69706	–	–	S
70511	–	–	V
76922	–	–	Xk
85727	–	–	S
107070	–	–	L
166264	–	–	Xk
186446	–	–	Ch

To perform one final comparison with the taxonomical distribution we found from our visible spectra, we searched for all the asteroids in the Erigone family with an SDSS color-based taxonomy. A total of 156 objects belonging to the Erigone family were classified according to (DeMeo & Carry 2013). In the lower panel of Fig. 2 we show their taxonomic distribution. The proportion of C- and B-types from our sample and the one from the SDSS taxonomy agree well: the proportion of X-type asteroids is significantly larger in our case. The difference between the two non-primitive distributions is probably due to the selection criterion ($p_V < 0.1$).

Figure 3 shows the distribution in the (a, H) space of the 1785 asteroids that have been identified as members of the Erigone collisional family (gray circles). As described by Vokrouhlický et al. (2006), the family shows signs of having experienced dynamical spreading through Yarkovsky thermal forces. Solid curves in Fig. 3 define the boundaries of the family, also known as the Yarkovsky cone, which is computed using the following expression:

$$0.2H = \log_{10}(\Delta a/C),$$

where $\Delta a = a - a_c$, with a_c defined as the center of the family. In practice, a_c is often close to, or the same as, the semimajor axis of the largest member of the family, in this case, asteroid (163) Erigone (Vokrouhlický et al. 2006; Bottke et al. 2015). Bottke et al. (2015) showed that for the Erigone family, $C = 1.9 \times 10^{-5}$. This Yarkovsky cone is basically an envelope around the center of the family, indicating the farthest distance that a family member can drift as a function of its size. Objects outside this cone are most likely family interlopers. Figure 3 shows the position, with respect to this cone, of the asteroids studied in this work. Different colors are associated with different spectral classes, as indicated in the legend of the figure. It is interesting to note that

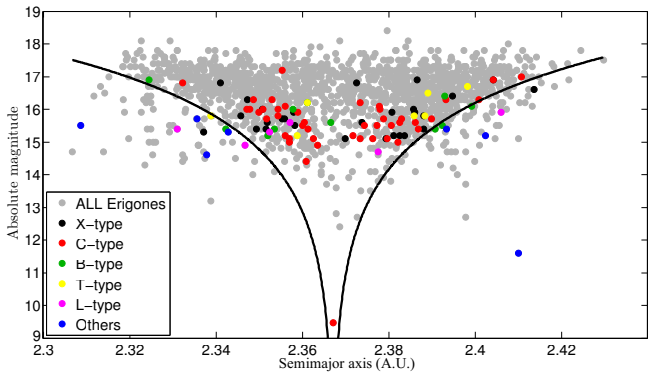

Fig. 3. Absolute magnitude (H) of the asteroids from the Erigone family as a function of their proper semimajor axis. The Erigone family (a total of 1785 objects) is shown in gray. The colored circles correspond to the different taxonomical classes found for our sample of 103 members: C-types (red), X-types (black), B-types (green), T-types (yellow), and the remaining non-primitive classes (S-types, L-types, and V-types, in blue). The solid lines represent the boundaries of the family (so-called Yarkovsky cone). The object with the lowest value of H that is located at the bottom of this cone is the parent body of the family, asteroid (163) Erigone.

most of the asteroids with non-primitive taxonomies fall outside the family boundaries, confirming that they are most likely interlopers.

In the following sections we perform a more detailed analysis of the asteroids of the Erigone family with a primitive taxonomical classification, that is, C-, X-, B-, and T-types. A total of 90 objects have been analyzed.

3.1. Spectral slopes

Given that primitive asteroids have featureless, linear spectra, we started by computing the spectral slope S', as defined by (Luu & Jewitt 1990), between 0.55 and 0.90 μm:

$$S' = \left(\frac{\mathrm{d}S/\mathrm{d}\lambda}{S_{0.55}}\right),$$

where $\mathrm{d}S/\mathrm{d}\lambda$ is the rate of change of the reflectivity in the aforementioned wavelength range, and $S_{0.55}$ is the reflectivity at 0.55 microns. To compute it, a linear least-squares fit between 0.55 and 0.90 μm was applied to every primitive asteroid spectra. We normalized[7] the slope at 0.55 μm. S' is measured in units of %/1000 Å. The resulting values for the computed spectral slopes are shown in Table C.3. The slope errors take into account both the 1σ uncertainty of the linear fit and the variation of 0.6%/1000 Å, which is attributable to the use of different solar analog stars during the night (see Sect. 2.2 for more details). Figure 4 shows the distribution of the computed slopes for the 90 primitive objects of the Erigone collisional family (red). As a comparison we show the distribution of the visible spectra slopes of the asteroids of the Polana family (blue) from de León et al. (2016), which are compatible with a B-type parent. The two distributions are significantly different, with the asteroids of the Erigone family showing redder spectral slopes in general.

[7] This is the central wavelength of the Johnson V filter, which is usually used as normalization reference.

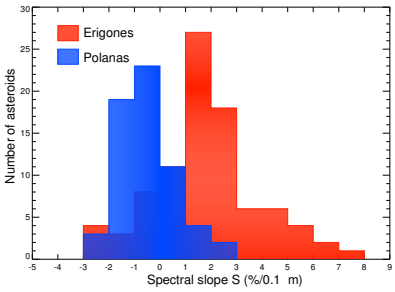

Fig. 4. Histogram showing the distribution for the values of the spectral slope for the primitive asteroids in the Erigone family (red). The distribution of the slopes of the asteroids of the Polana family from de León et al. (2016) is shown in blue as a comparison.

3.2. Aqueous alteration

Several studies (Vilas 1994; Fornasier et al. 1999; Carvano et al. 2003; Rivkin 2012; Fornasier et al. 2014) showed that a considerable number of main belt primitive asteroids present an absorption feature around 0.7 μm attributed to charge transfer transitions in oxidized iron (Vilas & Gaffey 1989; Vilas 1994; Barucci et al. 1998), which is indicative of, or associated with,

A&A 586, A129 (2016)

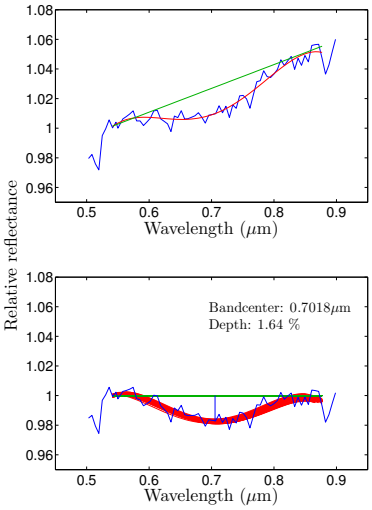

Fig. 5. Example figure of the process followed to compute the central wavelength position and depth of the 0.7 μm absorption band on the spectra of asteroid (72384). The *top panel* shows the straight line (green) used to remove the continuum from the fitted absorption band (red curve). The *bottom panel* shows the result of this continuum removal and the iterative procedure using a Monte Carlo model to compute the band parameters (see text for details).

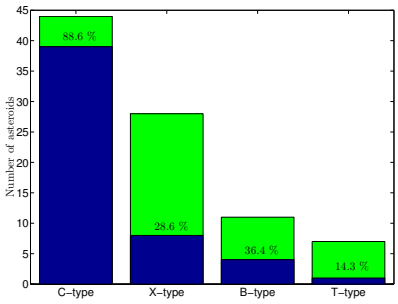

Fig. 6. Percentage of asteroids showing the 0.7 μm absorption band (dark blue) for each primitive taxonomic class (green).

aqueous alteration in the surface of these objects (i.e., presence of hydrated minerals). Fornasier et al. (2014) showed that (163) Erigone, the parent body of the family, presents this particular absorption feature at 0.7 μm, with a depth of 2.2 ± 0.1% with respect to the continuum. To search for said absorption feature among our Erigone family member spectra, we followed the procedure described in Carvano et al. (2003) with some minor adjustments. For objects that showed this feature, we characterize the central wavelength position and depth.

The first step was to compute the continuum of the absorption band by fitting a straight line tangent to the spectra at two positions, 0.54–0.56 μm and 0.86–0.88 μm, which are the limits of the 0.7 μm absorption band (green line in the top panel of Fig. 5). We tested slightly different ranges to compute the continuum, finding no significant changes in our results. Then, we fitted the spectrum in this interval using a fourth-order spline (red curve in the top panel of Fig. 5).

The final step was to remove the continuum by dividing the spline fit by the straight line we previously obtained (bottom panel of Fig. 5). To compute the depth and central wavelength position of the absorption band and their corresponding errors, we ran a Monte Carlo model with 1000 iterations, randomly removing ten points from the spectrum in the range from 0.54 to 0.88 μm at each iteration, then repeating the procedure. The band depth is computed as the difference, in %, between a reflectance value of 1 and the reflectance value corresponding to the central wavelength position. The final values for the band depth and central wavelength are computed as the mean values obtained for the full Monte Carlo run, and the errors are the corresponding 1σ standard deviations. The criterion for deciding whether an object showed an aqueous alteration band was to rule out objects that presented bands with a depth smaller than 1% or relative errors in the computation of the depth larger than 15%. The detection threshold of 1% corresponds to the peak-to-peak scatter in our spectra, which seems to be a better indicator of the spectrum quality than the calculated signal-to-noise ratio.

We have to note that there are some cases in which the detected bands have depths that are higher than expected. In these cases (in particular, that of asteroid 210564), high depth values arise because the absorption band is quite broad and the limiting regions are narrow and not perfectly defined. In the specific case of asteroid 210564, the band depth might vary from ~9% to ~5% if we were to change the continuum-fitting upper limits. This is because when we move the upper limit below 0.88 microns, we might fall already inside the band, which would produce heavy band depth shifts with small error bars. These special cases might reveal the limitations of our data (if we had information over 0.9 μm, the band limits would be clearer).

In Table C.3 we indicate for each asteroid the taxonomical classification, whether it has an absorption band at 0.7 μm (YES/NO), and the center and depth of the band, when present. We found that 52 of the 90 primitive asteroids present an absorption band at 0.7 μm and that this band is present regardless of the specific primitive spectral class. Figure 6 shows the proportion of asteroids with a hydration band for each primitive class. Almost all C-type asteroids present the hydration feature (~88%). This proportion is progressively smaller for B-types (~36%), X-types (~28.5%), and T-types (~14%). This decreasing trend in our results agrees with previous studies of the relative incidence of this feature in asteroids distributed throughout the main belt. Vilas (1994) found an incidence of 47.7% in C-type asteroids and 33% in B-types, while Fornasier et al. (2014) found an incidence of 50.7% in C-types and a 9.8% in B-types. The proportion of C-type asteroids showing the 0.7 μm absorption band is significantly larger in the Erigone family, with about 87% of the asteroids.

That there is a primitive collisional family, with all the observed objects located between 2.3 and 2.4 AU and with the majority of its members showing the 0.7 μm hydration band, agrees well with the results presented by Fornasier et al. (2014), who suggested that the aqueous alteration processes dominate in primitive asteroids located between 2.3 and 3.1 AU. Moreover, they stated that the proportion of hydrated primitive objects in the region where the Erigone family is located is 64%, which agrees very well with the proportion of hydrated objects we have found in our sample, which is 57.7% (52 out of 90).

We found no significant correlations between the band depths or the band centers and the taxonomical class, the asteroid orbital parameters, the albedo, or the size of the objects. A similar lack of correlations was found by Carvano et al. (2003) and Fornasier et al. (2014) in their respective studies for asteroids throughout the whole main belt. Additionally, the mean values we found for the band depth, 2.9 ± 1.5%, and the band center position, 7053 ± 160 Å, agree excellently well with those obtained by Fornasier et al. (2014): 2.8 ± 1.2% for the band depth and 6914 ± 148 Å for the band center. These results suggest that the values obtained for the parameters used to characterize the 0.7 μm hydration band are independent of the location of the asteroids in the main belt.

3.3. Comparison with spectra of (101955) Bennu and (162173) Ryugu

As we described in Sect. 1, the aim of characterizing the Erigone primitive family is that together with the Polana, Clarissa, and Sulamitis families and the low-albedo and low-inclination background asteroids, they are the most likely sources of the two NEAs that are the targets of the OSIRIS-REx and Hayabusa 2 sample-return missions: (101955) Bennu and (162173) Ryugu. Spectroscopic and photometric observations of these asteroids suggest that they are composed of primitive materials, pointing to an origin in the aforementioned populations, which is reinforced by the results of dynamical simulations (Campins et al. 2010, 2013; Bottke et al. 2015).

Spectral comparison might shed light upon the origins of the two asteroids, and we therefore compared the available visible spectra of asteroids (101955) Bennu and (162173) Ryugu with the data obtained in this work.

For (162173) Ryugu, several references in the literature show visible spectra of this small (~800 m), low-albedo (p_V = 0.07) NEA. A first spectrum from Binzel et al. (2001) shows an ultraviolet drop-off in reflectance shortward of 0.65 μm and provides a classification of Cg-type. Two other visible spectra were presented in Vilas (2008), obtained in July and September 2007. These two spectra were different from each other and also different from the spectrum reported by Binzel et al. (2001), which showed no ultraviolet drop-off. The spectrum obtained in July showed an absorption band at 0.7 μm and a red spectral slope, while the one obtained in September, with a much higher signal-to-noise ratio, presented a neutral slope and showed a marginal, very shallow absorption centered near 0.6 μm. According to Vilas (2008), these differences suggest that the surface of the asteroid covers the conjunction of two different geological units. A comparison between these three spectra can be seen in the left panel of Fig. 3 from Campins et al. (2013). Additional rotationally resolved visible spectra of (162173) Ryugu were presented by Lazzaro et al. (2013), Moskovitz et al. (2013), and Sugita et al. (2013), all of them compatible with a C-type classification and showing no absorption feature at 0.7 μm and a spectral slope similar to the September 2007 spectrum from Vilas (2008), making the suggestion of two different surfaces very unlikely. Because it is the spectrum with the highest signal-to-noise ratio, we therefore selected it to perform our spectral comparison. The upper panel of Fig. 7 shows the September 2007 (Vilas 2008) spectrum of Ryugu compared to the mean visible spectra of the asteroids of the Erigone family classified as C-types (and subclasses) in red, and those classified as B-types in blue. The visible spectrum of Ryugu agrees well with the mean spectrum of C-type asteroids in the Erigone family, even though it does not show the 0.7 μm absorption feature.

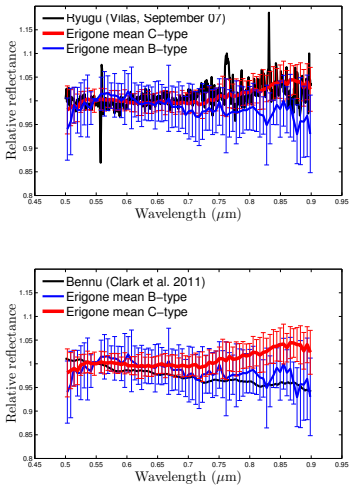

Fig. 7. Comparison between the September 2007 (Vilas 2008) visible spectrum of Ryugu in the top panel and the visible spectrum of (101955) Bennu from Clark et al. (2011) in the bottom panel, with the mean spectra of the C-type (red) and B-type (blue) asteroids in the Erigone family. The standard deviation of the mean ($\pm 1\sigma$) is shown with vertical lines.

Even if the signal-to-noise ratio is quite poor, we computed both the wavelength central position and band depth of the 0.7 μm absorption band present in the July 2007 spectrum of Ryugu (Vilas 2008). Our calculations yielded a depth of 11.7 ± 1.3% and a band center of 6870 ± 55 Å. The absorption band depth and band center are very different from the mean values computed by Fornasier et al. (2014) and also from those computed in this work for the asteroids in the Erigone family (see Sect. 3.2). Together with the absence of the 0.7 μm absorption band in all the subsequent visible spectra of Ryugu obtained by other authors, this suggests that the absorption band observed in the July 2007 spectrum from Vilas (2008) might be due to some artifact.

The only available visible data for the primitive (p_V = 0.043) and rather small (~500 m) NEA (101955) Bennu are found in Clark et al. (2011) and Hergenrother et al. (2013). Based on these studies, Bennu is classified as a B-type asteroid in the Bus & Binzel (2002) taxonomy. In addition, Binzel et al. (2015)

A&A 586, A129 (2016)

reported spectra obtained in the NIR range that showed spectral variability, which indicates a C-type class according to DeMeo et al. (2009). As has been shown in Clark et al. (2010) and de León et al. (2012), asteroids classified as B-types in the visible can present considerable slope variation in the NIR, from negative blue slopes to positive redder ones. The lower panel of Fig. 7 shows the visible spectrum of Bennu (black) compared to the mean visible spectra of the asteroids of the Erigone family classified as C-types (and subclasses) in red and those classified as B-types in blue, as observed in this work. From a visual inspection, the visible spectrum of Bennu seems to marginally show the presence of the hydration feature 0.7 μm. We followed the same approach as in the previous section to study the presence of a possible aqueous alteration band. Our calculations yielded the presence of a band centered at 7486 ± 76 Å, with a depth of 0.96 ± 0.02%. This depth is slightly below the threshold (1%) established for a positive detection, and the wavelength position of the band center is significantly different from the mean value found for the family (7053 ± 160 Å). Therefore, we rule out the presence of this hydration band in the spectrum of Bennu.

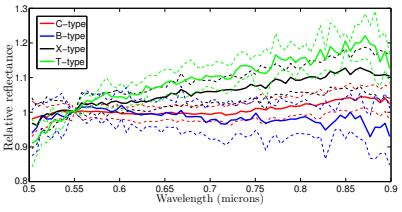

Fig. 8. Computed mean spectra of the asteroids in the Erigone family classified as C-types (red), B-types (blue), X-types (black), and T-types (green). The mean spectrum for each class is plotted as a thick line, while the ± 1σ of the mean is shown with dashed lines. The different mean spectra are well differentiated from one another.

4. Discussion

No previous spectroscopic studies have been performed until now on the Erigone primitive collisional family, with only two asteroids that were previously classified using visible spectroscopy: (163) Erigone, and (571) Dulcinea. We clearly showed that the asteroids we studied here are spectroscopically consistent with the hypothesis of a common parent body, and that this parent body is (163) Erigone, classified as a C-type asteroid. Moreover, (163) Erigone shares the particular spectroscopic feature at 0.7 μm with most of the family members. Another primitive collisional family in the inner belt, the Polana family, which together with Erigone, Sulamitis, and Clarissa, represents the four primitive families in the inner belt, has recently been studied by several authors (Walsh et al. 2013; Milani et al. 2014; Dykhuis & Greenberg 2015; de León et al. 2016; Pinilla-Alonso et al. 2016). Comparing our results on the Erigone family with those obtained from de León et al. (2016) for the Polana family, we observe two main differences.

a) The Erigone family presents a different distribution of taxonomical classes from that of the Polana family, referred to as the Polana-Eulalia complex in de León et al. (2016). In our sample, we found 44 C-type objects, 28 X-types, 11 B-types, and 7 T-types, plus 13 interlopers (S-types and L-types). The mean spectra for each class are clearly differentiated, especially in the X and T classes (see Fig. 8). In contrast, we found mainly C- (51%) and B-types (42%) in the Polana family, with a few X-types (5%) and only one S-type, with the mean spectra for the C-, B-, and X-types presenting similar values (de León et al. 2016). In addition, the slope distribution for the objects in the Erigone family is clearly redder than that of the Polana family, as can be seen in Fig. 4, which is mainly due to the larger fraction of X-types found in the former.
b) The majority of the primitive asteroids in the Erigone family (52 out of 90) show evidence of aqueous altered minerals on their surfaces. We conducted the same analysis as that described in Sect. 3.2 for the data in de León et al. (2016) and found that according to our criterion, only one object in the Polana family (asteroid 29626) showed the 0.7 μm absorption feature, with a band depth of 1.15±0.11% and a band center of 7300 ± 211 Å. This difference in the two families is well explained by their two parent bodies. Asteroid (142) Polana shows no signs at all of the hydration feature at 0.7 μm. On the other hand, (163) Erigone, the parent body of the Erigone family, shows evidence of aqueous alteration. Therefore, the presence of the hydration feature in the spectra of most of its family members is somewhat expected. An interesting explanation for the difference in hydration between the two families was presented by Matsuoka et al. (2015). They proposed that space weathering effects on C-type asteroids tend to make the 0.7 μm absorption feature less deep. Space weathering processes might have removed the aqueous alteration band in the Polana family, since the Polana family is older than Erigone: according to Bottke et al. (2015), Erigone is 130 ± 30 Myr old, while Polana (referred to as New Polana in their paper) and Eulalia are 1400 ± 150 Myr old, and 830^{+370}_{-100} Myr old, respectively.

To determine the likelihood that the Erigone family is the source for asteroids (101955) Bennu and (162173) Ryugu, we compared visible spectra of the two objects with the mean spectra of the primitive asteroids in the family. In our sample, we found approximately 56% of non-interlopers showing evidence of aqueous alteration. According to Bottke et al. (2015), there is little to no chance for the smaller families (Erigone, Clarissa, and Sulamitis) to be the source of these two asteroids:

– *(101955) Bennu*: Bennu is classified as a B-type asteroid in the visible wavelength range, according to Clark et al. (2011) and Hergenrother et al. (2013). Even if the fraction of B-type asteroids in the Erigone family is small, as is the probability of Bennu coming from the Erigone family (Bottke et al. 2015), the spectral comparison between the spectrum of Bennu and the mean spectrum of the B-type asteroids is compatible with a possible origin in the Erigone family.
– *(162173) Ryugu*: Vilas (2008) reported an aqueous alteration band around 0.7 μm in one of the three visible spectra obtained for Ryugu (July 2007, see their Fig. 4). Following the same approach we used for our aqueous alteration study, the depth of the band we computed in the July 2007 spectrum from Vilas (2008), 11.7±1.3%, is far from the medium depth of the aqueous altered asteroids in Fornasier et al. (2014) (2.8 ± 1.2%) and also in this work (2.9 ± 1.5%). However, from the spectral comparison, the possibility of Ryugu originating in the Erigone family should not be discarded. Ryugu is a C-type asteroid, and the most abundant spectral classes in the Erigone family are C-type asteroids and subclasses (Cb,

Cg, Ch, and Cgh). This would point to a possible origin of Ryugu in the Erigone family, even if all the visible spectra of this asteroid obtained by different authors show no 0.7 μm absorption band.

Since the Polana family, suggested in Bottke et al. (2015) as the most probable source for both NEAs, does not show signs of aqueous altered asteroids (Walsh et al. 2013; Dykhuis & Greenberg 2015; de León et al. 2016), the Erigone family cannot be discarded as a possible source for the two NEAs. More observations of (101955) Bennu and (162173) Ryugu need to be made to check whether the 3 μm absorption feature is present or not, definitely indicating evidence of aqueous alteration, and confirming or ruling out the chances for Erigone being the source of these objects.

5. Conclusions

We studied a total of 103 visible spectra of asteroids in the Erigone primitive family. We observed 101 of these asteroids with the 10.4 m Gran Telescopio Canarias. These objects have never been observed before with spectroscopy. We added the visible spectra of (163) Erigone and (571) Dulcinea from the SMASS database for completeness.

We showed that the slope distribution and the taxonomic classification of the asteroids agree with the assumption of a primitive family. Most of the observed objects are C-types, highly consistent with the classification of (163) Erigone, supporting its status as the parent body of the family. In terms of taxonomical distribution, 42% of the asteroids in our survey are classified as C-type objects, 28% as X-types, 11% as B-types, 7% as T-types, and 13% of the objects as non-primitive types, most likely interlopers (S-types and subclasses, and L-types).

In addition, the study of aqueous alteration performed on the group of primitive objects shows a high number of hydrated asteroids. The C-type class shows the largest number of hydrated asteroids, namely ~86%. The other primitive classes, also showing the hydration band, present a much smaller fraction: B-type objects, ~36%, X-type objects, ~28%, and T-type, ~14%. This distribution of the hydration as a function of the taxonomical class agrees with the one in Fornasier et al. (2014) for asteroids in the main belt.

Based on the spectral comparison alone and as for the Polana family that was studied in de León et al. (2016), we cannot discard the possibility of Erigone being the source family for the NEAs (101955) Bennu and (162173) Ryugu. The spectral classes present in the family are compatible with the taxonomic classification of the two asteroids. Future research should include further spectroscopic study, both in the visible and near-infrared regions, of the other primitive families in the inner belt, such as Sulamitis and Clarissa, to completely rule them out as the possible sources of asteroids (101955) Bennu and (162173) Ryugu.

Acknowledgements. D.M. gratefully acknowledges the Spanish Ministry of Economy and Competitiveness (MINECO) for the financial support received in the form of a Severo-Ochoa Ph.D. fellowship, within the Severo-Ochoa International Ph.D. Program. D.M., J.d.L., J.L., and V.L. acknowledge support from the project AYA2012-39115-C03-03 and ESP2013-47816-C4-2-P (MINECO). J.d.L. acknowledges support from the Insituto de Astrofísica de Canarias. H.C. acknowledges support from NASA's Near-Earth Object Observations program and from the Center for Lunar and Asteroid Surface Science funded by NASA's SSERVI program at the University of Central Florida. The authors gratefully acknowledge the referee, Sonia Fornasier, for her comments and suggestions. The results obtained in this paper are based on observations made with the Gran Telescopio Canarias (GTC), installed in the Spanish Observatorio del Roque de los Muchachos of the Instituto de Astrofísica de Canarias, in the island of La Palma.

References

Barucci, M. A., Doressoundiram, A., Fulchignoni, M., et al. 1998, Icarus, 132, 388
Bevington, P. R., & Robinson, D. K. 1992, Data reduction and error analysis for the physical sciences (New-York, USA: McGraw-Hill Companies)
Binzel, R. P., & Xu, S. 1993, Science, 260, 186
Binzel, R. P., Harris, A. W., Bus, S. J., & Burbine, T. H. 2001, Icarus, 151, 139
Binzel, R. P., DeMeo, F. E., Burt, B. J., et al. 2015, Icarus, 256, 22
Bottke, W. F., Morbidelli, A., Jedicke, R., et al. 2002, Icarus, 156, 399
Bottke, W. F., Vokrouhlický, D., Walsh, K. J., et al. 2015, Icarus, 247, 191
Bus, S. J., & Binzel, R. P. 2002, Icarus, 158, 146
Campins, H., Morbidelli, A., Tsiganis, K., et al. 2010, ApJ, 721, L53
Campins, H., de León, J., Morbidelli, A., et al. 2013, AJ, 146, 26
Carvano, J. M., Mothé-Diniz, T., & Lazzaro, D. 2003, Icarus, 161, 356
Cepa, J. 2010, in Highlights of Spanish Astrophysics V, eds. J. M. Diego, L. J. Goicoechea, J. I. González-Serrano, & J. Gorgas (Springer), 15
Cepa, J., Aguiar, M., Escalera, V. G., et al. 2000, in Optical and IR Telescope Instrumentation and Detectors, eds. M. Iye, & A. F. Moorwood, SPIE Conf. Ser., 4008, 623
Clark, B. E., Ziffer, J., Nesvorny, D., et al. 2010, J. Geophys. Res. (Planets), 115, 6005
Clark, B. E., Binzel, R. P., Howell, E. S., et al. 2011, Icarus, 216, 462
de León, J., Pinilla-Alonso, N., Campins, H., Licandro, J., & Marzo, G. A. 2012, Icarus, 218, 196
de León, J., Pinilla-Alonso, N., Delbo, M., et al. 2016, Icarus, 266, 57
DeMeo, F. E., & Carry, B. 2013, Icarus, 226, 723
DeMeo, F. E., Binzel, R. P., Slivan, S. M., & Bus, S. J. 2009, Icarus, 202, 160
Dykhuis, M. J., & Greenberg, R. 2015, Icarus, 252, 199
Fornasier, S., Lantz, C., Barucci, M. A., & Lazzarin, M. 2014, Icarus, 233, 163
Fornasier, S., Lazzarin, M., Barbieri, C., & Barucci, M. A. 1999, A&AS, 135, 65
Hergenrother, C. W., Nolan, M. C., Binzel, R. P., et al. 2013, Icarus, 226, 663
Hirayama, K. 1918, AJ, 31, 185
Howell, E. S., Rivkin, A. S., Vilas, F., et al. 2011, in EPSC-DPS Joint Meeting 2011, 637
Landolt, A. U. 1992, AJ, 104, 340
Lauretta, D. S., Drake, M. J., Benzel, R. P., et al. 2010, Meteorit. Planet. Sci. Suppl., 73, 5153
Lazzaro, D., Barucci, M. A., Perna, D., et al. 2013, A&A, 549, L2
Luu, J. X., & Jewitt, D. C. 1990, AJ, 99, 1985
Masiero, J. R., Mainzer, A. K., Grav, T., et al. 2011, ApJ, 741, 68
Matsuoka, M., Nakamura, T., Kimura, Y., et al. 2015, Icarus, 254, 135
Milani, A., Cellino, A., Knežević, Z., et al. 2014, Icarus, 239, 46
Moskovitz, N. A., Abe, S., Pan, K.-S., et al. 2013, Icarus, 224, 24
Nesvorny, D. 2012, NASA Planetary Data System, 189
Pinilla-Alonso, N., de León, J., Walsh, K. J., et al. 2016, Icarus, submitted
Popescu, M., Birlan, M., & Nedelcu, D. A. 2012, A&A, 544, A130
Rivkin, A. S. 2012, Icarus, 221, 744
Sugita, S., Kuroda, D., Kameda, S., et al. 2013, in Lunar and Planetary Inst. Technical Report, 44, 2591
Tsuda, Y., Yoshikawa, M., Abe, M., Minamino, H., & Nakazawa, S. 2013, Acta Astron., 91, 356
Vilas, F. 1994, Icarus, 111, 456
Vilas, F. 2008, AJ, 135, 1101
Vilas, F., & Gaffey, M. J. 1989, Science, 246, 790
Vokrouhlický, D., Brož, M., Bottke, W. F., Nesvorný, D., & Morbidelli, A. 2006, Icarus, 182, 118
Walsh, K. J., Delbó, M., Bottke, W. F., Vokrouhlický, D., & Lauretta, D. S. 2013, Icarus, 225, 283
Zappala, V., & Cellino, A. 1994, in Asteroids, Comets, Meteors 1993, eds. A. Milani, M. di Martino, & A. Cellino, IAU Symp., 160, 395
Zappala, V., Cellino, A., Farinella, P., & Knezevic, Z. 1990, AJ, 100, 2030

A&A 586, A129 (2016)

Appendix A: Primitive spectra

We present here the visible spectra of the primitive asteroids (a total of 90). The spectra are normalized to unity at 0.55 μm and binned (see Sect. 2.2). Visible spectrum of asteroid (163) Erigone has been taken from the SMASS-II survey.

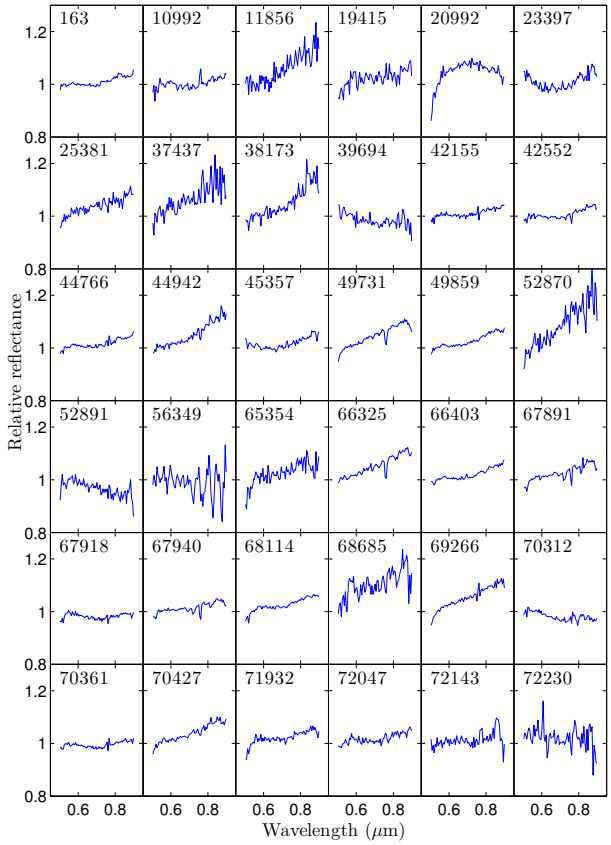

Fig. A.1. Visible spectra of the primitive asteroids. Spectra are normalized to unity at 0.55 μm.

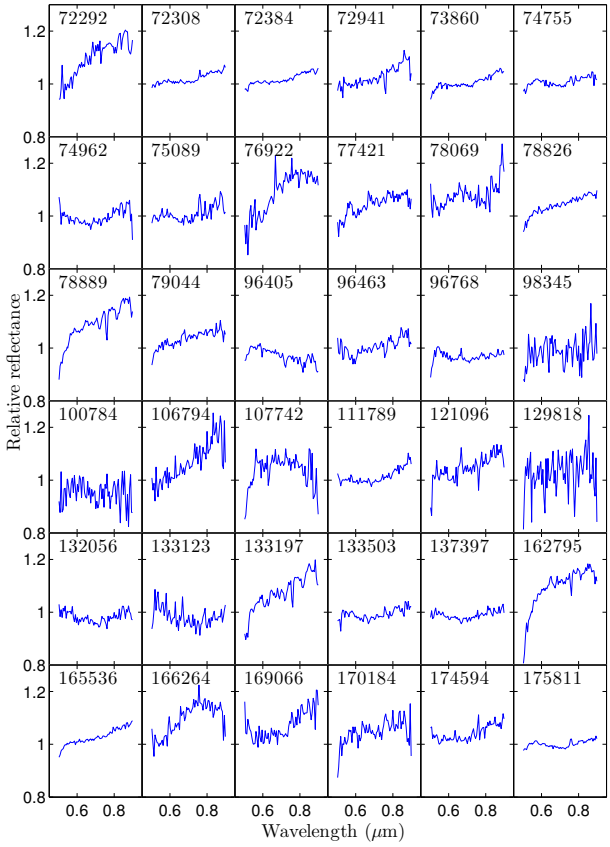

Fig. A.1. continued.

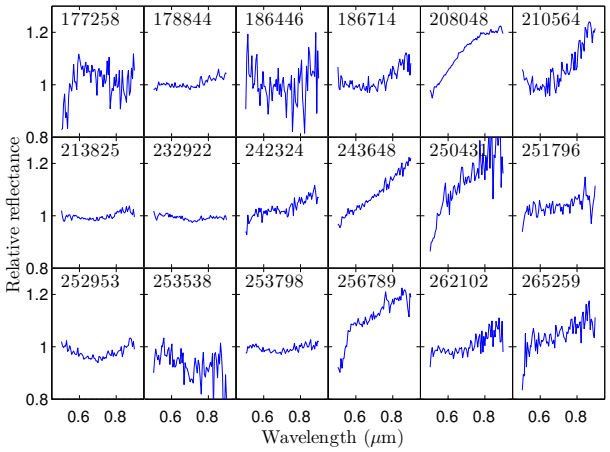

Fig. A.1. continued.

Appendix B: Non-primitive spectra

We present here the visible spectra of the non-primitive asteroids (a total of 13). The spectra are normalized to unity at 0.55 μm and binned (see Sect. 2.2). Visible spectrum of asteroid (571) Dulcinea has been taken from the SMASS-II survey.

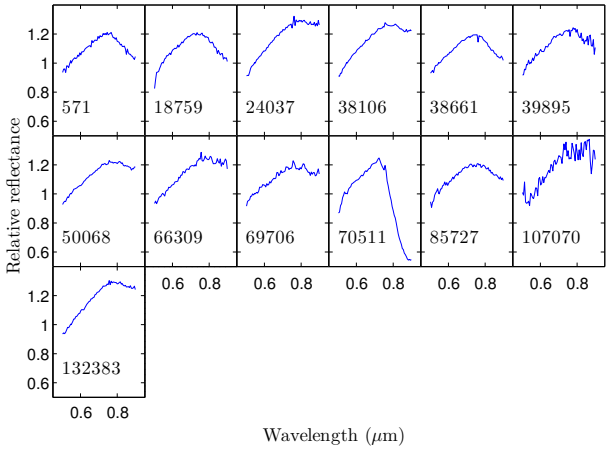

Fig. B.1. Visible spectra of the non-primitive asteroids. Spectra are normalized to unity at 0.55 μm.

Appendix C: Additional tables

Table C.1. Observational circumstances of the asteroids presented in this paper.

Object	Date	UT start	Airmass	Exposure time (s)	SAs	Seeing (″)
10992	2014-08-16	05:46	1.117	3 × 200	5	0.9
11856	2015-01-12	01:10	1.482	3 × 250	2	2.0
18759	2014-12-17	22:35	1.149	3 × 250	1	2.0
19415	2014-09-18	22:23	1.310	3 × 300	4, 6	1.0
20992	2014-12-17	03:13	1.248	3 × 250	2	1.9
23397	2015-01-14	03:51	1.292	3 × 300	1, 3	1.5
24037	2014-12-18	01:27	1.305	2 × 200	1	2.7
25381	2014-12-18	00:22	1.352	3 × 500	1	2.0
37437	2014-12-17	22:04	1.335	3 × 500	1	2.5
38106	2014-10-14	03:43	1.033	3 × 400	1, 2	1.0
38173	2014-12-15	23:46	1.554	3 × 300	1, 2	2.0
38661	2014-09-13	03:04	1.257	3 × 200	1, 6	0.9
39694	2014-09-19	00:18	1.198	3 × 400	4, 6	0.9
39895	2014-09-15	03:38	1.507	3 × 300	1, 6	0.8
42155	2014-09-13	03:36	1.095	3 × 200	1, 6	0.8
42552	2014-09-15	02:50	1.513	3 × 250	1, 6	0.9
44766	2014-12-17	03:58	1.039	3 × 200	2	1.3
44942	2015-01-14	03:29	1.496	3 × 200	1, 3	1.5
45357	2015-01-14	04:22	1.416	3 × 300	1, 3	1.5
49731	2015-01-14	04:46	1.920	3 × 200	1, 3	1.9
49859	2015-05-04	23:37	1.300	3 × 180	3, 7	1.5
50068	2015-05-05	00:10	1.131	3 × 180	3, 7	1.5
52870	2015-01-19	05:57	1.124	3 × 500	3	2.0
52891	2015-01-15	03:53	1.197	3 × 500	3	1.2
56349	2015-01-15	04:29	1.163	3 × 500	3	1.1
65354	2014-12-13	01:05	1.048	3 × 500	2	1.5
66309	2014-10-14	02:34	1.456	3 × 250	1, 2	1.4
66325	2014-10-13	04:20	1.847	3 × 300	1, 2	1.5
66403	2014-09-14	01:35	1.110	3 × 200	1, 6	0.9
67891	2014-09-15	02:09	1.684	3 × 200	1, 6	1.0
67918	2014-09-13	02:39	1.214	3 × 200	1, 6	0.9
67940	2014-09-15	03:14	1.709	3 × 200	1, 6	0.9
68114	2014-09-17	01:22	1.142	3 × 250	6	1.0
68685	2014-10-12	00:30	1.406	4 × 250	6	0.9
69266	2014-12-18	01:52	1.218	3 × 250	1	3.0
69706	2014-09-15	04:56	1.023	3 × 500	1, 6	0.8
70312	2014-09-18	03:01	1.088	3 × 300	1, 4	1.3
70361	2014-12-17	03:38	1.180	3 × 200	2	1.7
70427	2015-01-14	05:06	1.606	3 × 250	1, 3	1.7
70511	2014-09-15	04:20	1.010	3 × 300	1, 6	0.7
71932	2014-10-13	02:22	1.176	3 × 200	1, 2	1.2
72047	2014-11-25	22:13	1.027	3 × 350	1	1.3
72143	2014-09-19	23:39	1.414	3 × 250	1, 6	1.3
72230	2014-09-19	01:40	1.308	2 × 300	4, 6	0.9
72292	2014-12-18	00:57	1.276	3 × 450	1	2.0
72308	2014-08-16	04:04	1.304	3 × 250	5	0.7
72384	2014-11-25	21:49	1.201	3 × 250	1	1.4
72941	2014-10-13	03:57	1.997	3 × 300	1, 2	1.6
73860	2014-09-14	03:27	1.177	3 × 250	1, 6	0.9
74755	2014-11-25	22:53	1.017	3 × 300	1	1.2
74962	2014-12-02	04:21	1.136	3 × 500	2	1.4
75089	2015-01-19	04:48	1.096	3 × 350	3	2.5
76922	2014-10-08	00:02	1.292	6 × 250	1, 6	0.7
77421	2014-10-10	05:44	1.040	2 × 500	1, 2	0.8
78069	2014-12-02	05:29	1.377	3 × 500	2	1.7
78826	2014-09-13	04:53	1.114	3 × 200	1, 6	0.8
78889	2014-10-12	02:05	2.199	4 × 150	6	1.4
79044	2014-10-10	05:05	1.078	3 × 400	1, 2	0.7

Notes. Check Table 1 for the ID number of each solar analog star.

A&A 586, A129 (2016)

Table C.1. continued.

Object	Date	UT start	Airmass	Exposure time (s)	SAs	Seeing (″)
85727	2015-05-04	23:47	1.176	3 × 250	3, 7	0.9
96405	2014-09-17	22:15	1.294	5 × 400	1, 4	1.3
96463	2014-10-13	02:48	1.862	3 × 400	1, 2	1.2
96768	2014-10-07	23:23	1.315	3 × 300	1, 6	0.8
98345	2014-09-17	21:39	1.392	3 × 400	1, 4	1.3
100784	2014-09-18	04:59	1.049	5 × 500	1, 4	2.0
106794	2014-12-16	00:11	1.602	3 × 300	1, 2	3.0
107070	2014-10-13	03:29	1.873	3 × 400	1, 2	1.3
107742	2014-12-17	23:13	1.214	3 × 500	1	2.4
111789	2014-09-20	01:19	1.283	3 × 400	1, 6	1.1
121096	2014-10-07	22:20	1.458	3 × 300	1, 6	0.7
129818	2014-10-10	04:31	1.098	3 × 500	1, 2	0.7
132056	2014-10-12	02:33	1.306	3 × 250	6	1.1
132383	2014-10-14	04:39	1.026	3 × 400	1, 2	1.0
133123	2014-10-07	22:51	1.329	3 × 400	1, 6	0.7
133197	2014-10-12	01:37	1.954	3 × 250	6	1.0
133503	2014-10-14	03:06	1.047	3 × 500	1, 2	1.4
137397	2014-10-14	04:10	1.057	3 × 300	1, 2	1.1
162795	2014-10-12	01:06	1.613	3 × 300	6	1.0
165536	2014-12-18	02:17	1.235	3 × 250	1	0.7
166264	2014-09-18	23:28	1.178	3 × 400	4, 6	1.0
169066	2014-12-16	00:42	1.301	3 × 300	1, 2	1.8
170184	2014-11-25	23:23	1.190	3 × 400	1	1.7
174594	2014-12-15	22:55	1.049	3 × 250	1, 2	1.6
175811	2014-12-14	02:57	1.181	3 × 300	2	2.0
177258	2014-12-07	06:31	1.197	3 × 300	2	0.9
178844	2014-12-16	04:41	1.210	3 × 350	1, 2	1.6
186446	2015-01-21	07:01	1.163	2 × 600	3	1.8
186714	2014-12-14	05:32	1.574	2 × 350	2	2.3
208048	2015-01-20	00:28	1.224	3 × 600	1, 2	2.0
210564	2015-01-19	23:35	1.515	3 × 500	1,2	2.5
213825	2014-12-02	03:35	1.158	3 × 300	2	1.4
232922	2014-09-18	23:01	1.177	3 × 200	4, 6	1.0
242324	2015-01-16	23:07	1.212	3 × 500	2	2.0
243648	2014-12-16	04:06	1.193	3 × 500	1, 2	1.6
250431	2015-01-19	22:48	1.259	3 × 600	1, 2	3.0
251796	2015-01-26	04:20	1.041	3 × 600	3	1.5
252953	2015-01-26	03:16	1.012	3 × 450	3	1.5
253538	2015-01-19	22:02	1.304	3 × 500	1,2	2.5
253798	2015-01-26	03:47	1.031	3 × 400	3	1.8
256789	2014-12-14	03:27	1.127	3 × 400	2	2.0
262102	2015-01-26	05:37	1.111	3 × 600	3	1.6
265259	2015-01-26	04:59	1.109	3 × 600	3	1.5

Table C.2. Physical parameters of the targets.

Object	a (AU)	e	i (°)	H_V	D (km)	err$_D$	p_V	err$_{pV}$	Class
163	2.367	0.21	4.801	9.5	81.58	3.06	0.033	0.004	Ch
571	2.41	0.213	5.222	11.6	11.70	0.09	0.298	0.049	S
10992	2.363	0.205	5.022	15.1	5.48	0.28	0.062	0.014	Cgh
11856	2.384	0.201	4.735	15.2	4.20	0.44	0.093	0.029	X
18759	2.338	0.205	4.641	14.6	2.90	0.13	0.303	0.048	Sr
19415	2.382	0.209	5.055	15.0	5.76	0.18	0.058	0.005	C
20992	2.337	0.199	5.156	15.3	4.02	0.38	0.074	0.035	Xk
23397	2.357	0.218	5.692	15.1	7.75	3.34	0.027	0.021	Ch
24037	2.378	0.198	5.568	14.7	3.87	0.58	0.129	0.031	L
25381	2.395	0.202	4.751	16.4	4.33	0.17	0.028	0.005	X
37437	2.349	0.215	5.06	15.4	5.30	0.78	0.043	0.026	Xc
38106	2.331	0.213	4.781	15.4	–	–	–	–	L
38173	2.355	0.212	4.736	15.7	3.56	0.24	0.080	0.016	X
38661	2.309	0.203	4.834	15.5	–	–	–	–	Sr
39694	2.358	0.208	5.369	16.0	3.97	1.20	0.041	0.035	B
39895	2.393	0.198	5.526	15.4	–	–	–	–	S
42155	2.38	0.203	5.225	15.1	5.93	0.93	0.049	0.018	Cgh
42552	2.356	0.208	4.938	15.2	4.90	0.33	0.051	0.014	Cgh
44766	2.363	0.21	5.207	14.9	6.46	0.76	0.041	0.022	Cgh
44942	2.383	0.204	5.215	15.2	4.83	0.67	0.063	0.051	X
45357	2.374	0.215	5.211	15.5	3.96	0.06	0.078	0.006	Cgh
49731	2.379	0.202	5.25	15.1	5.22	1.10	0.065	0.066	X
49859	2.361	0.212	5.003	14.4	7.45	2.56	0.055	0.069	Cgh
50068	2.347	0.206	5.035	14.9	–	–	–	–	L
52870	2.359	0.205	4.938	15.2	5.53	0.05	0.053	0.009	T
52891	2.354	0.201	4.86	15.4	4.67	0.40	0.056	0.009	B
56349	2.352	0.209	5.314	15.2	–	–	–	–	B
65354	2.351	0.208	4.799	16.0	4.13	1.59	0.034	0.020	Xc
66309	2.353	0.208	4.873	15.3	3.45	0.46	0.094	0.023	L
66325	2.352	0.205	5.125	15.4	5.63	1.87	0.042	0.088	Xc
66403	2.387	0.202	5.004	15.4	–	–	–	–	Ch
67891	2.373	0.205	5.273	15.1	5.10	0.18	0.062	0.010	Ch
67918	2.376	0.203	4.942	15.1	4.76	1.27	0.076	0.069	Ch
67940	2.372	0.205	4.611	15.2	5.60	0.26	0.051	0.009	Ch
68114	2.36	0.209	4.635	15.5	5.96	1.15	0.031	0.016	Cgh
68685	2.358	0.218	5.458	15.5	4.66	0.13	0.056	0.011	Xc
69266	2.381	0.212	5.036	15.2	5.58	1.10	0.049	0.016	X
69706	2.343	0.2	4.808	15.3	-	-	-	-	S
70312	2.391	0.214	4.737	15.4	4.88	0.22	0.044	0.017	B
70361	2.357	0.206	4.453	15.0	6.49	1.22	0.043	0.018	Ch
70427	2.37	0.208	5.087	15.1	5.56	0.01	0.051	0.001	X
70511	2.402	0.203	5.165	15.2	–	–	–	–	V
71932	2.351	0.209	4.968	16.0	4.39	0.22	0.044	0.005	Cgh
72047	2.352	0.204	4.807	15.7	4.37	1.23	0.031	0.012	Ch
72143	2.354	0.209	5.232	15.8	4.71	0.12	0.046	0.006	Cb
72230	2.392	0.205	4.753	15.5	4.72	0.26	0.042	0.008	B
72292	2.358	0.212	5.534	15.9	4.57	0.86	0.025	0.014	Xk
72308	2.383	0.209	4.736	15.6	5.07	1.20	0.055	0.023	Ch
72384	2.381	0.209	5.281	15.5	3.95	0.64	0.088	0.049	Ch
72941	2.352	0.206	5.209	15.6	4.08	0.43	0.063	0.032	X
73860	2.378	0.209	5.093	16.1	4.32	1.09	0.042	0.026	Cgh
74755	2.39	0.201	5.303	15.7	3.92	0.03	0.072	0.006	Cgh
74962	2.359	0.213	5.034	15.9	4.36	0.32	0.041	0.015	Ch
75089	2.361	0.212	5.07	15.6	4.62	0.13	0.048	0.006	Cgh
76922	2.388	0.202	5.182	15.4	–	–	–	–	Xk
77421	2.374	0.206	4.815	15.6	4.52	0.09	0.041	0.004	Xk
78069	2.388	0.201	4.788	15.8	3.96	0.09	0.059	0.010	Xk
78826	2.356	0.217	5.52	15.7	4.93	0.97	0.042	0.032	Xc
78889	2.388	0.218	5.055	15.8	3.76	0.51	0.072	0.022	T
79044	2.386	0.209	4.739	16.0	3.77	0.52	0.063	0.020	X
85727	2.336	0.211	5.628	15.7	–	–	–	–	S
96405	2.342	0.214	5.347	15.4	5.11	0.35	0.056	0.018	B
96463	2.386	0.211	5.173	15.6	5.14	0.97	0.038	0.016	Cb
96768	2.377	0.206	4.686	15.5	4.57	0.85	0.059	0.025	Cgh
98345	2.361	0.211	5.137	15.4	4.61	0.25	0.063	0.015	Cg
100784	2.367	0.207	4.802	15.6	4.64	0.22	0.050	0.011	B
106794	2.339	0.215	5.317	15.8	3.82	0.61	0.070	0.078	T

A&A 586, A129 (2016)

Table C.2. continued.

Object	a (AU)	e	i (°)	H_V	D (km)	err$_D$	p_V	err$_{pV}$	Class
107070	2.406	0.177	5.419	15.9	–	–	–	–	L
107742	2.399	0.199	5.48	16.1	3.39	0.64	0.067	0.022	B
111789	2.383	0.203	5.208	15.7	4.01	0.09	0.069	0.015	Ch
121096	2.346	0.211	5.338	15.8	4.10	0.15	0.036	0.005	X
129818	2.347	0.208	4.854	16.0	3.66	0.64	0.069	0.027	Cb
132056	2.35	0.205	5.17	15.9	3.96	0.47	0.053	0.015	Ch
132383	2.357	0.21	5.149	15.6	1.77	0.42	0.356	0.156	L
133123	2.361	0.214	5.261	16.2	3.24	0.04	0.062	0.009	B
133197	2.386	0.209	5.078	15.8	3.96	0.09	0.065	0.015	T
133503	2.349	0.211	5.042	16.3	3.02	0.02	0.058	0.008	Cgh
137397	2.393	0.202	4.972	16.3	2.83	0.43	0.067	0.027	Ch
162795	2.361	0.212	5.388	16.2	3.83	0.19	0.048	0.014	T
165536	2.354	0.21	5.064	16.0	3.58	0.65	0.057	0.030	Cgh
166264	2.381	0.177	5.199	15.9	–	–	–	–	Xk
169066	2.386	0.212	5.316	15.9	4.93	0.25	0.038	0.005	X
170184	2.347	0.208	5.234	16.3	3.69	0.85	0.039	0.014	Xk
174594	2.353	0.215	5.427	16.3	2.84	0.65	0.096	0.040	Ch
175811	2.379	0.214	4.802	15.7	3.91	0.57	0.057	0.027	Cgh
177258	2.325	0.214	5.162	16.9	2.49	0.57	0.050	0.028	B
178844	2.373	0.206	5.123	16.2	3.61	0.43	0.045	0.008	Cgh
186446	2.378	0.199	5.117	16.0	–	–	–	–	Ch
186714	2.404	0.215	5.207	16.9	2.33	0.53	0.062	0.028	Cgh
208048	2.389	0.213	4.844	16.5	3.26	0.38	0.052	0.013	T
210564	2.414	0.21	5.33	16.6	3.04	0.35	0.046	0.018	X
213825	2.356	0.207	4.882	16.1	3.40	0.60	0.061	0.021	Cgh
232922	2.348	0.215	5.17	16.0	3.78	0.15	0.054	0.009	Ch
242324	2.411	0.205	4.952	17.0	2.49	0.70	0.059	0.048	Ch
243648	2.387	0.193	5.093	16.9	2.56	0.05	0.052	0.008	X
250431	2.398	0.211	5.337	16.7	3.29	0.59	0.037	0.013	T
251796	2.341	0.204	4.826	16.8	3.08	0.91	0.035	0.022	X
252953	2.401	0.202	4.749	16.3	3.58	1.04	0.046	0.040	Ch
253538	2.393	0.217	5.526	16.4	3.17	0.91	0.048	0.044	B
253798	2.332	0.201	4.732	16.8	2.60	0.43	0.055	0.020	Ch
256789	2.373	0.207	4.857	16.8	2.54	0.32	0.052	0.010	X
262102	2.355	0.207	4.891	17.2	3.01	0.79	0.026	0.025	Ch
265259	2.404	0.21	4.981	16.9	3.18	0.58	0.036	0.015	X

Table C.3. Summary of the obtained results for the primitive asteroids in our sample.

Object	Class	Slope (%/1000 Å)	Band	λ_{cent}(Å)	Depth (%)
163	Ch	1.34 ± 0.61	YES	6899 ± 26	1.52 ± 0.07
10992	Cgh	0.95 ± 0.63	YES	7074 ± 37	1.80 ± 0.14
11856	X	4.94 ± 0.71	NO	–	–
19415	C	–0.56 ± 0.66	NO	–	–
20992	Xk	–0.17 ± 0.64	NO	–	–
23397	Ch	1.95 ± 0.65	YES	6957 ± 78	4.43 ± 0.22
25381	X	2.16 ± 0.63	NO	–	–
37437	Xc	3.65 ± 0.76	NO	–	–
38173	X	4.90 ± 0.70	YES	7149 ± 60	4.32 ± 0.28
39694	B	–0.77 ± 0.65	YES	6887 ± 98	2.23 ± 0.30
42155	Cgh	1.07 ± 0.61	YES	6961 ± 35	1.34 ± 0.08
42552	Cgh	1.33 ± 0.62	YES	7107 ± 33	2.26 ± 0.10
44766	Cgh	1.29 ± 0.61	YES	7054 ± 33	1.48 ± 0.08
44942	X	4.10 ± 0.63	YES	7089 ± 81	2.69 ± 0.16
45357	Cgh	1.75 ± 0.62	YES	6913 ± 68	2.76 ± 0.11
49731	X	2.85 ± 0.62	NO	–	–
49859	Cgh	2.15 ± 0.61	YES	6936 ± 32	1.83 ± 0.08
52870	T	5.99 ± 0.77	NO	–	–
52891	B	–2.13 ± 0.64	NO	–	–
56349	B	–0.85 ± 0.87	NO	–	–
65354	Xc	1.78 ± 0.66	NO	–	–
66325	Xc	3.13 ± 0.62	NO	–	–
66403	Ch	1.87 ± 0.61	YES	7023 ± 30	2.00 ± 0.07
67891	Ch	1.83 ± 0.63	YES	7348 ± 75	1.75 ± 0.20
67918	Ch	0.05 ± 0.61	YES	7052 ± 32	2.20 ± 0.08
67940	Ch	1.11 ± 0.62	YES	7149 ± 53	1.25 ± 0.11
68114	Cgh	1.63 ± 0.61	YES	7153 ± 33	1.29 ± 0.07
68685	Xc	2.18 ± 0.74	NO	–	–
69266	X	3.07 ± 0.61	NO	–	–
70312	B	–0.74 ± 0.62	YES	6996 ± 35	2.00 ± 0.10
70361	Ch	0.63 ± 0.61	YES	7049 ± 32	1.96 ± 0.08
70427	X	2.65 ± 0.61	YES	6890 ± 68	1.39 ± 0.14
71932	Cgh	1.18 ± 0.62	YES	7199 ± 48	1.74 ± 0.12
72047	Ch	1.16 ± 0.62	YES	7125 ± 52	1.79 ± 0.16
72143	Cb	0.96 ± 0.68	NO	–	–
72230	B	–1.20 ± 0.78	NO	–	–
72292	Xk	4.63 ± 0.74	NO	–	–
72308	Ch	1.34 ± 0.61	YES	7050 ± 32	1.76 ± 0.06
72384	Ch	1.63 ± 0.61	YES	7018 ± 33	1.64 ± 0.07
72941	X	2.92 ± 0.66	YES	7380 ± 102	3.24 ± 0.20
73860	Cgh	1.81 ± 0.61	YES	7230 ± 65	2.49 ± 0.12
74755	Cgh	0.71 ± 0.62	YES	7118 ± 50	2.34 ± 0.16
74962	Ch	1.50 ± 0.67	YES	6922 ± 47	4.02 ± 0.23
75089	Cgh	1.65 ± 0.68	YES	7200 ± 108	4.15 ± 0.37
76922	Xk	5.06 ± 0.78	NO	–	–
77421	Xk	1.78 ± 0.65	NO	–	–
78069	Xk	2.51 ± 0.76	NO	–	–
78826	Xc	2.22 ± 0.61	NO	-	–
78889	T	3.62 ± 0.66	NO	–	–
79044	X	1.76 ± 0.63	NO	–	–
96405	B	–2.02 ± 0.63	NO	–	–
96463	Cb	2.49 ± 0.65	NO	–	–
96768	Cgh	0.23 ± 0.62	YES	6642 ± 41	3.41 ± 0.19
98345	Cg	–0.72 ± 0.86	NO	–	–
100784	B	–2.01 ± 0.83	NO	–	–
106794	T	5.55 ± 0.80	YES	7364 ± 202	3.52 ± 0.45
107742	B	–1.74 ± 0.80	NO	–	–
111789	Ch	2.24 ± 0.64	YES	7073 ± 32	3.32 ± 0.11
121096	X	2.76 ± 0.69	YES	6853 ± 250	2.23 ± 0.33
129818	Cb	1.45 ± 1.08	NO	–	–
132056	Ch	0.48 ± 0.65	YES	7108 ± 63	4.20 ± 0.24
133123	B	–0.58 ± 0.71	YES	7282 ± 137	4.28 ± 0.36
133197	T	3.92 ± 0.67	NO	–	–
133503	Cgh	1.15 ± 0.63	YES	6898 ± 76	2.83 ± 0.27
137397	Ch	0.92 ± 0.62	YES	6740 ± 46	2.67 ± 0.14
162795	T	2.93 ± 0.65	NO	–	–
165536	Cgh	2.38 ± 0.61	YES	7102 ± 53	1.44 ± 0.10

A&A 586, A129 (2016)

Table C.3. continued.

Object	Class	Slope (%/1000 Å)	Band	λ_{cent} (Å)	Depth (%)
166264	Xk	2.86 ± 0.78	NO	–	–
169066	X	4.50 ± 0.70	YES	6974 ± 59	3.08 ± 0.32
170184	Xk	1.11 ± 0.72	NO	–	–
174594	Ch	2.41 ± 0.64	YES	7051 ± 46	2.09 ± 0.16
175811	Cgh	0.61 ± 0.61	YES	7093 ± 31	2.36 ± 0.07
177258	B	–1.41 ± 0.81	NO	–	–
178844	Cgh	1.29 ± 0.62	YES	7058 ± 42	2.52 ± 0.13
186446	Ch	1.10 ± 1.08	YES	7081 ± 26	6.06 ± 0.74
186714	Cgh	3.25 ± 0.68	YES	7145 ± 66	5.50 ± 0.29
208048	T	5.74 ± 0.64	NO	–	–
210564	X	7.22 ± 0.78	YES	7009 ± 24	9.14 ± 0.58
213825	Cgh	0.93 ± 0.61	YES	7019 ± 48	2.42 ± 0.13
232922	Ch	–0.23 ± 0.61	YES	7109 ± 28	1.50 ± 0.06
242324	Ch	2.30 ± 0.64	YES	7420 ± 87	2.81 ± 0.29
243648	X	6.20 ± 0.62	YES	6957 ± 93	1.85 ± 0.17
250431	T	6.59 ± 0.97	NO	–	–
251796	X	1.43 ± 0.68	NO	–	–
252953	Ch	1.17 ± 0.64	YES	7127 ± 87	4.60 ± 0.21
253538	B	–2.79 ± 0.92	YES	7199 ± 118	6.49 ± 0.78
253798	Ch	0.65 ± 0.62	YES	6755 ± 42	2.42 ± 0.12
256789	X	4.01 ± 0.65	NO	–	–
262102	Ch	2.85 ± 0.70	YES	6816 ± 134	4.21 ± 0.28
265259	X	2.80 ± 0.71	NO	–	–

Chapter 5

Visible spectroscopy of the Sulamitis and Clarissa primitive families: a possible link to Erigone and Polana

For this second paper, we carried out observations with the 10.4 m Gran Telescopio Canarias of asteroids in the Sulamitis and Clarissa collisional families. These two families, together with the Polana–Eulalia complex and Erigone, complete the group of low-inclination primitive families in the IMB proposed as the possible origins of NEAs Bennu and Ryugu. We obtained spectra of 64 and 33 asteroids in the Sulamitis and Clarissa primitive collisional families, respectively. The results of those observations pointed to a possible connection between these two families and the Polana–Eulalia complex and the Erigone family. We also improved the detection pipeline for the search and analysis of hydration features in visible spectra, developed in the first work of the thesis.

A&A 610, A25 (2018)
DOI: 10.1051/0004-6361/201731407

Astronomy & Astrophysics

Visible spectroscopy of the Sulamitis and Clarissa primitive families: a possible link to Erigone and Polana⋆

David Morate[1,2], Julia de León[1,2], Mário De Prá[3], Javier Licandro[1,2], Antonio Cabrera-Lavers[1,4], Humberto Campins[5], and Noemí Pinilla-Alonso[6]

[1] Instituto de Astrofísica de Canarias (IAC), C/vía Láctea s/n, 38205 La Laguna, Tenerife, Spain
e-mail: damog@iac.es
[2] Departamento de Astrofísica, Universidad de La Laguna, 38205 La Laguna, Tenerife, Spain
[3] Observatório Nacional, Coordenação de Astronomia e Astrofísica, 20921-400 Rio de Janeiro, Brazil
[4] GTC Project Office, 38205 La Laguna, Tenerife, Spain
[5] Physics Department, University of Central Florida, PO Box 162385, Orlando, FL 32816-2385, USA
[6] Florida Space Institute, University of Central Florida, Orlando, FL 32816, USA

Received 20 June 2017 / Accepted 5 October 2017

ABSTRACT

The low-inclination ($i < 8°$) primitive asteroid families in the inner main belt, that is, Polana-Eulalia, Erigone, Sulamitis, and Clarissa, are considered to be the most likely sources of near-Earth asteroids (101955) Bennu and (162173) Ryugu. These two primitive NEAs will be visited by NASA OSIRIS-REx and JAXA Hayabusa 2 missions, respectively, with the aim of collecting samples of material from their surfaces and returning them back to Earth. In this context, the PRIMitive Asteroid Spectroscopic Survey (PRIMASS) was born, with the main aim to characterize the possible origins of these NEAs and constrain their dynamical evolution. As part of the PRIMASS survey we have already studied the Polana and Erigone collisional families in previously published works. The main goal of the work presented here is to compositionally characterize the Sulamitis and Clarissa families using visible spectroscopy. We have observed 97 asteroids (64 from Sulamitis and 33 from Clarissa) with the OSIRIS instrument (0.5–0.9 μm) at the 10.4 m Gran Telescopio Canarias (GTC). We found that about 60% of the sampled asteroids from the Sulamitis family show signs of aqueous alteration on their surfaces. We also found that the majority of the Clarissa members present no signs of hydration. The results obtained here show similarities between Sulamitis-Erigone and Clarissa-Polana collisional families.

Key words. minor planets, asteroids: general – methods: data analysis – techniques: spectroscopic

1. Introduction

Primitive asteroids are characterized by dark surfaces dominated by carbon compounds and are associated with carbonaceous chondrites, the most pristine meteorites in our records. These are usually composed of water-bearing minerals and organics, and so they carry the answer to the unsolved question on how water and life appeared on Earth. These life-forming materials present rather featureless spectra in visible to near-infrarred wavelengths, showing diagnostic absorption features in the 3 μm region. In particular, there is a hydration band centered around 2.7−2.9 μm and observed in infrared photometry and spectroscopy of many primitive asteroids, that is correlated with the 0.7 μm $Fe^{2+} \rightarrow Fe^{+3}$ oxidized iron absorption band observed in their visible spectra (Vilas & Gaffey 1989; Vilas 1994; Howell et al. 2011; Rivkin 2012). Aqueous alteration acts on primitive asteroids (C, B, and low albedo X-types, according to the DeMeo et al. (2009) classification scheme) by producing a low-temperature (<320 K) chemical alteration of the materials due to the presence of liquid water. This water acts as a solvent and generates hydrated materials like phyllosilicates, sulfates, oxides, carbonates, and hydroxides. Thus, the existence of hydrated materials on the surface of asteroids implies that, at some point, liquid water was present on these objects, produced by the melting of water ice by heating processes (Fornasier et al. 2014). Primitive asteroids have suffered minimal geological or thermal evolution, but have experienced an intense collisional evolution that affected their size, shape, and surface composition.

Collisional families are groups of fragments ("members") generated by a disruptive collisional event of a larger parent body. Therefore, members of a family share similar orbital properties. Spectroscopic observations of the Vesta family (Binzel & Xu 1993) provided the first confirmation of the collisional origin of a family and since then the spectroscopic study of collisional families have steadily increased. In addition, having in mind that near-Earth asteroids (NEAs) come principally from the main asteroid belt (Bottke et al. 2002), collisional families are preferred as sources of NEAs as they generate a lot of small chunks when they are formed. Families placed near particular resonances in the main belt can effortlessly drive these chunks into the near-Earth space. Because of this, the inner asteroid belt (the region located between the ν_6 resonance, near 2.15 AU, and the 3:1 mean-motion resonance with Jupiter, at 2.5 AU) is thought to be the primary source of the near Earth asteroid population (Bottke et al. 2002).

Two sample-return missions, NASA OSIRIS-REx (Lauretta et al. 2010) and JAXA Hayabusa2 (Tsuda et al. 2013) have

⋆ The reduced spectra are only available at the CDS via anonymous ftp to cdsarc.u-strasbg.fr (130.79.128.5) or via http://cdsarc.u-strasbg.fr/viz-bin/qcat?J/A+A/610/A25

A&A 610, A25 (2018)

targeted primitive NEAs: (101955) Bennu and (162173) Ryugu, respectively. These asteroids are believed to originate in the inner belt, where five possible sources have been identified: the four primitive collisional families Polana, Erigone, Sulamitis, and Clarissa, and a population of low-albedo and low-inclination background asteroids (Campins et al. 2010, 2013; Gayon-Markt et al. 2012; Bottke et al. 2015). The compositional characterization of the source regions of these two NEAs will enhance the science return of these missions.

With this objective in mind we started in 2010 a spectroscopic survey in the visible and the near-infrared to characterize the primitive collisional families in the inner belt and the low-albedo background population. This is the PRIMitive Asteroid Spectroscopic Survey (PRIMASS). It includes also primitive collisional families and dynamical populations of the outer main belt, as well as other groups of primitive asteroids, like the B-types. So far we have spectroscopically observed more than 400 asteroids.

We have already published some results on the characterization of these inner belt families. Results from visible spectroscopy for the Polana-Eulalia family complex and for the Erigone family can be found in de León et al. (2016) and Morate et al. (2016) respectively, mainly obtained with the 10.4 m Gran Telescopio Canarias (GTC), located at the El Roque de los Muchachos Observatory, in the island of La Palma (Spain). Results from near-infrared spectroscopy for the Polana-Eulalia complex can be found in Pinilla-Alonso et al. (2016). These were obtained using both the Telescopio Nazionale *Galileo* (TNG) and the NASA Infrared Telescope Facility (IRTF). We have also published results on the Hilda and Cybele groups in the outer main belt (De Prá et al. 2017).

To continue with our PRIMASS survey, we have observed and characterized the Sulamitis and Clarissa families by means of visible spectroscopy. These are the smallest families of the low-inclination ($i < 8°$) primitive families in the inner belt. We have carried out our study using visible spectra obtained with the GTC during the semesters 2015A, 2015B, and 2016A (January 2015–August 2016), following similar procedures for the data acquisition, reduction, and compositional analysis as those described in Morate et al. (2016). Details on the observations and on the data reduction are presented in Sect. 2. In Sect. 3 we present the analysis of the data, including taxonomical classification, computation of spectral slopes and analysis of aqueous alteration. In Sect. 4 we discuss the obtained results, and the conclusions are summarized in Sect. 5.

2. Observations and data reduction

The asteroids observed within this study have been selected using the dataset of families from Nesvorny (2015) in the Small Bodies Node of the NASA Planetary Data System. This dataset contains asteroid dynamical family memberships for 122 families calculated from synthetic proper elements, including high-inclination families, computed by David Nesvorný (Nesvorný et al. 2015) using his code based on the Hierarchical Clustering Method (HCM) as described in Zappala et al. (1990) and Zappala & Cellino (1994). The dataset also provides values for the absolute magnitude of the asteroids (H_v), as well as their synthetic proper elements used to compute family membership. According to this dataset, the Sulamitis and Clarissa families have 303 and 179 members, respectively. Table B.2 shows the orbital and physical information on the asteroids studied in this work, including proper semi-major axis (a), eccentricity (e), inclination (i), and absolute magnitude. Whenever available, we included the diameter (D) and geometric albedos (p_V) extracted from the NEOWISE database (Mainzer et al. 2016).

Sulamitis and Clarisa collisional families are classified as primitive ones based on the information regarding visible albedo (and taxonomical classification of a few) of their members. From the 174 members of the Sulamitis family having visible albedo determinations, 170 show values of $p_V < 0.1$. In the case of the Clarissa family, a total of 68 objects have p_V determined, and 67 of them have also $p_V < 0.1$. Selecting just objects with $p_V < 0.1$ would be excessively conservative, leaving us without observable targets at some nights of the semesters (see Sect. 2.1 for more details). Therefore, our only constraint was the apparent visual magnitude of the objects, being in the range $18 < m_V < 21$, observing objects with and without a priori information on their albedo. An exception to this constraint are asteroids (752) Sulamitis and (302) Clarissa, which are the largest (and brightest) members of the families, and their expected parent bodies.

2.1. Observations

A total of 97 low-resolution visible spectra were obtained for the asteroids in the Sulamitis and Clarissa families (64 and 33 objects, respectively), using the Optical System for Imaging and Low Resolution Integrated Spectroscopy (OSIRIS) camera spectrograph (Cepa et al. 2000; Cepa 2010) at the 10.4 m GTC, located at the El Roque de los Muchachos Observatory (ORM) in La Palma, Canary Islands, Spain. See Sect. 2.1 in Morate et al. (2016) for further information about the OSIRIS instrument and specifications.

The instrument configuration and the observational procedure are the same that we used for the observations in Morate et al. (2016), except for the use of a 2.5″-width slit, instead of the 5″-width slit used in the previous work. Observational details are shown in Table B.1, including asteroid number, date of observation, starting time of the first exposition, exposure time, and visible magnitude (m_V) at the moment of the observation. We also include the solar analog stars used to obtain the reflectance spectra.

Observations were done in service mode within GTC programs GTC18-15A, GTC48-15B, and GTC15-16A, on different nights from January 2015 to August 2016. Given the fact that the program is classified as a filler within the GTC schedule, night qualities were rather variable, covering a wide range of different weather conditions. The goal of these filler programs is to obtain high S/N spectra for targets that are relatively bright for a 10 m-class telescope in non-optimal weather conditions. These would include high seeing values (up to 2.0″), full moon, or some cirrus coverage. Because of this, spectra quality might vary from one night to another.

In addition, we obtained three spectra of (752) Sulamitis using the Intermediate Dispersion Spectrograph (IDS) at the 2.5 m *Isaac Newton* Telescope (INT), also located at the ORM in La Palma, as part of program C97 (2015), on July 22, 2015. The IDS instrument was used with a 4096 × 2048 pixels RED+2 CCD detector, having a scale plate of 0.44″/pixel, and a total of 2200 unvignetted pixels. The spectra were obtained using the R150V grism, which produces a dispersion of 4.03 Å/pixel, for a slit of 1.0″, covering the spectral range from 4000–10 000 Å. The R150V grism was used in combination of a 1.5″ slit. The observational procedure was the same as the one we used for the observations with the OSIRIS instrument at the GTC, described above.

Table 1. Right ascension, declination, and visible magnitude for the solar analog stars used to obtain the reflectance spectra of the observed asteroids.

ID	Star	α	δ	V
1	SA 93-101	01:53:18.0	+00:22:25	9.7
2	SA 98-978	06:51:34.0	–00:11:28	10.5
3	SA 102-1081	10:57:04.4	–00:13:10	9.9
4	SA 107-998	15:38:16.4	+00:15:23	10.4
5	SA 110-361	18:42:45.0	+00:08:04	12.4
6	SA 112-1333	20:43:11.8	+00:26:15	10.0
7	SA 115-271	23:42:41.8	+00:45:10	9.7

Notes. The ID number is the same as the one appearing in the last column of Table B.1.

2.2. Data reduction

To reduce the spectroscopic data obtained with the GTC we used a similar procedure as that described in Morate et al. (2016), using our own developed pipeline combining standard IRAF[1] tasks and some Python routines. The process included bias and flat-field correction of the 2D-images, sky background subtraction and 1D-spectra extraction, and wavelength calibration using Xe+Ne+HgAr lamps. We used the same pipeline to reduce the INT spectrum of (752) Sulamitis.

To correct for telluric absorptions and to obtain relative reflectance spectra, at least one solar analog star from the Landolt catalog (Landolt 1992) was observed each night. Whenever possible, more than one solar analog star was observed in order to improve the quality of the final spectra and to minimize potential variations in spectral slope introduced by the use of one single star. In those cases, the reflectance spectra obtained for the asteroids against each solar analog were averaged to obtain the final result. These stars were observed using the same spectral configuration as that for the asteroids, and at similar airmass. The list of solar analogs used in this study is shown in Table 1, including an identification number ID (the same as the one appearing in the last column of Table B.1), their right ascension (α) and declination (δ), and their visible magnitude (V). From the total of 36 observation nights, in 16 of them more than one solar analog was observed. We computed the possible fluctuations in spectral slopes on these nights due to the use of different stars. The largest value we obtained for the slope variation was 0.8%/1000 Å. As we will explain in the next section, this will be the dominating error regarding the asteroid spectral slopes. The resulting spectra were normalized to unity at 0.55 μm (this is the central wavelength of the V Johnson filter, which is widely used as reference for normalization in the visible) and are shown in Figs. A.1 and A.2.

3. Analysis and results

We have performed in-depth analysis on the obtained spectra. In the following sections we will describe how did we determine the taxonomy of the observed asteroids, how is the Yarkovsky effect affecting the family members, and, for the primitive objects in the sample, we have computed the spectral slopes, and we have looked for the absorption feature at 0.7 microns related to hydrated minerals on the surface of the asteroids. Finally, we compared our observations of (752) Sulamitis with the spectral data of this asteroid present in the literature.

[1] IRAF is distributed by the National Optical Astronomy Observatories, which are operated by the Association of Universities for Research in Astronomy, Inc., under cooperative agreement with the National Science Foundation.

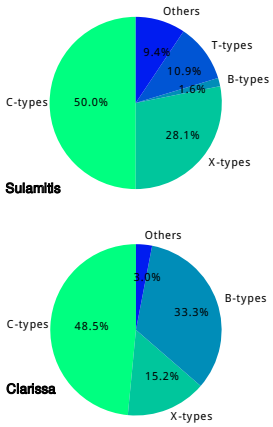

Fig. 1. Distribution of the taxonomical classes for the sample of 64 Sulamitis family asteroids (*top panel*) and the 33 Clarissa family asteroids (*bottom panel*) studied in this paper. The "Other" class includes all non-primitive taxonomies (S-types, V-types, and A-types).

3.1. Taxonomy determination

Once the data was reduced, we performed a taxonomic classification of the resulting spectra using the M4AST[2] online tool. The procedure used by the M4AST tool to classify asteroid spectra is summarized in Popescu et al. (2012) and is based on the DeMeo et al. (2009) taxonomy, an extension to the near-infrared of the Bus & Binzel (2002) taxonomy in the visible. Most of the classes in the DeMeo et al. (2009) overlap the ones in Bus & Binzel (2002), but, since we are working only with visible spectra (0.5–0.9 μm), we have checked individually those cases in which the taxonomical classes were exclusive to the DeMeo et al. (2009) taxonomy and classified them according to Bus & Binzel (2002).

To obtain robust results, we selected the χ^2 option (Bevington & Robinson 1992) available in the M4AST tool to test how well the spectra fitted to the templates. The best result was that corresponding to the smallest standard deviation. The taxonomical classification obtained for each asteroid is shown in the last column of Table B.2.

The classification procedure of the Sulamitis spectra provided a total of 32 C-type asteroids (including subclasses Ch and Cgh), 18 X-types (including one Xe-type), one B-type, seven T-types, and six objects with non-primitive classifications (three V-types, two A-types, and one Sr-type). In the case of the Clarissa family, we found 16 C-types (including one Cgh-type), five X-types, 11 B-types, and one V-type. These results are summarized in two pie charts (Fig. 1). As expected from the albedo

[2] Online tool for modeling of asteroid spectra: http://m4ast.imcce.fr/

A&A 610, A25 (2018)

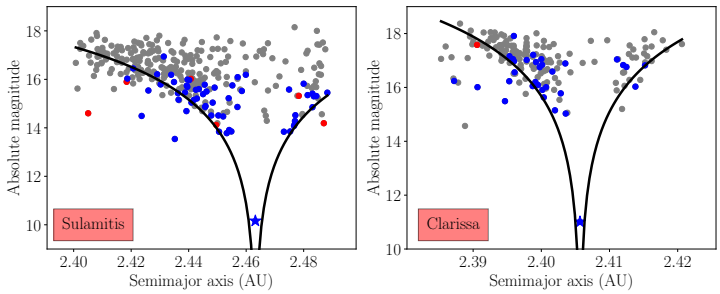

Fig. 2. Absolute magnitude (H) of the asteroids from the Sulamitis and Clarissa families as a function of their proper semi-major axes. Both families are shown in gray. The colored circles correspond to the objects observed in this study. Objects depicted in blue are primitive asteroids (C, X, B, T, and subclasses), while objects in red are non-primitive (A-, V-, and S-types). The family parent asteroids, (752) Sulamitis and (302) Clarissa, are represented as stars and are the largest objects in the families.

information extracted from the NEOWISE database, the majority of the asteroids in both families belong to primitive taxonomical classes. From the seven asteroids classified as non-primitive, we found albedo information from WISE database for two of them: (70528) and (79143). Both objects are classified as V-types and have $p_V > 0.2$, in agreement with their non-primitive nature.

3.2. The Yarkovsky effect on the Sulamitis and Clarissa families

As described by Vokrouhlický et al. (2006), collisional families show signs of having experienced dynamical spreading via the Yarkovsky thermal forces (spread in values of semi-major axis). Figure 2 shows the distribution in the absolute magnitude and semi-major axis space (H, a) for the members of both families. Solid curves in this figure define the boundaries of the family, also known as the "Yarkovsky cone", computed using the expression

$$H = 5 \times \log_{10}(\Delta a/C), \quad (1)$$

where $\Delta a = a - a_c$, with a_c defined as the center of the family. In practice, a_c is often close to, or the same as, the semimajor axis of the largest member of the family. C is a constant, different for each family, defined in Bottke et al. (2015), where they show that $C = 2.15 \times 10^{-5}$ AU for the Sulamitis family, and $C = 4.15 \times 10^{-6}$ AU for the Clarissa family. This Yarkovsky cone is an "envelope" around the center of the family, indicating the furthest that a family member can drift as a function of its size. Objects outside this cone are likely family interlopers. In addition, objects having a different composition from that of the family, are also considered as interlopers. In the cases we are studying, there are three objects belonging to the Sulamitis family with a non-primitive taxonomy lying outside this cone (from a total of six non-primitive asteroids). Regarding the Clarissa family, the only non-primitive object observed lies outside the Yarkovksy cone. This behavior is something we would expect given the definition of the Yarkovsky envelope. However, since this definition is empirical, we can find both primitive objects outside this cone (objects that might have drifted away from the family more than expected) and non-primitive objects inside the envelope. If we suppose that the original body had an homogeneous composition, the latter would likely be spurious members, which fall inside the family because of the exclusively dynamical definition of the group.

3.3. Spectral slopes

Primitive asteroids have almost featureless, linear spectra. Therefore we started by computing their spectral slope S', as defined by (Luu & Jewitt 1990), in the range from 0.55 to 0.90 μm, using the expression

$$S' = \left(\frac{\mathrm{d}S/\mathrm{d}\lambda}{S_{0.55}}\right), \quad (2)$$

where $\mathrm{d}S/\mathrm{d}\lambda$ is the rate of change of the reflectance in the aforementioned wavelength range, and $S_{0.55}$ is the reflectance at 0.55 μm. To compute S', we applied a linear least-squares fit between 0.55 and 0.90 μm to the whole spectrum of every primitive asteroid. The values we used for $\mathrm{d}S/\mathrm{d}\lambda$ and $S_{0.55}$ are, respectively, the slope of the aforementioned fit and its value at 0.55 microns[3]. S' is measured in units of %/1000 Å. The resulting values for the computed spectral slopes are shown in Table B.2. The variation in the slope due to the solar analog stars (see Sect. 2.2) is always larger than the 1σ standard deviation given by the linear fit. Therefore, the uncertainty in the slope will be 0.8%/1000 Å for all cases.

Figure 3 shows the distribution of the computed slopes for several cases. In the upper-left panel we show the slope distributions for the two families studied in this paper: Sulamitis and Clarissa. We can see that the slope distributions are different, with the Sulamitis family showing redder slope on average. The upper-right panel shows the comparison between the slope distributions of the largest primitive families in the inner main belt, Polana and Erigone, as computed by de León et al. (2016) and Morate et al. (2016). Here we observe a similar behavior to that of the previous case, with the slope distribution of the Erigone family being redder than that of Polana. This led

[3] We also computed the slopes using just the edges of the spectra, but we did not find any significant variation in the mean values, so we have kept our initial approach, which we also used in Morate et al. (2016).

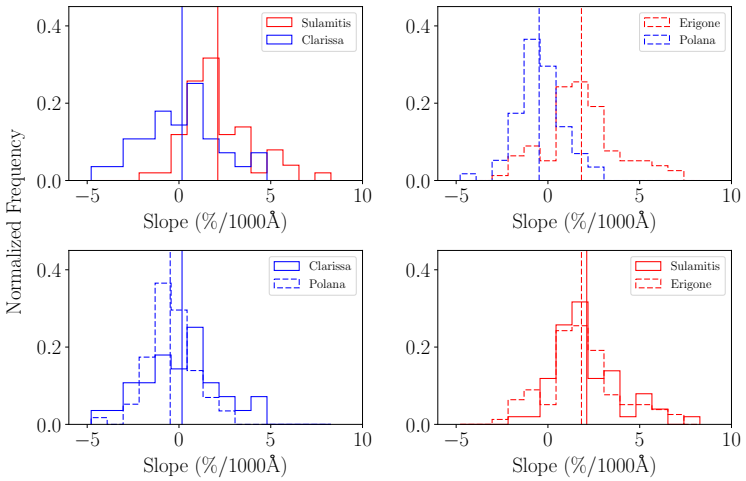

Fig. 3. Comparison of the spectral slope distributions of the primitive families in the inner main belt. The bin size is 0.87%/1000 Å. *From left to right, top to bottom*: sulamitis vs. Clarissa (this work), Polana vs. Erigone (the largest families, see Morate et al. 2016 for in-depth results), Clarissa vs. Polana, and Sulamitis vs. Erigone. Sulamitis and Erigone have been depicted in red, and Clarissa and Polana in blue. The vertical lines represent the mean values of the slope distributions. See text for more details.

us to compare the "blue" families (Clarissa and Polana) on one panel, and the "red" families (Sulamitis and Erigone) on other panel, in an attempt to better visualize their apparent similarities. We can see in Fig. 3 that the difference between the slope distributions of Clarissa and Polana (lower-left) is considerably small, while Sulamitis and Erigone (lower-right) show very similar slope distributions. The mean values for the four slope distributions are 2.12 (Sulamitis), 1.81 (Erigone), 0.17 (Clarissa), and −0.48 (Polana) %/1000 Å.

To quantify these similarities we run a two-sample Kolmogorov-Smirnov test (KS-test) over the two pairs of distributions (see Chap. 14 in Press 1992, and references within). We rejected the hypothesis of both samples coming from the same distribution if:

$$D_{m,n} > c(\alpha)\sqrt{\frac{m+n}{mn}}, \quad (3)$$

where $D_{m,n}$ is the Kolmogorov-Smirnov statistic, $c(\alpha) = 1.36$ for a confidence level of $\alpha = 0.05$, and m and n are the sizes of the compared samples. With these data, the critical value for the Sulamitis-Erigone test was $D_{\mathrm{crit,Sul,Eri}} = 0.23$, and the critical value for the Clarissa-Polana test was $D_{\mathrm{crit,Cla,Pol}} = 0.29$. When we run the KS-test, the results were $D_{\mathrm{Sul,Eri}} = 0.13$, and $D_{\mathrm{Cla,Pol}} = 0.27$. This means that we cannot reject the hypothesis of both samples coming from the same distribution in either case. Furthermore, if we compare any other pair of distributions among these four families, the results of the KS-test point out to samples coming from different distributions. Since this two-sample KS-test is used to check the difference between two one-dimensional cumulative distribution functions, we are plotting the functions for the four families in Fig. 4 for a graphical representation of this comparison.

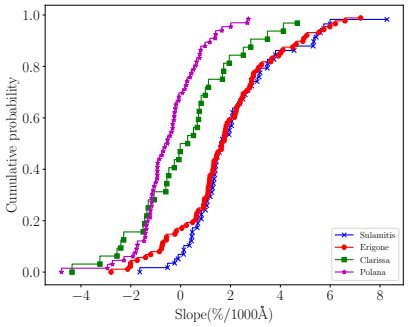

Fig. 4. Cumulative distribution function (CDF) of the slopes for the four primitive families of the inner main belt: Sulamitis and Clarissa (this work), Polana (de León et al. 2016), and Erigone (Morate et al. 2016). The Kolmogorov-Smirnov test compares the CDFs and gives an estimation of the differences.

A&A 610, A25 (2018)

3.4. Aqueous alteration

A considerable number of main belt primitive asteroids show an absorption feature centered around 0.7 μm in their visible spectra (Vilas 1994; Fornasier et al. 1999, 2014; Carvano et al. 2003; Rivkin 2012; Morate et al. 2016), attributed to charge transfer transitions in oxidized iron, indicative of, or associated to, the presence of aqueous altered minerals on their surfaces (Vilas & Gaffey 1989; Vilas 1994; Barucci et al. 1998). This is the case for a significant fraction of the asteroids from the Sulamitis family (evident from a simple visual inspection of the obtained visible spectra, see Fig. A.1). In addition, previous spectroscopic observations in the visible of (752) Sulamitis (Bus & Binzel 2002; Lazzaro et al. 2004) have shown the presence of this aqueous alteration band. As in the case of (163) Erigone and the asteroids from the Erigone family, we study here this particular feature, following a similar procedure as that described in Morate et al. (2016).

The first step was to compute a fourth-order polynomial fit to the entire spectrum. Then, we removed the continuum of the absorption band. This continuum was obtained by fitting a straight line tangent to the polynomial fit in the local maxima (around 0.55 μm and 0.87 μm), which are the limits of the 0.7 μm absorption band. In some particular cases the polynomial fit did not present one of the two local maxima, although the absorption band was clearly seen in the spectra. For such cases, we just used the reflectance values in the regions delimiting the band (0.54−0.56 μm on the left side and 0.86−0.88 μm on the right) and computed a straight line. Once the continuum was fitted, we removed it from the spectrum by dividing the reflectance data by the continuum straight line. After this, we iterated the above process once, in order to make an accurate correction of the continuum slope.

In order to compute the depth and the central wavelength position of the absorption band and their corresponding errors we run a Monte Carlo model with 1000 iterations, randomly removing 10% of the points from the spectrum at each iteration, then repeating the above described procedure. The central wavelength position corresponds to the position of the local minimum of the band after the continuum removal. The band depth is computed as the difference, in %, between a reflectance value of 1 and the reflectance value at this minimum. The final values for the band depth and central wavelength are computed as the mean values obtained for the full Monte Carlo run, and the errors are the corresponding 1σ standard deviations of the mean. We also computed the standard deviation of the fit residuals within the band (i.e., between 0.53 and 0.84 μm), and then we compared this result with the mean value obtained for the band depth. Whenever the computed band depth was larger (considering its associated error) than the computed residual, we considered that the band was real (positive detection). On the contrary, cases where the depth was smaller than the residual, were considered as negative detections (no band). Table B.2 shows the values for the computed band centers and depths, as well as the residual, and a flag indicating whether the asteroid presents the 0.7 μm absorption band (YES/NO). Those cases having the same value for the band depth and the residual are marked with an asterisk, and were visually inspected to decide if the band was real or not.

According to our detection method, we found that, at least, 35 asteroids (out of 58 primitive objects) from the Sulamitis family present an absorption band at 0.7 μm. This band is present regardless the specific primitive spectral class. Figure 5 shows the proportion of asteroids in the Sulamitis family showing the hydration band for each primitive class: ~69% for C-types

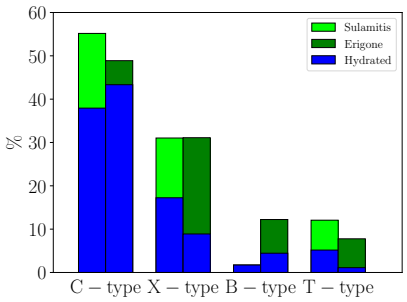

Fig. 5. Proportion of asteroids from each primitive class with respect to the total number of primitive asteroids found for each family. The percentage of asteroids showing the 0.7 μm absorption band within each class is shown in blue. We compare the results obtained for the Sulamitis family (this work, light green) with those obtained in Morate et al. (2016) for the Erigone family (dark green).

(Vilas 1994 and Fornasier et al. 2014 found an incidence of 47.7% and 50.7% in C-type asteroids, respectively, in good agreement with our result), ~56% for X-types, and ~43% for T-types. There is only one asteroid classified as a B-type and it shows the hydration band. The mean values we found for both the band depth, 2.7 ± 1.2%, and the band center position, 7130 ± 170 Å, are in good agreement with those obtained by Fornasier et al. (2014): 2.9 ± 1.3% for the band depth and 6900 ± 170 Å for the band center of the hydrated objects in the inner belt studied in their work. In the case of asteroids in the Clarissa family only three asteroids from the 30 analyzed present the 0.7 μm absorption band, two B-types and one C-type.

Given that the hydration band detection method used in the present work is similar, but not equal, to the one used in Morate et al. (2016), we have run some tests to look for consistency between results. For this, we conducted the analysis presented here on the spectra from the Erigone family, finding the same detections with both methods. However, for future uses, we prefer the one presented in this work, since it is able to detect bands without the need of a previously imposed threshold, that is, it works in an almost unsupervised way.

3.5. Other observations of (752) Sulamitis

Two other visible spectra of asteroid (752) Sulamitis exist in the literature: one obtained on November 22, 1992 within the SMASS survey (Xu et al. 1995), and another obtained on January 26, 2001 as part of the S_3OS_2 survey (Lazzaro et al. 2004). These two spectra, together with the two spectra presented in this work, are shown in Fig. 6, with a vertical offset for clarity.

We have run our codes to compute the slopes of the spectra. These slopes are computed using the procedure explained in Sect. 3.3. The spectral slope shows random variations (see Fig. 6): it is at its maximum around six to seven degrees, then it diminishes around a phase angle of 17°, to rise again at 20°, and then going down again at 24°. Although it might be tempting to fit a straight line to these four points and suggest a decrease of the slope with phase angle, we have found no references in

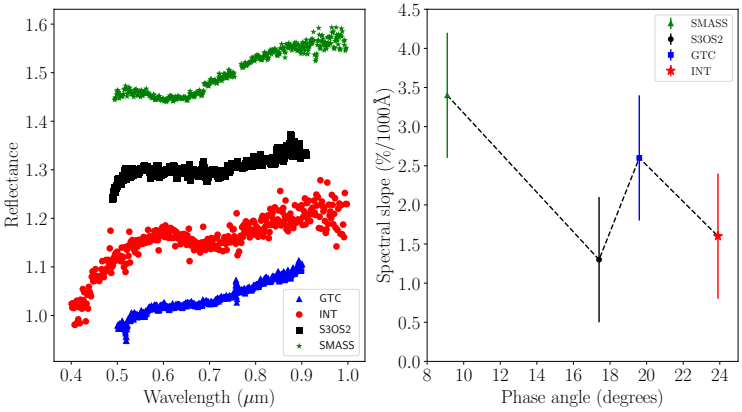

Fig. 6. Visible spectra of asteroid (752) Sulamitis currently available (*left panel*). The four spectra are normalized to unity at 0.55 μm and offset vertically for clarity. In the *right panel* we show the computed slope of the spectra as a function of phase angle at the moment of the observations.

Table 2. Information for the different spectra of (752) Sulamitis available in the literature, and also for the ones we have obtained.

Date	Survey or telescope	Phase (°)	Slope (%/1000 Å)	Band center (Å)	Band depth (%)
1992-November-29	SMASS	9.1	3.4	6520 ± 30	2.30 ± 0.07
2001-January-26	S_3OS_2	17.4	1.3	7200 ± 6	2.15 ± 0.03
2015-July-21	INT	23.9	1.6	7390 ± 40	2.03 ± 0.18
2015-August-31	GTC	19.6	2.6	7260 ± 9	1.61 ± 0.02

the literature regarding such phase bluing effect. On the contrary, phase angle induced effects can manifest themselves as phase reddening, which produces an artificial increase (reddening) of the spectral slope, according to Gradie et al. (1980); Gradie & Veverka (1986), and Clark et al. (2002). Positive slope variations with respect to the phase angle have been documented for primitive classes: Lumme & Bowell (1981) found a variation of 0.15 ± 0.12%/1000 Å/degree for C-types; Dahlgren et al. (1997) found a slope variation of 0.04 ± 0.03%/1000 Å/degree for D-types and 0.003 ± 0.05%/1000 Å/degree for P-types, although they consider this effect negligible. Anyway, given the errors in our slope points, we can neither confirm nor reject the presence of this effect on (752) Sulamitis.

We have also analyzed the presence of the hydration band, and we have found that depending on the observation, the band's depth and center values are slightly different (see Table 2). A possible explanation could be the difference in phase angles for each of the observations. But, again, we do not find consistent correlations between the phase angle and the band depth or center. Up to now, there are no known studies relating this 0.7 micron band with the phase angle of the observation.

Finally, we performed a taxonomic analysis of these four spectra using the M4AST online tool. The results yielded two different classifications for the four spectra: the SMASS and the GTC spectra were classified as X-types (higher slopes, see Table 2), while the S_3OS_2 and the INT spectra are classified as Cgh (smaller slopes). This points out the dependence of the taxonomy on the spectral slope, which is the main parameter for the taxonomic classification of primitive asteroids[4]. More observations of this asteroid, covering a wider range of phase angles, are needed in order to search for consistent changes in the spectral slope and the band presence to better understand this behavior.

4. Discussion

No previous spectroscopic studies had been performed until now on the Sulamitis nor the Clarissa primitive collisional families. Only the parent bodies, (752) Sulamitis and (302) Clarissa had been observed before: (752) was observed as part of the SMASS and the S_3OS_2 surveys (Xu et al. 1995; Lazzaro et al. 2004) and (302) Clarissa was observed as part of the ECAS survey (Zellner et al. 1985). (752) Sulamitis shares the particular spectroscopic feature at 0.7 μm with most of its family members (about 60%), while the spectrum of (302) Clarissa does not show this hydration feature, as is the case for the large majority of its family members. The other two primitive low-inclination families located in the inner belt, Polana and Erigone, have been

[4] For the analysis carried out in the present work, we have used the taxonomic class obtained for the GTC spectrum, since its S/N is much higher than that of the INT spectrum.

A&A 610, A25 (2018)

studied recently (Walsh et al. 2013; Dykhuis & Greenberg 2015; de León et al. 2016; Pinilla-Alonso et al. 2016; Morate et al. 2016). In the next paragraphs we discuss the results obtained here for the Sulamitis and Clarissa families, and we will compare those with the ones on the literature for Polana and Erigone.

The Sulamitis family presents a different distribution of taxonomical classes from that of the Clarissa family. In our sample, we found primarily C- and X-type objects (50.0% and 28.1% respectively), few T-types (10.9%), and just one B-type, plus six interlopers (V-, A-, and S-types), in agreement with the classification proposed in Nesvorný et al. (2015), where Sulamitis is classified as a C-type. On the contrary, in the Clarissa family, although there is a similar C-type proportion (48.5%), we found that B-types are more common (33.3%), with few X-types (15.2%) and only one S-type. This result differs from the classification presented in Nesvorný et al. (2015) for the Clarissa family, where it appears as an X-type (using SDSS photometric data), while our results from visible spectroscopy point to a C/B-type family. In addition, the slope distribution for the objects in the Sulamitis family is fairly redder than that of the Clarissa family, as can be seen in Fig. 3, mainly due to the larger fraction of X-types found in the former. These results confirm the primitive composition of both families. However, their surface compositions seem to be different.

When comparing the Sulamitis family slope distribution with the slope distribution obtained in Morate et al. (2016) for the Erigone family, we find that they are very similar (see lower-left panel of Fig. 3), with a mean spectral slope of 2.1 ± 1.8%/1000 Å for the Sulamitis family, vs. a value of 1.8 ± 2.0%/1000 Å for the Erigone family. The same happens when we compare the slope distributions of the Clarissa and Polana families and their mean spectral slopes: 0.2 ± 2.0%/1000 Å for Clarissa vs. −0.5 ± 1.3%/1000 Å for Polana (de León et al. 2016). The KS-test we run on both pairs of distributions (Sulamitis vs. Erigone, and Clarissa vs. Polana), tells us that we cannot reject the hypothesis that one sample pair comes from one common distribution, and the other sample pair comes from another common distribution.

In addition, both family pairs (Sulamitis-Erigone and Clarissa-Polana) show a similar presence of the 0.7 μm aqueous alteration feature: Sulamitis and Erigone present, respectively, 60.3% (this work) and 57.7% (Morate et al. 2016) of primitive asteroid spectra with the hydration band (see Fig. 5 for a more in-depth comparison of the aqueous alteration presence between these families); on the other hand, Clarissa and Polana show, respectively, three (this work) and one (de León et al. 2016) spectra with the 0.7 μm absorption feature within the two studied samples, that is, there are two "wet" families (Erigone and Sulamitis), and two "dry" families (Polana and Clarissa).

The presence of a primitive collisional family, Sulamitis, located between 2.4 and 2.5 AU, and with the majority of its members showing the 0.7 μm hydration band, is in good agreement with the results presented by Fornasier et al. (2014), where they suggested that the aqueous alteration processes dominate in primitive asteroids located between 2.3 and 3.1 AU. Moreover, it is stated that the proportion of hydrated primitive objects (regardless the taxonomic class) in the region where the Sulamitis family is located is 64%, in good agreement with the proportion of hydrated objects we have found in our sample, 60.3% (35 out of 58).

As it was the case in Morate et al. (2016), we found no significant correlations between the band depths or the band centers and the taxonomical class, the orbital parameters, or the albedo of the objects. A similar lack of correlation is found by Carvano et al. (2003) and Fornasier et al. (2014) in their respective studies for asteroids through the whole main belt. Interestingly, these and other authors find that the percentage of hydrated asteroids is somehow correlated with their size, the aqueous alteration process being less effective for bodies smaller than 50 km, and dominating in the 50−240 km size range. We cannot search for correlations between hydration and size in our sample, as we are studying asteroids within collisional families having about the same size: the mean sizes of the objects studied in this work in the Sulamitis and the Erigone collisional families are 5.5 km and 4.2 km respectively. The presence of such large fraction of small asteroids showing the 0.7 μm absorption band can be explained by the fact that they are fragments of larger bodies that were aqueously altered: both (752) Sulamitis and (163) Erigone have diameters larger than 50 km and therefore the parent bodies of these two families were large enough to retain water ice in their interiors and produce internal heating sufficient to melt the ice.

Regarding the difference in the presence of the aqueous alteration for both families, it is most likely explained by their two parent bodies. Asteroid (302) Clarissa shows no signs at all of the hydration feature at 0.7 μm, while (752) Sulamitis shows evidence of aqueous alteration. Therefore, the presence of the hydration feature in the spectra of most of its family members is somewhat expected for the latter. This was also the case for asteroid (163) Erigone and the members of its collisional family (Morate et al. 2016). In this paper we proposed that space weathering could be acting on the surfaces of C-type asteroids by removing the aqueous alteration band: the older the family, the less the fraction of objects showing the 0.7 μm absorption feature. According to Bottke et al. (2015), the estimated ages for Clarissa, Erigone, Sulamitis, and Polana families are ∼60 Myr, 130 ± 30 Myr, 200 ± 40 Myr, and 1400 ± 150 Myr, respectively. Therefore, we can rule out the space weathering explanation, since, according to these ages, Clarissa, the youngest member of this group, should present a higher number of hydrated asteroids if this hydration feature was present at any point during the family's life.

To end the discussion, we would like to note that Sulamitis and Clarissa are two primitive families which share with the Erigone and Polana families, respectively, a) similar proportion of taxonomic classes; b) similar slope distribution; c) similar presence of the 0.7 μm aqueous alteration feature; and d) similar proper orbital elements, specifically semi-major axis and inclination (see Fig. 1 from Morate et al. 2016). Having this in mind, we would like to propose here the possibility of a link between these four families (two links, actually). One link between Erigone and Sulamitis (which, in addition, have similar ages), and another link between the Clarissa and Polana families. The question of whether they could be related in some way, for example cratering events or fragmentation of bigger asteroids Milani et al. (2014), is open for future discussion.

5. Conclusions

We studied a total of 97 visible spectra of asteroids in the Sulamitis and Clarissa primitive families. All spectra were obtained with the 10.4 m Gran Telescopio Canarias and had never been spectroscopically observed before (with the exception of the parent bodies). (752) Sulamitis was also observed with the 2.5 m *Isaac Newton* Telescope. We have sampled 64 out of the total of 303 asteroids in the Sulamitis family (∼21% of the family) and 33 out of 179 in the case of Clarissa (∼18%).

In terms of taxonomical distribution, in the case of the Sulamitis family we found that 50% of the asteroids are classified as C-type objects, 28% as X-types, 11% as T-types, and just one B-type, being the 9% of the objects in the sample spectral interlopers (three V-types, two A-types, and one Sr-type). The taxonomical distribution for the Clarissa family is clearly different from that of Sulamitis: we see a similar proportion of C-types (48%), but 33% of the objects are classified as B-types, 15% as X-types, and we found just one interloper.

The study of aqueous alteration performed on the Sulamitis primitive sample shows a high number of hydrated asteroids: 35 out of 58 (about 60%). This percentage of aqueously altered asteroids is comparable with the results obtained by Morate et al. (2016) for the Erigone collisional family (about 58%). Moreover, the taxonomical distribution is very similar between Sulamitis and Erigone families. The Clarissa family, however, does not show almost any signs of hydration (just three objects in the sample present the aqueous alteration band). This result, together with its taxonomical and slope distribution is, again, comparable with the results obtained by de León et al. (2016) for the Polana family.

Given all the physical similarities found between these families, and given that they also share similar orbital properties, we hereby propose the possibility of the existence of a link between the Erigone and Sulamitis families, and also between the Polana and the Clarissa family. Future work should include a more detailed analysis on the dynamical evolution of these groups, in order to confirm or discard a possible common origin.

Acknowledgements. D.M. gratefully acknowledges the Spanish Ministry of Economy and Competitiveness (MINECO) for the financial support received in the form of a Severo-Ochoa PhD fellowship, within the Severo-Ochoa International PhD Program. D.M., J.d.L. and J.L. acknowledge support from the project AYA2012-39115-C03-03 and ESP2013-47816-C4-2-P (MINECO). J.d.L. acknowledges financial support from the Spanish MINECO under the 2015 Severo Ochoa Program MINECO SEV-2015-0548. M.D.P. acknowledges support from the CAPES (Brazil). H.C. acknowledges support from NASA's Near-Earth Object Observations program and from the Center for Lunar and Asteroid Surface Science funded by NASA's SSERVI program at the University of Central Florida. D.M. gratefully acknowledges Dr. Jorge Carvano for the discussions on the improvement of the detection method for the aqueous alteration features. The results obtained in this paper are based on observations made with the Gran Telescopio Canarias (GTC), installed in the Spanish Observatorio del Roque de los Muchachos of the Instituto de Astrofísica de Canarias, in the island of La Palma. The authors thank Marcel Popescu for the observing time to obtain the second spectrum of (752) on program C97-2015 on the *Isaac Newton* Telescope (INT).

References

Barucci, M. A., Doressoundiram, A., Fulchignoni, M., et al. 1998, Icarus, 132, 388
Bevington, P. R., & Robinson, D. K. 1992, Data reduction and error analysis for the physical sciences (New York: McGraw-Hill)
Binzel, R. P., & Xu, S. 1993, Science, 260, 186
Bottke, W. F., Morbidelli, A., Jedicke, R., et al. 2002, Icarus, 156, 399
Bottke, W. F., Vokrouhlický, D., Walsh, K. J., et al. 2015, Icarus, 247, 191
Bus, S. J., & Binzel, R. P. 2002, Icarus, 158, 146
Campins, H., Morbidelli, A., Tsiganis, K., et al. 2010, ApJ, 721, L53
Campins, H., de León, J., Morbidelli, A., et al. 2013, AJ, 146, 26
Carvano, J. M., Mothé-Diniz, T., & Lazzaro, D. 2003, Icarus, 161, 356
Cepa, J. 2010, in Highlights of Spanish Astrophysics V, eds. J. M. Diego, L. J. Goicoechea, J. I. González-Serrano, & J. Gorgas, 15
Cepa, J., Aguiar, M., Escalera, V. G., et al. 2000, in Optical and IR Telescope Instrumentation and Detectors, eds. M. Iye, & A. F. Moorwood, SPIE Conf. Ser., 4008, 623
Clark, B. E., Helfenstein, P., Bell, J. F., et al. 2002, Icarus, 155, 189
Dahlgren, M., Lagerkvist, C.-I., Fitzsimmons, A., Williams, I. P., & Gordon, M. 1997, A&A, 323, 606
de León, J., Pinilla-Alonso, N., Delbo, M., et al. 2016, Icarus, 266, 57
DeMeo, F. E., Binzel, R. P., Slivan, S. M., & Bus, S. J. 2009, Icarus, 202, 160
De Prá, M. N., Pinilla-Alonso, N., Carvano, J. M. F., et al. 2017, Icarus, accepted
Dykhuis, M. J., & Greenberg, R. 2015, Icarus, 252, 199
Fornasier, S., Lazzarin, M., Barbieri, C., & Barucci, M. A. 1999, A&AS, 135, 65
Fornasier, S., Lantz, C., Barucci, M. A., & Lazzarin, M. 2014, Icarus, 233, 163
Gayon-Markt, J., Delbo, M., Morbidelli, A., & Marchi, S. 2012, MNRAS, 424, 508
Gradie, J., & Veverka, J. 1986, Icarus, 66, 455
Gradie, J., Veverka, J., & Buratti, B. 1980, in Lunar and Planetary Science Conference Proceedings 11, ed. S. A. Bedini, 799
Howell, E. S., Rivkin, A. S., Vilas, F., et al. 2011, EPSC-DPS Joint Meeting 2011, 637
Landolt, A. U. 1992, AJ, 104, 340
Lauretta, D. S., Drake, M. J., Benzel, R. P., et al. 2010, Meteoritics and Planetary Science Supplement, 73, 5153
Lazzaro, D., Angeli, C. A., Carvano, J. M., et al. 2004, Icarus, 172, 179
Lumme, K., & Bowell, E. 1981, AJ, 86, 1705
Luu, J. X., & Jewitt, D. C. 1990, AJ, 99, 1985
Mainzer, A. K., Bauer, J. M., Cutri, R. M., et al. 2016, NEOWISE Diameters and Albedos V1.0. EAR-A-COMPIL-5-NEOWISEDIAM-V1.0. NASA Planetary Data System
Milani, A., Cellino, A., Knežević, Z., et al. 2014, Icarus, 239, 46
Morate, D., de León, J., De Prá, M., et al. 2016, A&A, 586, A129
Nesvorny, D. 2015, Nesvorny HCM Asteroid Families V3.0. EAR-A-VARGBDET-5-NESVORNYFAM-V3.0. NASA Planetary Data System
Nesvorný, D., Brož, M., & Carruba, V. 2015, Identification and Dynamical Properties of Asteroid Families, eds. P. Michel, F. E. DeMeo, & W. F. Bottke, 297
Pinilla-Alonso, N., de León, J., Walsh, K. J., et al. 2016, Icarus, 274, 231
Popescu, M., Birlan, M., & Nedelcu, D. A. 2012, A&A, 544, A130
Press, W. H. 1992, Numerical recipes 2nd edn.: The art of scientific computing (Cambridge University Press)
Rivkin, A. S. 2012, Icarus, 221, 744
Tsuda, Y., Yoshikawa, M., Abe, M., Minamino, H., & Nakazawa, S. 2013, Acta Astronautica, 91, 356
Vilas, F. 1994, Icarus, 111, 456
Vilas, F., & Gaffey, M. J. 1989, Science, 246, 790
Vokrouhlický, D., Brož, M., Bottke, W. F., Nesvorný, D., & Morbidelli, A. 2006, Icarus, 182, 118
Walsh, K. J., Delbó, M., Bottke, W. F., Vokrouhlický, D., & Lauretta, D. S. 2013, Icarus, 225, 283
Xu, S., Binzel, R. P., Burbine, T. H., & Bus, S. J. 1995, Icarus, 115, 1
Zappala, V., & Cellino, A. 1994, in Asteroids, Comets, Meteors 1993, eds. A. Milani, M. di Martino, & A. Cellino, IAU Symp., 160, 395
Zappala, V., Cellino, A., Farinella, P., & Knezevic, Z. 1990, AJ, 100, 2030
Zellner, B., Tholen, D. J., & Tedesco, E. F. 1985, Icarus, 61, 355

A&A 610, A25 (2018)

Appendix A: Visible spectra

We present here the visible spectra of the asteroids from the Sulamitis and Clarissa collisional families studied in this paper. A total of 64 and 33 asteroids were observed from each family, respectively. Spectra are normalized to unity at 0.55 μm.

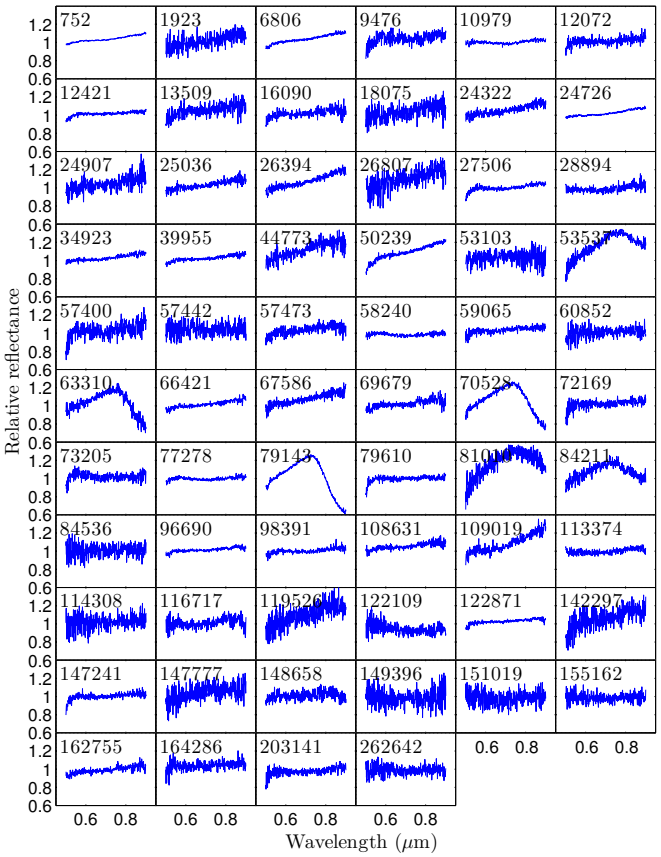

Fig. A.1. Visible spectra of the 64 observed asteroids from the Sulamitis family.

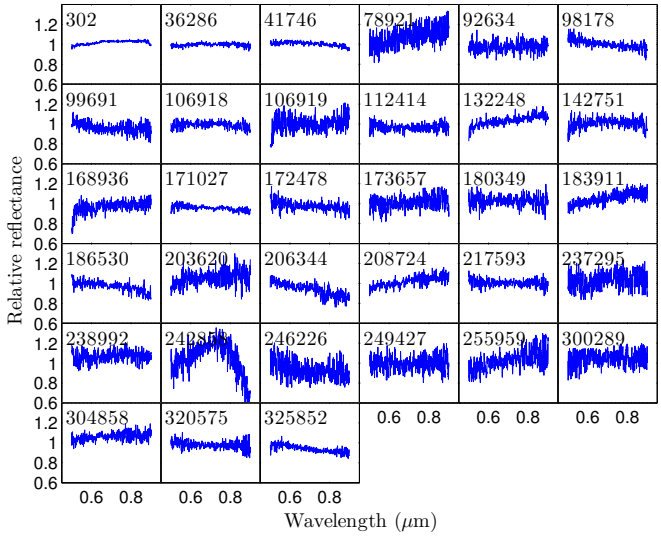

Fig. A.2. Visible spectra of the 33 observed asteroids from the Clarissa family.

A&A 610, A25 (2018)

Appendix B: Additional tables

Table B.1. Observational circumstances for the asteroids presented in this work.

Object	Date	UT Start	Exp. time (s)	m_V	SAs
Sulamitis					
752	01-09-2015	04:50	3 × 30	14.5	1, 7
752[1]	22-07-2015	04:57	3 × 180	15.2	1
1923	01-04-2015	23:33	3 × 100	17.8	2, 3
6806	17-02-2016	03:03	3 × 300	17.9	2
9476	27-01-2015	20:57	3 × 300	18.7	1, 2, 3
10979	04-08-2015	02:35	3 × 250	17.9	6
12072	03-09-2015	05:05	3 × 300	18.9	1, 7
12421	29-02-2016	22:29	2 × 250	18.6	2
13509	25-03-2016	21:26	3 × 250	18.1	2
16090	08-04-2016	23:16	3 × 500	20.3	2, 3
18075	27-02-2015	22:19	3 × 400	19.9	2, 3, 4
24322	14-05-2016	22:32	3 × 300	19.5	3
24726	12-03-2016	01:22	3 × 300	17.7	3
24907	01-03-2016	21:21	3 × 400	19.3	2
25036	12-03-2016	00:57	3 × 300	18.6	3
26394	23-05-2016	22:37	3 × 350	19.2	2
26807	01-04-2015	22:00	3 × 300	19.3	2, 3
27506	30-01-2015	00:38	3 × 200	18.1	2
28894	29-01-2015	06:43	3 × 350	19.3	3
34923	12-03-2016	01:52	3 × 400	19.1	3
39955	05-01-2016	21:41	3 × 300	19.1	1, 2
44773	09-04-2016	00:03	3 × 400	20.3	2, 3
50239	27-01-2015	22:30	5 × 300	18.4	1, 2, 3
53103	28-02-2015	04:57	3 × 400	19.7	2, 3, 4
53537	04-04-2015	23:27	3 × 300	18.9	2, 3, 4
57400	28-01-2015	06:43	3 × 500	20.5	1, 2, 3
57442	02-04-2015	02:03	6 × 150	18.1	2, 3
57473	31-03-2015	03:33	3 × 500	19.7	3
58240	17-02-2016	01:25	3 × 500	19.3	2
59065	28-02-2015	00:33	3 × 300	19.0	2, 3, 4
60852	05-04-2015	00:23	3 × 400	19.8	2, 3, 4
63310	08-04-2016	22:47	3 × 400	20.1	2, 3
66421	05-01-2016	22:54	3 × 400	19.5	1, 2
67586	29-11-2015	23:00	3 × 600	19.4	1
69679	05-01-2016	22:02	3 × 500	20.3	1, 2
70528	13-05-2016	21:45	3 × 400	19.2	3
72169	01-09-2015	05:41	3 × 500	20.1	1, 7
73205	27-11-2015	22:31	3 × 500	20.5	1, 2, 7
77278	17-02-2016	02:08	3 × 500	18.9	2
79143	13-05-2016	21:22	3 × 300	18.3	3
79610	28-01-2015	01:00	3 × 300	19.2	1, 2, 3
81010	27-02-2015	23:50	3 × 500	20.0	2, 3, 4
84211	30-01-2015	21:53	3 × 300	19.1	1
84536	04-04-2015	23:50	3 × 500	20.3	2, 3, 4
96690	03-09-2015	03:10	3 × 300	18.7	1, 7
98391	03-09-2015	04:03	3 × 350	19.6	1, 7
108631	13-03-2015	22:06	3 × 500	19.7	2
109019	11-02-2015	03:16	3 × 450	19.6	3
113374	14-05-2016	22:54	3 × 400	19.9	3
114308	05-04-2015	01:00	3 × 350	19.9	2, 3, 4
116717	15-05-2016	22:11	3 × 600	19.4	3, 4
119526	31-05-2015	22:46	3 × 300	19.6	4, 5
122109	04-05-2015	22:49	3 × 450	19.7	3, 4
122871	03-09-2015	03:26	3 × 300	18.9	1, 7
142297	30-01-2015	22:38	3 × 500	20.0	1
147241	28-01-2015	01:37	3 × 400	19.6	1, 2, 3
147777	05-04-2015	01:37	3 × 300	19.8	2, 3, 4
148658	28-02-2015	03:40	3 × 400	19.5	2, 3, 4
149396	31-05-2015	23:10	3 × 350	20.0	4, 5
151019	05-04-2015	03:34	6 × 150	19.4	2, 3, 4
155162	05-04-2015	04:02	12 × 125	19.4	2, 3, 4
162755	05-01-2016	23:22	3 × 500	20.1	1, 2
164286	01-09-2015	05:05	3 × 500	20.0	1, 7
203141	27-11-2015	23:04	3 × 400	19.9	1, 2, 7
262642	28-02-2015	00:57	3 × 500	20.3	2, 3, 4
Clarissa					
302	31-08-2016	21:13	3 × 15	15.9	6
36286	13-06-2016	04:13	3 × 400	19.4	5
41746	28-11-2015	02:43	3 × 200	17.7	1, 2, 7
78921	29-02-2016	21:50	3 × 500	20.7	2
92634	29-11-2015	23:24	3 × 500	20.1	1
98178	27-11-2015	23:37	3 × 350	19.6	1, 2, 7
99691	16-12-2015	03:03	3 × 500	20.1	1, 2
106918	21-12-2015	01:53	3 × 600	20.2	1
106919	28-11-2015	04:11	3 × 500	20.4	1, 2, 7
112414	23-05-2016	21:57	3 × 600	20.6	3
132248	09-12-2015	04:20	3 × 450	19.4	1, 2
142751	16-05-2016	00:03	3 × 500	20.1	3, 4
168936	29-12-2015	00:33	3 × 400	19.4	1, 2
171027	20-12-2015	23:11	3 × 500	19.8	1
172478	21-12-2015	02:46	3 × 600	20.8	1
173657	20-03-2016	04:45	3 × 600	20.4	4
180349	15-05-2016	23:08	3 × 600	20.4	3, 4
183911	12-06-2016	04:28	3 × 500	19.4	5
186530	13-06-2016	03:20	3 × 600	19.5	5
203620	09-12-2015	01:54	3 × 500	20.4	1, 2
206344	09-12-2015	03:06	3 × 600	20.2	1, 2
208724	16-12-2015	02:10	3 × 600	20.5	1, 2
217593	16-05-2016	01:06	3 × 500	19.8	3, 4
237295	28-12-2015	22:54	3 × 600	21.1	1, 2
238992	09-12-2015	01:12	3 × 600	20.8	1, 2
242858	15-12-2015	22:46	3 × 600	21.0	1, 2
246226	15-12-2015	23:36	3 × 600	20.8	1, 2
249427	29-02-2016	21:09	3 × 600	21.5	2
255959	20-03-2016	05:27	4 × 600	20.7	4
300289	28-12-2015	22:08	3 × 600	21.1	1, 2
304858	09-12-2015	02:34	3 × 450	19.9	1, 2
320575	09-04-2016	00:43	3 × 600	20.4	2, 3
325852	09-04-2016	01:34	3 × 600	20.3	2, 3

Notes. See Table 1 for the ID number of each solar analog star. [(1)] Observed with INT.

Table B.2. Orbital and physical parameters of the observed asteroids.

Object	a (AU)	e	i (°)	H_V (km)	D (km)	err$_D$	p_V	err$_{pV}$	Slope (±0.8%/1000 Å)	Band	Center (Å)	Depth (%)	Residual	Class
Sulamitis														
752	2.463	0.091	5.047	10.2	60.17	0.25	0.045	0.008	2.6	YES	7254 ± 6	1.65 ± 0.01	0.25	X
752[1]	″	″	″	″	″	″	″	″	1.6	YES	7390 ± 50	2.04 ± 0.19	1.15	Cgh
1923	2.435	0.083	5.076	13.5	14.59	5.40	0.029	0.018	3.7	NO	–	1.93 ± 0.16	3.28	X
6806	2.455	0.091	5.036	13.8	8.44	3.94	0.065	0.082	3.5	YES	7202 ± 5	1.52 ± 0.02	0.49	X
9476	2.453	0.090	4.990	13.8	8.61	2.34	0.066	0.066	0.7	YES	7360 ± 10	3.94 ± 0.10	2.12	Cgh
10979	2.457	0.090	5.036	14.9	5.33	0.07	0.057	0.009	1.0	YES	7036 ± 8	3.05 ± 0.05	0.66	Cgh
12072	2.452	0.092	5.100	14.5	7.80	2.58	0.052	0.115	1.4	YES	7335 ± 24	2.87 ± 0.10	1.88	Cgh
12421	2.451	0.089	4.953	13.8	6.79	2.62	0.099	0.108	0.8	YES	7292 ± 9	1.33 ± 0.03	0.60	Cgh
13509	2.477	0.090	4.938	14.1	10.66	5.44	0.031	0.269	2.2	NO	–	1.68 ± 0.12	2.73	X
16090	2.442	0.089	4.932	15.2	5.37	0.13	0.051	0.009	1.5	YES	7079 ± 9	2.18 ± 0.08	1.95	Cgh
18075	2.477	0.093	5.126	14.5	–	–	–	–	3.2	NO	–	2.51 ± 0.17	3.41	X
24322	2.424	0.088	4.866	14.5	6.55	3.43	0.063	0.072	3.8	YES	7008 ± 14	1.95 ± 0.07	1.40	X
24726	2.454	0.090	4.953	13.9	9.24	4.12	0.050	0.120	2.8	YES	7012 ± 6	1.98 ± 0.02	0.35	X
24907	2.454	0.094	5.134	15.2	–	–	–	–	3.5	NO	–	2.86 ± 0.14	3.38	X
25036	2.477	0.091	4.990	14.3	7.31	1.49	0.058	0.036	3.2	YES	7000 ± 11	1.76 ± 0.07	1.42	X
26394	2.450	0.090	5.051	14.5	8.41	2.75	0.033	0.038	6.0	YES	7079 ± 11	2.73 ± 0.05	1.19	T
26807	2.473	0.092	5.019	13.8	–	–	–	–	5.6	NO	–	–0.22 ± 0.17	4.29	T
27506	2.483	0.093	5.280	14.8	5.86	2.32	0.056	0.042	1.7	YES	7201 ± 4	3.29 ± 0.04	0.91	Cgh
28894	2.477	0.094	5.111	14.2	9.41	3.66	0.042	0.052	1.9	YES	6864 ± 18	3.37 ± 0.08	1.63	Cgh
34923	2.442	0.091	4.963	15.6	–	–	–	–	2.5	YES	6984 ± 10	1.78 ± 0.04	0.75	X
39955	2.439	0.086	4.916	14.7	–	–	–	–	2.0	YES	7274 ± 11	1.61 ± 0.04	0.71	X
44773	2.426	0.089	4.970	15.5	3.37	0.24	0.090	0.007	5.3	NO	–	0.63 ± 0.25	2.48	T
50239	2.475	0.093	5.061	13.8	9.22	0.33	0.057	0.007	5.4	YES	7331 ± 6	2.29 ± 0.04	0.86	T
53103	2.443	0.085	5.000	15.2	4.93	0.02	0.053	0.007	–0.1	NO	–	–0.92 ± 0.09	3.75	C
53537	2.450	0.093	4.974	14.1	–	–	–	–	N.A.	N.A.	N.A.	N.A.	N.A.	A
57400	2.480	0.092	4.944	15.8	4.33	1.32	0.046	0.029	2.1	YES	7422 ± 20	5.93 ± 0.20	3.23	Cgh
57442	2.446	0.086	5.054	14.9	7.01	2.20	0.037	0.013	0.1	NO	–	1.49 ± 0.19	3.31	C
57473*	2.439	0.088	5.066	15.5	4.20	0.07	0.030	0.004	2.1	NO*	–	1.80 ± 0.08	1.88	X
58240	2.484	0.090	4.887	15.3	4.87	0.04	0.038	0.005	0.1	YES	7144 ± 7	2.76 ± 0.04	0.78	Ch
59065	2.446	0.091	5.016	14.9	6.58	2.01	0.045	0.027	1.6	NO	–	0.83 ± 0.06	1.30	C
60852	2.483	0.091	5.110	15.4	–	–	–	–	0.7	NO	–	1.30 ± 0.13	3.03	C
63310	2.478	0.093	5.261	15.3	–	–	–	–	N.A.	N.A.	N.A.	N.A.	N.A.	V
66421	2.436	0.092	5.225	15.2	5.35	0.32	0.052	0.016	2.7	YES	7304 ± 23	1.34 ± 0.05	0.92	X
67586	2.448	0.090	5.001	14.5	6.00	0.13	0.065	0.016	4.6	NO	–	1.13 ± 0.08	1.59	X
69679	2.446	0.090	4.956	15.8	–	–	–	–	2.0	YES	7008 ± 8	2.25 ± 0.07	1.60	X
70528	2.405	0.088	5.312	14.6	2.43	0.27	0.359	0.036	N.A.	N.A.	N.A.	N.A.	N.A.	V
72169*	2.458	0.091	5.015	15.5	–	–	–	–	1.3	YES*	7229 ± 10	2.15 ± 0.10	2.20	Cgh
73205	2.488	0.091	5.127	15.4	4.27	0.16	0.061	0.015	–0.5	YES	7307 ± 15	3.60 ± 0.10	2.01	Ch
77278	2.448	0.091	5.087	15.0	5.62	1.46	0.049	0.022	0.5	YES	7205 ± 6	2.74 ± 0.04	0.70	Cgh
79143	2.487	0.091	5.303	14.2	3.90	0.25	0.242	0.055	N.A.	N.A.	N.A.	N.A.	N.A.	V
79610	2.446	0.091	5.034	15.5	–	–	–	–	0.4	YES	7240 ± 9	1.82 ± 0.07	1.37	Cgh
81010	2.441	0.091	4.871	16.0	–	–	–	–	N.A.	N.A.	N.A.	N.A.	N.A.	A
84211	2.418	0.094	5.055	15.9	–	–	–	–	N.A.	N.A.	N.A.	N.A.	N.A.	Sr
84536	2.444	0.089	4.982	15.6	–	–	–	–	0.8	NO	–	0.91 ± 0.12	3.55	C
96690	2.440	0.091	5.055	15.7	3.92	0.14	0.060	0.014	1.4	YES	7113 ± 7	1.39 ± 0.03	0.71	Cgh
98391	2.436	0.084	4.993	15.4	4.64	0.19	0.040	0.009	1.3	YES	7158 ± 8	2.25 ± 0.05	1.08	Cgh
108631	2.445	0.092	4.979	15.4	–	–	–	–	2.0	YES	7040 ± 10	1.49 ± 0.05	1.16	X
109019	2.475	0.090	5.111	15.6	4.81	1.20	0.040	0.031	8.3	YES	7061 ± 11	5.49 ± 0.08	1.88	T
113374	2.419	0.091	5.103	16.0	–	–	–	–	1.6	YES	6742 ± 14	2.42 ± 0.17	1.16	Cgh
114308	2.439	0.087	4.904	15.7	–	–	–	–	1.2	NO	–	2.02 ± 0.22	4.01	C
116717	2.460	0.093	4.969	16.2	–	–	–	–	1.3	YES	6795 ± 12	4.03 ± 0.11	2.47	Cgh
119526	2.481	0.092	5.171	15.3	4.76	0.16	0.054	0.010	5.7	NO	–	1.50 ± 0.19	4.05	T
122109	2.434	0.088	4.940	16.2	3.08	0.32	0.051	0.037	–1.6	YES	7143 ± 18	5.28 ± 0.14	3.11	B
122871	2.441	0.091	5.142	15.0	4.82	0.13	0.070	0.010	1.3	YES	7126 ± 7	1.06 ± 0.03	0.74	Cgh
142297	2.440	0.087	5.001	16.0	3.55	0.35	0.051	0.017	5.3	NO	–	1.92 ± 0.17	4.22	T
147241	2.449	0.091	5.059	15.7	–	–	–	–	1.0	YES	7165 ± 6	2.56 ± 0.06	1.33	Cgh
147777	2.457	0.091	4.990	16.1	–	–	–	–	3.1	NO	–	–1.18 ± 0.14	3.97	Xe
148658	2.429	0.088	5.110	16.2	3.02	0.47	0.064	0.039	0.5	NO	–	1.56 ± 0.10	2.16	C
149396	2.440	0.087	4.851	16.0	3.19	0.59	0.063	0.036	1.4	NO	–	3.54 ± 0.20	4.69	C

Notes. We also include a summary of the obtained results for the primitive asteroids in our sample: slope values and aqueous alteration band analysis. We include taxonomical classification for all the observed asteroids, derived through the M4AST tool, based on Bus & Binzel (2002).
[(1)] Observed with INT.

A&A 610, A25 (2018)

Table B.2. continued.

Object	a (AU)	e	i (°)	H_V (km)	D (km)	err$_D$	p_V	err$_{pV}$	Slope (±0.8%/1000 Å)	Band	Center (Å)	Depth (%)	Residual	Class
151019	2.484	0.095	5.337	15.3	3.87	0.12	0.089	0.009	1.1	YES	6803 ± 29	4.66 ± 0.18	3.84	C
155162*	2.430	0.091	5.016	15.8	3.70	0.30	0.062	0.018	0.3	NO*	–	2.77 ± 0.13	2.67	Ch
162755	2.421	0.091	4.880	16.4	3.38	0.85	0.038	0.020	2.4	NO	–	1.06 ± 0.06	1.47	X
164286	2.455	0.091	5.079	15.8	3.15	0.37	0.093	0.033	1.1	NO	–	1.72 ± 0.10	2.53	C
203141	2.435	0.088	4.972	15.9	3.30	0.50	0.071	0.013	1.6	YES	7249 ± 10	3.26 ± 0.09	1.88	Cgh
262642*	2.431	0.088	5.041	16.9	–	–	–	–	–0.2	YES*	7023 ± 12	2.86 ± 0.15	2.83	Cgh
Clarissa														
302	2.406	0.106	3.346	11.0	29.48	9.07	0.062	0.045	0.7	NO	–	–0.93 ± 0.02	0.52	C
36286	2.395	0.104	3.304	15.5	4.20	0.30	0.063	0.014	–0.1	NO	–	–0.52 ± 0.02	0.84	C
41746	2.404	0.106	3.361	15.0	5.03	0.06	0.070	0.015	–1.5	NO	–	–0.76 ± 0.03	0.82	B
78921	2.403	0.107	3.398	15.8	2.85	0.99	0.084	0.040	4.1	NO	–	–0.48 ± 0.15	3.97	X
92634	2.400	0.107	3.413	16.1	3.12	1.10	0.067	0.045	0.7	NO	–	0.54 ± 0.08	2.97	C
98178	2.402	0.106	3.308	15.2	4.49	0.56	0.063	0.018	–2.4	NO	–	0.89 ± 0.07	1.85	B
99691	2.400	0.106	3.313	15.9	2.65	0.16	0.100	0.041	–1.3	YES	6760 ± 21	3.32 ± 0.30	2.59	B
106918	2.395	0.110	3.236	16.2	–	–	–	–	–1.1	NO	–	–1.35 ± 0.05	1.74	B
106919	2.401	0.107	3.429	16.0	4.18	0.48	0.040	0.008	1.1	YES	7401 ± 23	5.95 ± 0.25	3.78	Cgh
112414*	2.387	0.108	3.306	16.2	2.52	0.44	0.084	0.034	0.3	NO*	–	2.18 ± 0.16	2.14	C
132248	2.400	0.105	3.373	15.6	3.73	0.28	0.073	0.024	2.5	NO	–	1.48 ± 0.08	1.74	X
142751	2.400	0.105	3.412	17.1	–	–	–	–	–0.5	NO	–	–2.16 ± 0.62	2.60	C
168936	2.414	0.106	3.331	16.0	3.00	0.89	0.071	0.065	1.7	NO	–	0.84 ± 0.27	2.71	C
171027	2.412	0.106	3.346	16.8	4.58	0.45	0.013	0.003	–1.4	NO	–	0.21 ± 0.05	1.16	B
172478	2.412	0.107	3.381	16.8	–	–	–	–	–1.4	NO	–	1.32 ± 0.09	2.47	B
173657	2.399	0.107	3.362	16.9	–	–	–	–	2.0	NO	–	1.21 ± 0.20	3.31	C
180349	2.396	0.109	3.343	17.0	–	–	–	–	–0.3	NO	–	–0.09 ± 0.12	3.07	C
183911	2.391	0.109	3.478	16.0	–	–	–	–	3.5	NO	–	0.70 ± 0.10	2.05	X
186530	2.399	0.105	3.343	16.1	–	–	–	–	–3.2	NO	–	–0.42 ± 0.04	1.94	B
203620	2.399	0.106	3.369	16.2	2.12	0.34	0.119	0.044	0.7	NO	–	0.75 ± 0.15	3.62	C
206344	2.404	0.106	3.326	16.9	2.55	0.75	0.050	0.044	–4.4	NO	–	0.25 ± 0.09	2.56	B
208724	2.411	0.106	3.348	17.0	–	–	–	–	2.8	NO	–	–0.56 ± 0.06	2.02	X
217593	2.396	0.109	3.521	17.1	–	–	–	–	–0.6	NO	–	0.78 ± 0.07	1.98	C
237295	2.402	0.107	3.403	16.6	3.00	0.98	0.045	0.027	1.7	NO	–	1.08 ± 0.13	4.01	C
238992	2.396	0.109	3.431	16.6	3.24	0.23	0.042	0.005	0.5	NO	–	0.23 ± 0.09	2.77	C
242858	2.391	0.107	3.433	17.6	–	–	–	–	N.A.	N.A.	N.A.	N.A.	N.A.	V
246226*	2.395	0.109	3.394	17.2	–	–	–	–	–2.3	NO*	–	4.72 ± 0.21	4.72	B
249427	2.415	0.106	3.319	16.8	2.19	0.52	0.070	0.024	1.0	NO	–	2.83 ± 0.30	4.14	C
255959	2.400	0.106	3.347	16.8	–	–	–	–	4.7	NO	–	0.11 ± 0.32	4.03	X
300289	2.399	0.105	3.308	17.2	–	–	–	–	0.0	NO	–	0.05 ± 0.39	3.67	C
304858	2.400	0.106	3.376	16.8	–	–	–	–	0.8	NO	–	–0.20 ± 0.08	1.99	C
320575	2.398	0.108	3.373	17.0	2.69	0.48	0.039	0.016	–0.6	NO	–	1.02 ± 0.08	2.21	B
325852	2.396	0.108	3.371	17.9	–	–	–	–	–2.6	YES	7210 ± 17	1.60 ± 0.07	1.37	B

Chapter 6

Color study of asteroid families within the MOVIS catalog

In the third paper of this thesis we used the near-infrared colors of the MOVIS-C catalog in order to study the compositional diversity of collisional families in the main belt. This catalog was created extracting the near-infrared data of asteroids present in the VISTA-VHS all-sky survey. Using the color information available in the MOVIS catalog, we created a near-infrared parameter which allowed us to separate families into different classes according to their surface compositions. The initial goal of this study was the confirmation of primitive families in order to characterize possible sources of primitive near-Earth asteroids through the whole main belt. However, we decided to take advantage of the parametrization method that we developed, and we extended this characterization to all the families and their backgrounds (regardless of their composition) present in the MOVIS-C catalog. We also cross-checked the MOVIS information with the data present in the NEOWISE and SDSS databases to look for unusual traits in the analyzed families. In the last page of this chapter, we present the acceptance letter of this paper (Fig. 6.1).

Color study of asteroid families within the MOVIS catalog

David Morate[1,2], Javier Licandro[1,2], Marcel Popescu[1,2,3], and Julia de León[1,2]

[1] Instituto de Astrofísica de Canarias (IAC), C/Vía Láctea s/n, 38205 La Laguna, Tenerife, Spain
[2] Departamento de Astrofísica, Universidad de La Laguna, 38205 La Laguna, Tenerife, Spain
[3] Astronomical Institute of the Romanian Academy, 5 Cuţitul de Argint, 040557 Bucharest, Romania

April 20, 2018

ABSTRACT

The aim of this work is to study the compositional diversity of asteroid families based on their near-infrared colors, using the data within the MOVIS catalog. As of 2017, this catalog presents data for 53 436 asteroids observed in at least two near-infrared filters (*Y*, *J*, *H*, or *Ks*). Among these asteroids, we find information for 6299 belonging to collisional families with both $Y - J$ and $J - Ks$ colors defined. The work presented here complements the data from SDSS and NEOWISE, and allows a detailed description of the overall composition of asteroid families. We derived a near-infrared parameter, the ML^*, that allows us to distinguish between four generic compositions: two different primitive groups (P1 and P2), a rocky population, and basaltic asteroids. We conducted statistical tests comparing the families in the MOVIS catalog with the theoretical distributions derived from our ML^* in order to classify them according to the above-mentioned groups. We also studied the background populations in order to check how similar they are to their associated families. Finally, we used this parameter in combination with NEOWISE and SDSS to check for possible bimodalities in the data. We found 43 families with $ML^*_{err} < 0.071$ and with at least 8 asteroids observed: 5 classified as P1, 10 classified as P2, 19 families associated with the rocky population, and 9 families that were not linked to any of the previous populations. In these cases, we compared our samples with different combinations of these theoretical distributions to find the one that best fits the family data. We also show, using the data from MOVIS and NEOWISE, that the Bapistina family presents a two-cluster distribution in the near-infrared albedo vs. ML^* parameter space that might be related to a common differentiated parent body. Finally, we show that the backgrounds we defined seem to be linked to their associated families.

Key words. minor planets, asteroids: general - methods: data analysis - techniques: photometric

1. Introduction

Asteroid families are the remnants of catastrophic collisional episodes in the solar system. After such events, a large asteroid (commonly known as parent body) leaves behind dozens, hundreds, or even thousands of fragments that share similar orbital properties. These fragments, referred to as family members, experienced dynamical processes under the gravitational forces dominating the solar system and also via the Yarkovsky effect, gradually evolving to their current locations in the main asteroid belt (Bottke et al. 2002). By analyzing the physical properties of the family members, we can investigate the composition of the original bodies, and we can study the processes that these objects have experienced through the history of the solar system.

At the beginning of the 21st century, several all-sky surveys were carried out: SDSS (York et al. 2000) and Pan-STARRS (Kaiser et al. 2010) at optical wavelengths, and WISE (Wright et al. 2010), AKARI (Ishihara et al. 2010), and 2MASS (Skrutskie et al. 2006) at different infrared wavelengths. Initially, these surveys were mainly of cosmological or stellar interest. However, their sky coverage offers the opportunity to study a large number of solar system objects. Using data from some of these databases, combined with data from visible and infrared spectroscopic surveys, light curves, and polarimetry, Masiero et al. (2015) carried out an analysis of 109 out of the 122 families identified by Nesvorný et al. (2015). In their paper, they outlined some key questions that still remain unanswered, such as the effect of space weathering or the presence of inhomogeneities in asteroid family composition. Related to this last point, one of the most prominent questions is the apparent absence of collisional families generated from the complete disruption of a differentiated parent body.

In 2009, using the Visible and Infrared Survey Telescope for Astronomy (VISTA), several near-infrared surveys started to collect data in five broadband filters: *Z*, *Y*, *J*, *H*, and *Ks* (Sutherland et al. 2015). Among these, the VISTA Hemisphere Survey (VHS) aims to image almost the entire southern hemisphere, i.e., ∼19 000 degrees (McMahon et al. 2013). Using the third data release of this survey (VISTA VHS-DR3), Popescu et al. (2016) compiled their Moving Objects from VISTA Survey catalog (MOVIS), with a total of 39 947 solar system objects, including NEAs, main-belt asteroids, TNOs, comets, and other bodies. This catalog presents colors for those objects observed in at least two of the *Y*, *J*, *H*, and *Ks* infrared filters. See Fig. 1 for the response curves of these filters.

The work presented here aims to enhance the current knowledge about overall family composition and physical properties, and to complement the available information of the families with near-infrared photometry. To achieve this, we have used the latest version of the MOVIS database. This paper is organized as follows: we describe the latest version of the MOVIS catalog in Sect. 2, as well as the datasets used for family identification and data comparison; in Sect. 3 we define a near-infrared parameter that will be used to classify those families with a significant number of members observed within the catalog; in Sect. 4 we discuss the results for individual families; finally, in Sect. 5 we summarize the obtained results and we address some important questions to be investigated in the near future.

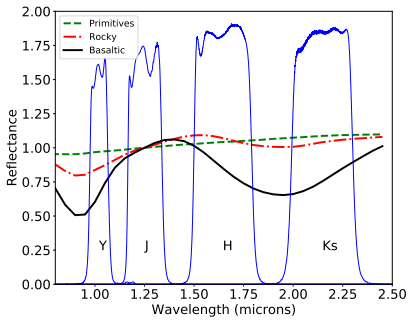

Fig. 1: Response curves of the Y, J, H, and Ks VISTA filters (blue), together with the DeMeo et al. (2009) template spectra of the asteroid populations in our study. We averaged the templates for the B-, C-, and X-types and subclasses (primitives); the S-types and subclasses (rocky); and V-types (basaltic). The template spectra have been normalized to unity at 1.25 μm (central wavelength of the J filter) for representation purposes.

2. Dataset description

To conduct our analysis we used several databases with physical data of thousands of asteroids. Here follows a brief description of each of these datasets.

2.1. Infrared colors from the MOVIS catalog

The main dataset that we use throughout this paper is the latest version of the Moving Objects from VISTA Survey (MOVIS) catalog[1]. It was compiled from data in the VISTA Hemisphere Survey (VHS), obtained using the VISTA telescope, a 4m class telescope located at the ESO Cerro Paranal Observatory (Chile). Thanks to this survey, which aims to cover almost the whole sky of the southern hemisphere (McMahon et al. 2013), it was possible to retrieve spectro-photometric data in four near-infrared filters, Y, J, H, and Ks (see Fig.1 and Table 1), and also accurate astrometry, for a very large number of solar system objects. A complete description of the creation of the MOVIS catalog can be found in Popescu et al. (2016). In particular, we use an updated version of the MOVIS-C catalog, compiled on April 30, 2017. This catalog was obtained using the VHSv20161007 data release of the VISTA Hemisphere Survey. It includes photometric colors ($Y-J$, $Y-H$, $Y-Ks$, $J-H$, $J-Ks$, and $H-Ks$) and errors for a total of 53 436 asteroids. Our analysis is performed using data in the Y, J, and Ks filters for a total of 18 263 objects. Figure 2 shows the distribution of these objects in proper orbital element space.

[1] The published version of the catalog can be found at http://vizier.u-strasbg.fr/viz-bin/VizieR-3?-source=J/A%2bA/591/A115/movis-c

[2] Filter information available at http://casu.ast.cam.ac.uk/surveys-projects/vista/technical/filter-set

Table 1: Central wavelengths and passbands for the different filters used in the SDSS (Bessell 2005), VISTA-VHS [2], and NEOWISE (Jarrett et al. 2011) surveys.

Filter	Effective central wavelength (μm)	Width (μm)
SDSS		
u'	0.3596	0.057
g'	0.4639	0.128
r'	0.6122	0.115
i'	0.7439	0.123
z'	0.8896	0.107
VISTA-VHS		
Y	1.021	0.093
J	1.254	0.172
H	1.646	0.291
Ks	2.149	0.309
NEOWISE		
$W1$	3.3526	0.66256
$W2$	4.6028	1.0423
$W3$	11.5608	5.5069
$W4$	22.0883	4.1013

2.2. Family lists

In order to look for family members within the objects present in the MOVIS catalog, we used the lists from Nesvorný et al. (2015). For the family identification process the authors took into account many past publications (Mothé-Diniz et al. 2005; Nesvorný et al. 2005; Gil-Hutton 2006; Parker et al. 2008; Nesvorny 2010, 2012; Novaković et al. 2011; Brož et al. 2013; Masiero et al. 2011, 2013; Carruba et al. 2013; Milani et al. 2014), as well as data from SDSS and NEOWISE, to finally define 122 asteroid families. These lists were created using numerically computed proper orbital elements for 384 337 numbered asteroids and 4016 Jupiter trojans. The dataset, publicly available in the Small Bodies Node of the NASA Planetary Data System[3], provides the synthetic proper orbital elements used to compute family membership, as well as values for the absolute magnitude of the asteroids (H_v). Some asteroids are included in more than one family; for example, all the members of the Beagle family are also included in the Themis family. In these cases we considered those asteroids as members of the smallest family (i.e., we removed the Beagle family members from the Themis family). We found 6299 asteroids belonging to 104 families among the MOVIS data and observed at least in the Y, J, and Ks filters (see Table A). These asteroids are shown in Fig. 2.

2.3. Other datasets: the SDSS MOC and NEOWISE

The Sloan Digital Sky Survey was initially devised to measure redshifts of large samples of galaxies (York et al. 2000; Ivezić et al. 2001). However, sky coverage and survey operations made it possible to observe a great number of asteroids in five photometric filters (u', g', r', i', z') in optical wavelengths (see Table 1). The latest release of the Sloan Digital Sky Survey Moving Object Catalog (SDSS MOC) lists astrometric and photometric data for 471 569 moving objects observed up to March 2007. This catalog has been used to determine family membership (Ivezić et al. 2002), to constrain family size distribution (Parker et al.

[3] https://pds.nasa.gov/

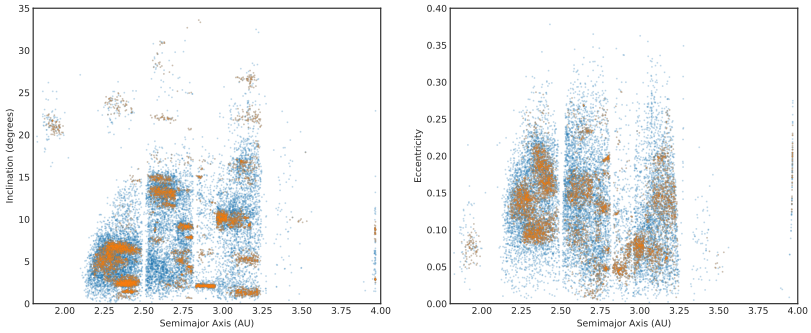

Fig. 2: Proper semimajor axis vs. proper inclination (left panel) and proper eccentricity (right panel) for the asteroids observed within MOVIS catalog. The blue background represents the full sample of objects with $Y-J$ and $J-Ks$ colors defined in MOVIS (a total of 18 263 objects). In orange, we overplot those asteroids belonging to families (6299 objects).

2008), or even to perform photometric taxonomic classifications (Carvano et al. 2010; DeMeo & Carry 2013).

In a different wavelength range, the Near-Earth Object Wide-field Infrared Survey Explorer (NEOWISE, initially launched as WISE) performed an all-sky astronomical survey with images in four infrared photometric filters (see Table 1). This catalog contains data for over 150 000 asteroids (Mainzer et al. 2011, 2014). Using this dataset, Masiero et al. (2011) computed albedos and diameters for over 32 000 members of 46 collisional families from Nesvorny (2012), and from these diameters Masiero et al. (2013) measured the size-frequency distributions for 76 asteroid families identified within the data.

In this work we compare near-infrared albedos (p_{NIR}) derived from the NEOWISE[4] data, and the slope parameter a^* derived from the SDSS[5] observations, with the results obtained from our analysis of the MOVIS near-infrared colors (which covers the wavelength range between the SDSS and NEOWISE surveys) of the families present in the catalog.

3. Data processing

In order to differentiate between the asteroid populations in the MOVIS catalog, we define a single parameter (ML^*) using the Y, J, and Ks spectro-photometric information. We followed a similar approach to that used in Ivezić et al. (2001) to derive the a^*. We chose this parametrization because it favors the description of overall composition of asteroid groups. An in-depth taxonomic classification based on near-infrared colors and obtained with a machine-learning algorithm is presented in Popescu et al. (2018). This taxonomy favors the classification of individual asteroids into several classes and subclasses, and it is compatible with previous taxonomies, proposing targets for future spectral investigation.

[4] https://sbn.psi.edu/pds/resource/neowisediam.html
[5] SDSS MOC4: http://faculty.washington.edu/ivezic/sdssmoc/sdssmoc.html

3.1. The ML* parameter

We parametrized the photometry of the asteroids in the MOVIS database in order to determine how families are compatible with a "primitive" or "rocky" composition. This process followed four steps:

1. We first removed the ten observed comets from the full MOVIS-C database. Then, taking into account our previous experience with data quality when creating the MOVIS catalog, we selected the subset of asteroids with computed colors $Y-J$ and $J-Ks$ having errors smaller than 0.15 magnitudes ($C_{0.15}$). This yielded a total of 10 107 objects.

2. We performed two bivariate kernel density estimations on this first selection with different resolutions using Python routines contained in the *seaborn* package (Waskom et al. 2017). Once we estimated the bivariate probability density functions (PDF), we extracted the values of the density maxima for the two main clusters present in the color-color plots, associated with S- and C-complex asteroids (Popescu et al. 2016).

3. We then computed the angle between the line that connects the two maxima (determined in the previous step) and the x-axis of the system. Next, we rotated the system according to this angle, selecting the new y-axis as our parameter.

4. We forced this parameter to be zero at the separation between the two main clusters. To do this, we performed a new, unidimensional, PDF estimation, and we computed the required offset selecting the point of minimum density between the two peaks of this univariate PDF.

To test whether the data quality is relevant in the previous process, we repeated these four steps selecting a new subset by limiting the error in the color determination to 0.10 magnitudes ($C_{0.10}$). Figure 3 shows a graphical representation of this procedure. After this, we averaged the rotation angles of the system

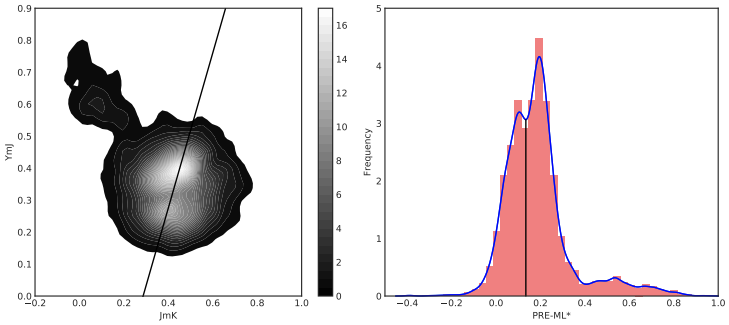

Fig. 3: Graphical representation of the procedure followed to parametrize the near-infrared colors in MOVIS. The left panel shows the kernel density estimation plot of the $J - Ks$ (JmK) vs. $Y - J$ (YmJ) distributions. Brighter regions correspond to higher density of points. The straight line connects the two main cluster centers (peaks of maximum density). The third cluster ($Y - J > 0.5$) corresponds to basaltic asteroids (Popescu et al. 2016). The right panel shows the univariate PDF estimation for the ML^* before the computation of the required offset to set the separation between the rocky and primitive asteroids clusters at the origin. The vertical black line indicates the point where the PDF density is minimum between the two maxima. We used the $C_{0.10}$ subset for this example.

and the computed offsets obtained for the $C_{0.10}$ and $C_{0.15}$ subsets in order to build our parameter, ML^*, defined as follows:

$$ML^* = 0.931(Y - J) - 0.364(J - Ks) - 0.142 \quad (1)$$

This definition is almost coincident with Equation 3 from (Popescu et al. 2016) for the case where $ML^* = 0$.

The uncertainties associated with the ML^* parameter are obtained by propagating the color errors. We note that the fact that the observations are not simultaneous might introduce also some uncertainty related to light curve variations. The mean time interval between the two measurements used to compute the colors (Y–J) and (J–Ks) is $t_{(Y-J)} = 7.6 \pm 2.4$ min, and $t_{(J-Ks)} = 7.9 \pm 3.7$ min, respectively (Popescu et al. 2016). The magnitude variation during this interval can be estimated by considering the light curves reported by the Asteroid Lightcurve Database[6]. The median rotation period for more than 18 000 asteroids is ~ 6.3 h, and the median of the light curve amplitudes is ~ 0.38 magnitudes. Thus, for a lightcurve amplitude of 0.38 magnitudes with a 6.3 h period, and 7.75 min between the observations, we estimate an uncertainty of ~0.03 magnitudes in (Y–J) and (J–Ks), and subsequently in ML^*, due to light curve variations. As is described in Sect. 4.1, we consider for our analysis the subset of asteroids with $ML^*_{err} < 0.071$. Thus, we are already taking into account possible light curve induced errors, i.e., these do not affect the outcome of the analyses.

After obtaining this parameter, we computed theoretical distributions of ML^* for the different clusters present in the sample in order to separate the contributions of the different identified populations. In Popescu et al. (2016), the authors identified three regions in the J–Ks vs. Y–J color-color plots, associated with C/X-complex, S-complex, and V-type asteroids. In good agreement with this result, we identify the same three groups in our ML^* distribution, shown in the left panel of Fig. 4: primitives (green stars), rocky (blue dashed line), and basaltic (black crosses). We used standard curve-fitting Python routines inside the *lmfit* module (Newville et al. 2014) to compute the best fit for our ML^* distribution, using a combination of these three contributions (red line in Fig. 4).

Our first approach was to use a combination of three Gaussians to fit the ML^* distribution. However, the fitting routine did not converge on its own, and we needed to "force" it to fit the three distributions to the data (Appendix B, left panels). The results pointed to the possibility of obtaining a better fit, so we tried a combination of three Lorentzians and achieved better results (Appendix B, center panels). By looking at these plots, we can see that for $ML^* < 0$ (the primitive region) the Gaussian function gave a better approximation to the data, while the regions corresponding to $ML^* > 0$ (associated with rocky and basaltic populations) were better fitted by Lorentzians. Thus, we used a combination (Appendix B, right panels), which provided the best fit of the three cases. This behavior might be explained by the fact that primitive asteroid spectra are almost featureless, meaning that their color variation will be smaller than the color variations associated with rocky or basaltic asteroids, whose spectra present deep absorption bands in the near-infrared region, which would account for the higher dispersion in the wings of their corresponding distributions.

After preliminary analyses on our data using this three-distribution fit, we found some discrepancies when running KS-tests for the families. Whereas the rocky distribution accurately fit the family data in the corresponding cases, the primitive distribution did not match (according to the KS-tests) some families previously known as primitive, for example Hygiea or Themis, and there was no combination of distributions that we could use to accurately fit the data (see Appendix B, Fig. B.3). At this point, we decided to consider an extra primitive distribution in the fitting routine, taking into account the mean ML^* values ob-

[6] http://www.minorplanet.info/lightcurvedatabase.html

Table 2: Mean ML^* values computed for the four different populations detected within the ML^* distribution.

Cluster	$\overline{ML^*}$	σ_{ML^*}
P1	-0.092	0.029
P2	-0.033	0.027
Rocky	0.063	0.042
Basaltic	0.407	0.062

tained for the Themis and Hygiea families. We note that this fit (Fig. 4, right panel) does not look significantly different from the three-population case, yet the KS-test that we ran to check for similarity tells us that the choice of four populations gives a slightly better fit than using three populations. In addition, when it comes to fitting these primitive families, the results are significantly better; as we show in Sections 4.1 and 4.2.5, using this approach, we were able to fit all of the families to one of the theoretical distributions that we defined (or a combination of them), something that we did not manage to do when using the three-population fit.

We thus obtained the best fit combination by assuming four different distributions (see Fig.4-right and Fig. B.2-right): two Gaussians for two primitive populations (denoted P1 and P2, associated with a combination of B-, C-, and X-types and subclasses), and two Lorentzians, one for a rocky population (associated with S-types and subclasses) and one for a basaltic population (associated with V-types). The near-infrared spectra of these groups is represented in Fig. 1, averaged for the primitive and rocky populations. We use this information to differentiate between the families present in the MOVIS database.

We applied the parametrization obtained in this section to the 6299 objects belonging to 104 collisional families among the MOVIS database, as described in Sect. 2.2. The mean ML^* values for each of these families and their corresponding errors are shown in Table A.1.

3.2. Connecting SDSS MOC and NEOWISE to MOVIS

In addition to the analysis performed on the MOVIS data alone, we combined our near-infrared parameter with the near-infrared albedos, p_{NIR} (albedos for the W1 bandpass, at 3.4 μm) computed from NEOWISE data (Masiero et al. 2014), and with the a^* colors from SDSS (Ivezić et al. 2001). Since we are working with near-infrared data, we have selected the p_{NIR} instead of the p_V for comparison. In addition, the p_{NIR} provides a larger separation for the identified clusters (see Fig. 5). Also, according to Masiero et al. (2014), these near-infrared albedos are a more precise indicator of the surface properties than the visible albedos.

To combine our ML^* with the near-infrared albedos from NEOWISE (or the a^* from SDSS), we have represented the data as weighted density plots. These plots are done by considering that every data point for ML^* and p_{NIR} (or a^*) defines a bi-dimensional Gaussian distribution, where the mean is equal to the measured value, and the sigma is the error associated with that measurement. The total density is given by the sum of all the Gaussians. The density peaks correspond to the highest probabilities of finding an object inside this two-dimensional space.

In Fig. 6 we present the weighted density plots for all the asteroids in the MOVIS database that have computed values of ML^* and p_{NIR} (or a^*). Separate clusters, as well as the transition regions between them, are clearly seen in these plots. We have overplotted (in white) the mean ML^* and p_{NIR} (or a^*) values for the collisional families having more than 200 members with MOVIS data: Vesta, Flora, Eunomia, Themis, Nysa–Polana, Koronis, and Eos.

Several families of those represented in Fig. 6 have been widely studied, and their properties and overall characteristics are accurately known. For example, Binzel & Xu (1993) confirmed the collisional origin of the Vesta family by means of spectroscopy, finding spectral features similar to those of (4) Vesta among their sample; Florczak et al. (1998) performed spectroscopic observations of several objects in the Flora family, and almost all of them showed a maximum around 0.75 μm, typical of S-type (rocky) asteroids; Florczak et al. (1999) observed asteroids from the Themis family and determined that most of them have featureless spectra, with their distribution contained in the range of the taxonomic classes that we refer to as primitive; several studies of the Eos family (Doressoundiram et al. 1998; Vokrouhlický et al. 2006; Mothé-Diniz et al. 2008; Masiero et al. 2014) show that it presents traits that are somehow exclusive to it, with a considerable number of Eos family members associated with a particular spectroscopic class, the K-types. We take advantage of our current knowledge of these and other notable families in order to compare the results obtained from MOVIS with those of SDSS and NEOWISE, and with the rest of the detected families.

We draw weighted density plots of ML^* vs. p_{NIR} or a^* for families that have data available for at least 40 members (i.e., the analyzed families should have ML^* and p_{NIR} or a^* determined for at least 40 asteroids). We consider that using a smaller number of objects will lower the statistical significance of the results. These plots are shown in Appendix C, and the most relevant results are discussed in the following sections.

4. Results and discussion

There are a total of 104 collisional families with at least one member with determined ML^* in the MOVIS catalog. In the following subsections we present the ML^* distribution for 43 families detected in the MOVIS catalog, and for 27 of them, we also show the distributions of their associated backgrounds (see Sect. 4.3 for the definition of background). In addition, out of the 104 families, 17 of them present at least 40 asteroids that also have NEOWISE data, and 12 out of these 17 have at least 40 asteroids coincident with the SDSS MOC. We individually discuss some of them in the following sections.

4.1. The ML^* distribution for the families in MOVIS

We compared the ML^* distributions of the asteroid families present in the MOVIS database to the theoretical distributions computed in Sect. 3.1. The most efficient way to do this is through a Kolmogorov–Smirnov test (KS-test), since it is designed to compare samples of unidimensional probability distributions against a reference distribution (or against another sample). In addition, the KS-test works very well with a surprisingly small number of points in the sample (Stephens 1970).

The KS-test takes the cumulative distribution function (CDF) of the sample we want to compare (in our case, the ML^* distribution of the family) and computes the maximum distance between this CDF and that of the reference distribution (the theoretical distributions that we computed). The test works under the initial hypothesis that the sample is drawn from the reference distribution. It is designed to reject this hypothesis whenever the maximum distance between the sample CDF and the reference CDF is higher than some critical value. It is important to note that fail-

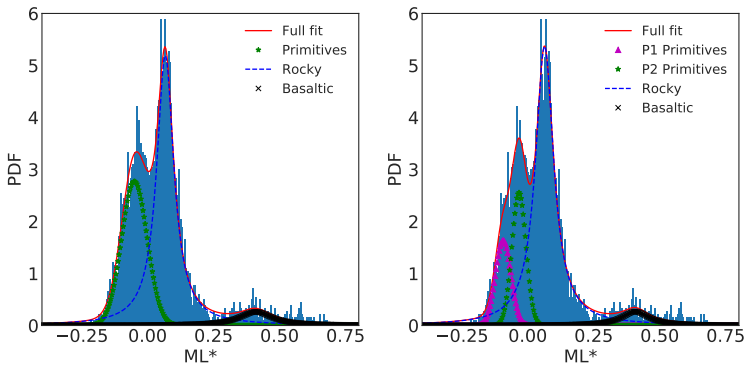

Fig. 4: Histograms and fits for the ML^* distribution. We have used only those objects presenting an error in the computation of ML^* smaller than the first quartile of the full sample ($ML^*_{err} < 0.0408$). A total of 4566 objects were used for these fits. In the left panel we show the fitting results for the case with only three distributions (primitive, rocky, and basaltic). The right plot shows the fitting results when we introduce an additional primitive population. This last case provides the best fit. The red line corresponds to the combination of all the populations used for the fits. See Table 2 for the computed mean ML^* values and their corresponding standard deviations for these four groups. We note that for the P1 and P2 populations $ML^* < 0$, while for the rocky and basaltic populations $ML^* > 0$.

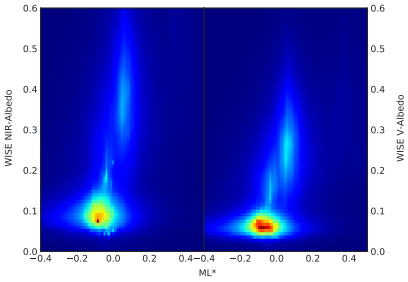

Fig. 5: Weighted density plots of the NEOWISE near-infrared (left) and visible (right) albedos vs. ML^*. The cluster associated with rocky populations (ML^*>0) is more separated from the primitive cluster (ML^*<0) in the case of the near-infrared albedo, providing a better visual differentiation.

ing to reject it does not confirm the initial hypothesis, but the test gives a good idea of how similar the two distributions are.

According to Stephens (1970), the KS-test serves a practical purpose for samples with $N_{OBS} \geq 8$. Therefore, we ran this test for all the families in the MOVIS catalog that have at least eight members and an error in the determination of ML^* smaller than the first quartile of the full family sample (i.e., $ML^*_{err} < 0.071$). In Fig. 7 we present a graphical representation of the KS-test performed for the 43 families that fulfilled the previous requirements.

The results yielded rejections (with a confidence level of $\alpha = 0.01$, i.e., around 2.5σ) in all the cases for three of the four theoretical distributions that we proposed, except for nine families for which all the proposed distributions were rejected: Vesta, Hygiea, Themis, Nysa–Polana, Hilda, Erigone, Ino, Eos, and Ursula. For these families, we studied possible mixtures of the four distributions. These "theoretical" mixtures were created by generating random numbers according to two (or more) of the computed distributions, up to the desired percentages (i.e., in a 25–75% P2–rocky mixture, 25% of the sample is generated according to a P2 distribution, and the other 75% is generated according to a rocky distribution).

Among the rest of the analyzed families, 5 of them are compatible with the P1 population, 10 are compatible with a P2 population, and 19 are compatible with our rocky distribution (see Table 3).

According to these results, we are able to characterize a family as belonging to one of the four proposed distributions by rejecting the other three. In other words, the result of the test gives an idea of how homogeneous a family is. It is interesting to note that the four distributions are rejected for some of the cases where the number of objects is high: for example, the Vesta family, with 408 objects in the analyzed distribution, known to be composed of basaltic asteroids, is rejected by this test as a 100% basaltic population. This tells us that when we have enough data, we are able to distinguish inhomogeneities in the family distributions. We discuss some of these cases in Sect. 4.2.

4.2. Individual families

4.2.1. Vesta (and Ino)

The Vesta family is one of the best known asteroid families, closely related to one of the largest asteroids within the solar sys-

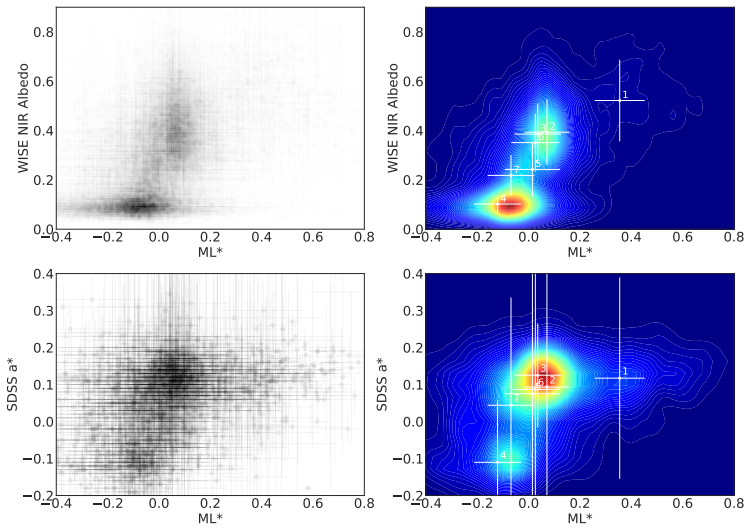

Fig. 6: Top: Scatter plot (left) and corresponding weighted density plot (right) of the computed ML^* from this work and near-infrared albedo values from NEOWISE, for a total of 8746 objects. Bottom: Same as top panels, but for the computed a^* from SDSS MOC (2210 objects). Overplotted in white are the points (with their error bars) corresponding to the mean values of these parameters for some of the families observed within MOVIS: 1-Vesta, 2-Flora, 3-Eunomia, 4-Themis, 5-Nysa–Polana, 6-Koronis, 7-Eos.

tem, (4) Vesta. This family presents characteristic high albedos ($< p_{NIR} >= 0.52 \pm 0.17$), and is associated with the howardite-eucrite-diogenite (HED) meteorites (McCord et al. 1970; Binzel & Xu 1993; Moskovitz et al. 2010; Mayne et al. 2011).

As we mentioned in the previous section, the KS-test rejects the hypothesis that the Vesta family distribution comes from our theoretical basaltic population. According to Licandro et al. (2017), around 85% of the Vesta family members are V-types, and just 1–2% are classified as primitive objects. Using this information, we created new theoretical distributions by combining our basaltic, rocky, and primitive populations in different proportions. We then applied the KS-test to the ML^* distribution of the Vesta family and these new distributions, looking for the combination that minimized the KS-test result and that was not rejected. The best result was obtained with a combination of 93% basaltic population and 7% rocky–primitive populations, in good agreement with the values obtained by Licandro et al. (2017).

When we add NEOWISE (Fig. C.1a) or SDSS data (Fig. C.2a) to our ML^* parameter and create the corresponding weighted density plots, we can see that the Vesta family is unique, as we do not find this type of clustering in any of the other represented families. However, we can see in these plots the same behavior that we observed with just the analysis of the ML^* distribution: a small contamination of rocky objects, which might be part of the background in that region of the asteroid belt, and even primitive asteroids, probably interlopers from the small primitive background in the inner belt.

One interesting case to mention together with Vesta is the Ino family. This family's ML^* CDF (see Fig. 7), although constructed from a small number of objects (just 11), shows a behavior that is quite strange. The KS-test rejects compatibilities with any of the four proposed theoretical distributions, even with distributions created from combinations of P1-P2-rocky populations. However, considering that the KS-test results were smaller for the comparisons with the rocky and basaltic populations, we decided to create combinations of these two and compare the resulting distributions with the family distribution: we minimized the KS-statistic for a mixture of 60% rocky and 40% basaltic populations. Nevertheless, the test also finds compatibilities for mixed samples of 50–50% up to 73–27% rocky–basaltic populations. Interestingly, Licandro et al. (2017) found that two of the V-type asteroids identified in the central main belt, (180703) and (197480), belong to the Ino collisional family. Spectroscopic observations of a significant number of asteroids in this family would be needed in order to check whether it presents more basaltic asteroids or not.

4.2.2. Nysa–Polana and Erigone

Using photometric data from visible filters, Tedesco et al. (1982) proposed that the Nysa family (now known as the Nysa–Polana complex) presented asteroids with pronounced differences in

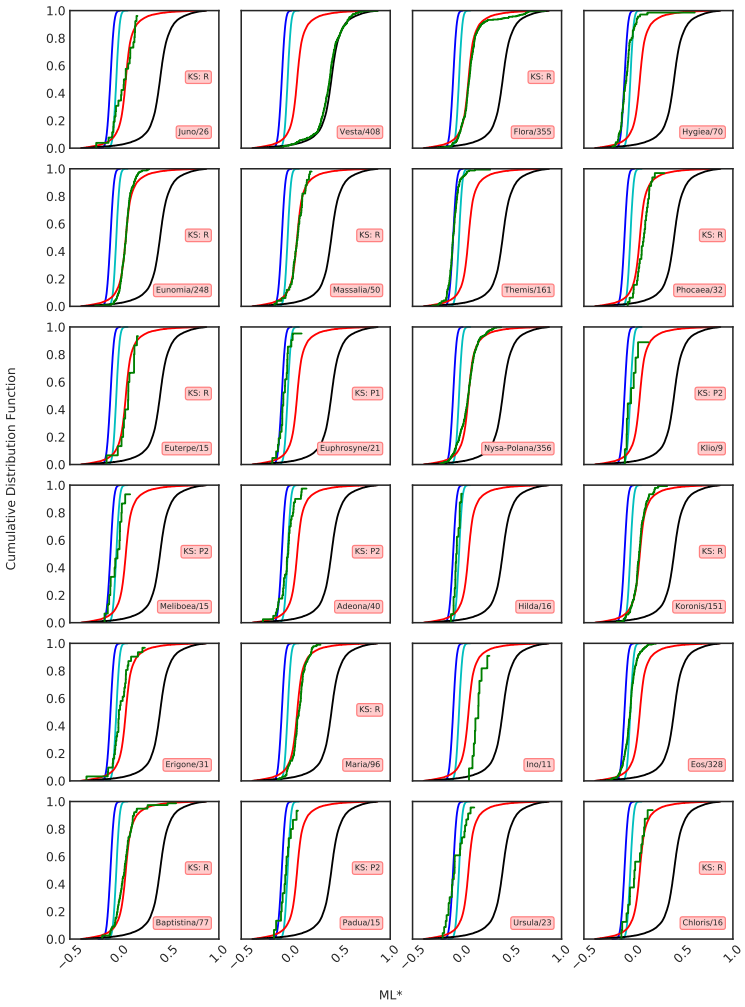

Fig. 7: Cumulative distribution functions (CDFs) for all the families with $N_{OBS} \geq 8$ observed in MOVIS and $ML^*_{err} < 0.071$ (green), together with the theoretical distributions computed in Sect. 3.1: dark blue for P1, light blue for P2, red for the rocky population, and black for the basaltic population. Each plot includes the family name and the number of asteroids from the family used to run the KS-test. In addition, we marked every family associated with a single population (determined via the KS-test).

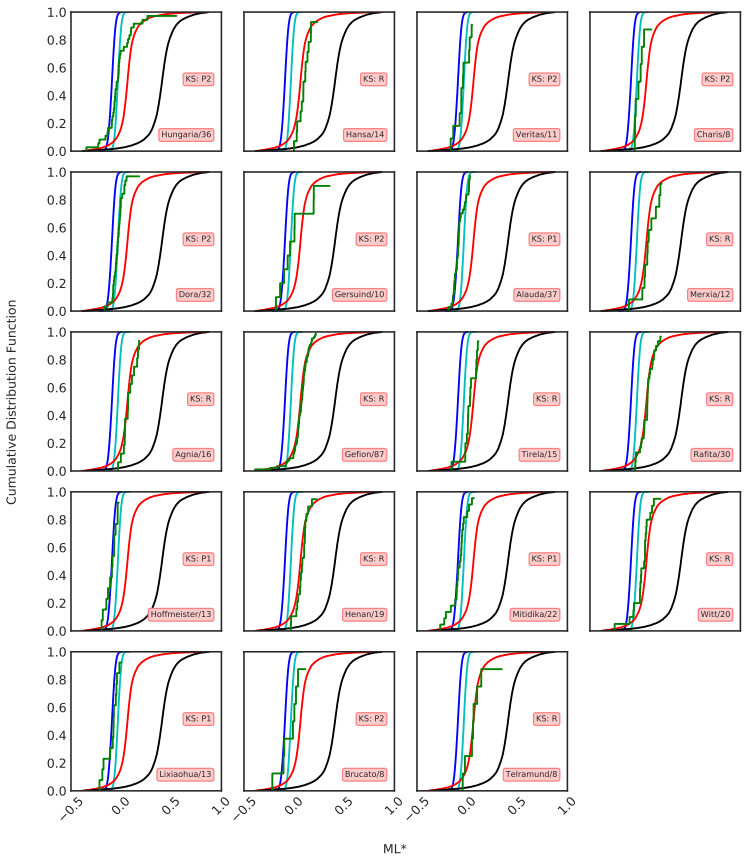

Fig. 7: Continued.

their colors, pointing to the idea of a differentiated parent body. Later, Cellino et al. (2001) presented visible spectra of 22 asteroid members of this family, finding evidence that this group was actually formed by two different clusters associated with asteroids (44) Nysa and (142) Polana, rather than being the result of the disruption of a common differentiated parent body. Subsequent studies have revealed the dynamical complexity of this particular region of the asteroid belt (Walsh et al. 2013; Milani et al. 2014; Dykhuis & Greenberg 2015).

The weighted density plot using ML^* and p_{NIR} from NEOWISE (see Fig. C.1f), shows two clearly separated clusters for the Nysa–Polana family. Although the ML^* CDF of the Nysa–Polana complex is visually very similar to that of our rocky population (see Fig. 7), the KS-test rejects the four proposed populations, i.e., the statistics tell us that the Nysa–Polana complex is not composed solely of rocky objects. Thus, after trying several mixtures of primitive and rocky distributions, the KS-test is minimized for a 90–10% mixed population of rocky–P2 objects. This result is in good agreement with the literature, since the whole Nysa–Polana complex is composed of approximately 20 000 asteroids, while the Polana family has around 2000 members.

Table 3: Results for the Kolmogorov–Smirnov test for all the families that have $N_{OBS} \geq 8$ with $ML^*_{err} < 0.071$. In the first two columns we specify the family name and the number of objects used for the KS-test. In columns three to six, D_{P1}, D_{P2}, D_{Rocky}, and $D_{Basaltic}$ are the maximum distances between the families and the theoretical CDFs. $D_{Critical}$ is the critical distance, i.e., if the distance resulting from the KS-test is greater than this value, the test rejects the compared distribution. In the last column we indicate which distribution (or mixture of distributions) was not rejected by the test.

Family	N_{OBS}	D_{P1}	D_{P2}	D_{Rocky}	$D_{Basaltic}$	$D_{Critical}$	Not Rejected
Juno	26	0.7385	0.6170	0.2062	0.9358	0.3110	Rocky
Vesta	408	0.9772	0.9650	0.8389	0.0980	0.0823	93% B - 7% R-P2
Flora	355	0.8880	0.7579	0.0666	0.8346	0.0880	Rocky
Hygiea	70	0.2916	0.4535	0.7087	0.9365	0.1955	67% P1 - 33% P2
Eunomia	248	0.9323	0.7838	0.0634	0.9051	0.1048	Rocky
Massalia	50	0.8759	0.7770	0.0817	0.9229	0.2311	Rocky
Themis	161	0.1312	0.5980	0.7976	0.9525	0.1295	95% P1 - 5% P2
Phocaea	32	0.9361	0.8374	0.2695	0.8897	0.2810	Rocky
Euterpe	15	0.9282	0.8423	0.2575	0.9332	0.4040	Rocky
Euphrosyne	21	0.3436	0.4674	0.7472	0.9567	0.3440	P1
Nysa–Polana	356	0.8004	0.6628	0.1146	0.8616	0.0879	90% R - 10% P2
Klio	9	0.6679	0.3448	0.5488	0.9454	0.5130	P2
Meliboea	15	0.5948	0.3530	0.6285	0.9570	0.4040	P2
Adeona	40	0.5966	0.2404	0.6048	0.9431	0.2582	P2
Hilda	16	0.5325	0.4029	0.8415	0.9752	0.3920	36% P1 - 64% P2
Koronis	151	0.8974	0.7497	0.0873	0.9003	0.1336	Rocky
Erigone	31	0.7493	0.4324	0.3854	0.8939	0.2850	44% P2 - 56% R
Maria	96	0.9113	0.8103	0.1521	0.8934	0.1672	Rocky
Ino	11	1.0000	0.9999	0.6572	0.8777	0.4680	60% R - 40% B
Eos	328	0.5572	0.1923	0.6223	0.9392	0.0915	25% P1 - 55% P2 - 20% R
Baptistina	77	0.8437	0.6243	0.1684	0.8855	0.1865	Rocky
Padua	15	0.5023	0.3008	0.6376	0.9641	0.4040	P2
Ursula	23	0.3834	0.5520	0.5813	0.9539	0.3300	49% P1 - 51% P2
Chloris	16	0.7190	0.5382	0.3498	0.9302	0.3920	Rocky
Hungaria	36	0.5016	0.2637	0.5695	0.8693	0.2722	P2
Hansa	14	0.9991	0.9141	0.3355	0.9105	0.4180	Rocky
Veritas	11	0.6058	0.3393	0.6136	0.9682	0.4680	P2
Charis	8	0.9108	0.4223	0.5550	0.9555	0.5420	P2
Dora	32	0.6218	0.1536	0.6551	0.9363	0.2810	P2
Gersuind	10	0.5623	0.4116	0.5214	0.8291	0.4890	P2
Alauda	37	0.2570	0.5974	0.7408	0.9716	0.2685	P1
Merxia	12	0.9166	0.8955	0.2241	0.9202	0.4500	Rocky
Agnia	16	0.9832	0.8627	0.1431	0.9357	0.3920	Rocky
Gefion	87	0.9061	0.7924	0.1096	0.9190	0.1755	Rocky
Tirela	15	0.9274	0.6728	0.3491	0.9553	0.4040	Rocky
Rafita	30	0.9304	0.7733	0.1739	0.9234	0.2900	Rocky
Hoffmeister	13	0.2401	0.5953	0.8789	0.9776	0.4320	P1
Henan	19	0.9783	0.8744	0.2071	0.9141	0.3610	Rocky
Mitidika	22	0.3313	0.4464	0.7119	0.9648	0.3370	P1
Witt	20	0.7990	0.6743	0.2881	0.9249	0.3520	Rocky
Lixiaohua	13	0.3160	0.5409	0.8301	0.9750	0.4320	P1
Brucato	8	0.6221	0.4111	0.5552	0.9554	0.5420	P2
Telramund	8	0.9522	0.7488	0.1340	0.8234	0.5420	Rocky

Another family that needs to be discussed here is Erigone. This family is classified as primitive. Masiero et al. (2015) computed visible and near-infrared albedos for ~50% of the members in the Erigone family, giving values compatible with this classification ($< p_V >= 0.05 \pm 0.01$ and $< p_{NIR} >= 0.06 \pm 0.01$). This is also evident from our weighted density plot of ML^* and p_{NIR} for the family (see Fig. C.1i). Interestingly, we find that the ML^* CDF of this family (computed with a total of 31 observations) falls in between the CDFs of the P2 and the rocky populations (see Fig. 7). When looking for the best-fitting mixed distribution, we found it for a combination of 44–56% P2–rocky populations (see Fig. 8). Morate et al. (2016) studied visible spectra of 103 members of the Erigone family, 14 of which did not have any albedo information, and 8 of which presented spectra compatible with the rocky population defined here. This translates into a percentage of approximately 57% of rocky interlopers contaminating the sample, most likely from the background, and is in good agreement with the fraction of rocky population we find as a best-fitting result of the family's CDF.

A possible explanation for these results might be that since family membership lists are based on optical magnitude, brighter objects are preferentially selected: NEOWISE has a flat sensitivity with respect to albedo, and will miss the small, higher albedo objects that are included in the family membership; conversely,

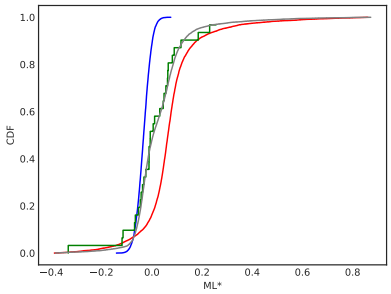

Fig. 8: Cumulative distribution function of the Erigone ML^* distribution (green). The P1 primitive and rocky theoretical distributions are depicted in blue and red, respectively, and the mixture in gray. It is easy to see that the Erigone CDF fails to follow any of them. However, the 44–56% mixture seems to accurately fit the family sample.

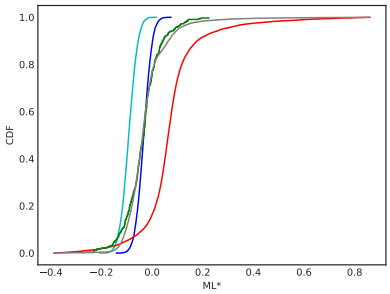

Fig. 9: Cumulative distribution function of the Eos ML^* distribution (green), compared to the P1 (cyan), P2 (blue), and rocky (red) theoretical distributions. The mixed distribution which minimizes the KS-test (in gray) follows the family curve almost exactly.

as MOVIS is based on reflected light, it will be preferentially sensitive to high albedo objects (because of the steep growth of the number of family members with decreasing diameter). This might suggest some physical evidence. However, we consider this 44–56% ratio as a preliminary finding, which should be addressed by spectroscopic surveys.

4.2.3. Eos

The Eos family is, in a certain way, as distinctive as Vesta; it is the only one in the whole main belt classified as a K-type. This has been shown by means of spectroscopic observations (Mothé-Diniz et al. 2005, 2008). In Masiero et al. (2014) it is also shown that the Eos family can be easily addressed by their characteristic 3.4 μm albedos.

There are a total of 599 asteroids from the Eos family in the MOVIS catalog. Of these, we used 328 for the analysis of the ML^* distribution. Visual inspection of the CDF of this family (see Fig. 7) tells us that it is different from our four proposed populations (and different from all the other families as well). This is confirmed by the KS-test, which rejects compatibility with all the theoretical distributions that we have defined in this work. When looking for an approximate composition of this family, we needed to combine the P1, P2, and rocky populations. We found the best fit for a 25-55-20% combination of these distributions (Fig. 9).

If we also use the near-infrared albedo from NEOWISE and the SDSS data, we are able to distinguish a different clustering from that of the rest of the families, located in what we call a transition region in the ML^* vs. p_{NIR} or a^* (see Fig. 6 and Figs. C.1k and C.2d). We identify this region with a K-type population, since Eos is the only family that shows this spread in the weighted density plots. Thus, the mixture we found as the best fit for the ML^* is equivalent to that of a K-type distribution.

Although the combination of the P2 and rocky distributions probably gives a result of a K-type population, there is still a non-negligible "contamination" of objects from a P1 distribution (we note that $ML^*_{P1} < ML^*_{P2}$). This is probably due to the family location in the outer belt where the proportion of primitive asteroids with negative slopes is higher than in the inner and middle regions.

4.2.4. Baptistina

The Baptistina family has been the object of various studies during the last years. Some investigations pointed to a C-type low albedo family, inferred from the spectra of (298) Baptistina and some of its members. Subsequent studies have shown that this is not a typical homogeneous family: Reddy et al. (2011) linked Baptistina to Vesta and Flora, both nearby families in the proper element space (Baptistina is actually contained within Flora). Using albedos or SDSS data to separate these families does not provide definitive results (Masiero et al. 2013).

The KS-test is unable to distinguish the Baptistina family from a rocky population (see Table 3). However, after combining the ML^* from MOVIS either with the p_{NIR} or the a^*, we are able to distinguish a two-cluster distribution for the Baptistina family (see Figs. C.1f and C.3g), different from the clustering present in the Flora family (see Figs. C.1b and C.2b). This kind of clustering might point to several scenarios: a fraction of the family may actually be composed of background asteroids; Baptistina may actually be formed of two different families, as is the case of the Nysa–Polana complex (Figs. C.1f and C.3g have cluster distributions similar to those in Figs. C.1f and C.2c); or this family may be the product of the breakup of a differentiated parent body.

Even if the KS-test failed to differentiate the Baptistina family CDF from that of a rocky family, after identifying this bimodality in the weighted density plots, we compared it to different combinations of primitive and rocky asteroids. We found the best approximation to the data for a combination of 83–17% rocky–P2 populations, which is in agreement with the two-cluster distribution found in Figs. C.1f and C.3g.

4.2.5. Some primitive families

After running the corresponding KS-tests on all the families, we found that four of them were rejected by the statistical test, despite visually presenting similar ML^* distributions to those of P1 or P2 primitive populations. These families are Hygiea, Themis, Hilda, and Ursula. As in the previous cases, we looked for the combination of theoretical distributions that makes the test fail to reject it as a reference distribution, and then determined which distribution best fits the family data.

For Hygiea, this mixed distribution is composed of 67% P1 and 33% P2 populations. This is in agreement with data in the literature: Mothé-Diniz et al. (2001) showed that even though (10) Hygiea is one of the largest known C-type asteroids, a fraction of the objects in the family seem to belong to the Tholen B taxonomic class.

The situation for the Themis family is a bit different. It is similar to the Vesta case, in the sense that the CDF of the family follows almost exactly the CDF for the P1 population. As in the Vesta case, the proportion of one of the populations was extremely high with respect to the other: we found the best-fitting combination for a 95–5% mixture of P1–P2 distributions. This result, however, does not fully agree with the literature: Landsman et al. (2016) showed that this family, although composed of primitive asteroids, presents a diverse composition, and Fornasier et al. (2016) confirmed the spectral diversity within the Themis family. Here we report a slight contamination instead of a compositional variation.

In the case of the Hilda family, located within the Hilda dynamical group, the combination that minimizes the KS-test results is a 36–64% of P1–P2 populations. De Prá et al. (2018) reported a primitive surface composition with a bimodal distribution. This is in agreement with our results.

Information on the Ursula family is scarce, and the only compositional reference is found in Nesvorný et al. (2015), where they report Ursula to be a CX-type family, based on the SDSS colors of its members. For Ursula, the combination that we found is a 49–51% P1–P2, in agreement with the C-X classification from Nesvorný et al. (2015).

4.3. The background

It has been shown that large families have an associated halo of objects that presents similar properties to those of the main family, extending beyond the limits of the families determined using the traditional hierarchical clustering method (Parker et al. 2008; Carruba 2013; Brož & Morbidelli 2013). Apart from some recent efforts to include physical parameters in the identification of collisional families (Parker et al. 2008; Carruba et al. 2013; Masiero et al. 2013), this has long been a purely dynamical process, where the input variables for the family detection method are the proper orbital elements of the asteroids.

In addition to the family analyses, we performed a search on a rough approximation of the concept of halo, or family background. We wanted to check whether a family background (with a very relaxed definition) shares some physical properties with the main family, using the near-infrared colors in MOVIS: in our case, if the unidimensional (ML^*) or bi-dimensional (ML^* vs. p_{NIR} or a^*) distribution shows a similar behavior to that of the corresponding family. We define these backgrounds simply as the groups formed by the asteroids that do not belong to a family, but are located inside a cube in the 3D space of proper orbital elements centered around the mean values of semimajor axis, eccentricity, and sine of inclination of the main family and with an extension up to 3-σ of the mean.

We ran KS-tests comparing the ML^* distribution of the backgrounds to that of their corresponding families. The background selection was performed using the same criteria as those in Sect. 4.1. Table 4 shows the results of these tests. From the 27 families analyzed, 23 backgrounds are, according to the KS-test, compatible with their associated families. The only backgrounds that the KS-test proves as being different from their corresponding families are Vesta, Flora, Adeona, and Mitidika.

If we look at Fig. 10, we can clearly see that the CDFs of Vesta and Flora show a different behavior from that of their backgrounds. This is mainly due to their nearby location in the asteroid belt: the Vesta background is clearly contaminated with a rocky population, coming probably from the entire background of the inner main belt; the Flora background is also contaminated, but with a basaltic population, due to its proximity to the Vesta family. The cases of Adeona and Mitidika are probably similar: they are located near two big rocky families, Eunomia and Juno. It is worth mentioning that the Baptistina family background, although compatible with the family, shows almost the same CDF as the Flora family background. This is, of course, because Baptistina is contained within Flora, and so they share the same background.

In addition to the unidimensional analysis, we also looked for similarities in family background using the near-infrared albedos (p_{NIR}) and the a^*. There are 17 families with more than 40 asteroids observed in MOVIS, coincident within the NEOWISE database, which also present at least ten coincident objects in the background. In the case of the coincidences with the SDSS database, there are just four families fulfilling the mentioned conditions: Vesta, Flora, Nysa–Polana, and Eos. The information provided is statistically less significant than that obtained using NEOWISE since there are fewer background coincidences than in the first case.

In A.2, we present mean values for the different family backgrounds in the MOVIS catalog. We note that most of the analyzed backgrounds share a similar distribution in the ML^* vs. p_{NIR}, and also in the ML^* vs. a^* space as their corresponding families. This is particularly interesting for the cases where the families are significantly different in composition from their surroundings:

- *Vesta*. The background of the Vesta family seems to occupy the same region in the ML^* vs. p_{NIR} space as that occupied by the family (see Fig. C.1a), although there are objects with ML^* and p_{NIR} values similar to those shown by the Flora family, i.e., objects with rocky composition, as expected from the inner belt rock background.

- *Eos*. This similarity is much more significant in this case. The Eos family is located in the outer belt, mainly populated by primitive objects having $ML^* < 0$ and low albedos ($p_{NIR} < 0.1$). But if we look at its background (Fig. C.1e), instead of this primitive population we find objects with a similar distribution to that of the family, suggesting that these objects are very likely related to Eos. This relationship had been previously noted using only SDSS data (Brož & Morbidelli 2013).

- *Nysa–Polana and Baptistina*. The results in this case also point to a close relation between these backgrounds and their families since both families present a bimodal distribution of asteroids and their corresponding backgrounds seem to present the same behavior: two clusters related to the different compositions of the family members.

The information provided here points out, using near-infrared photometry alone (and also in combination with the

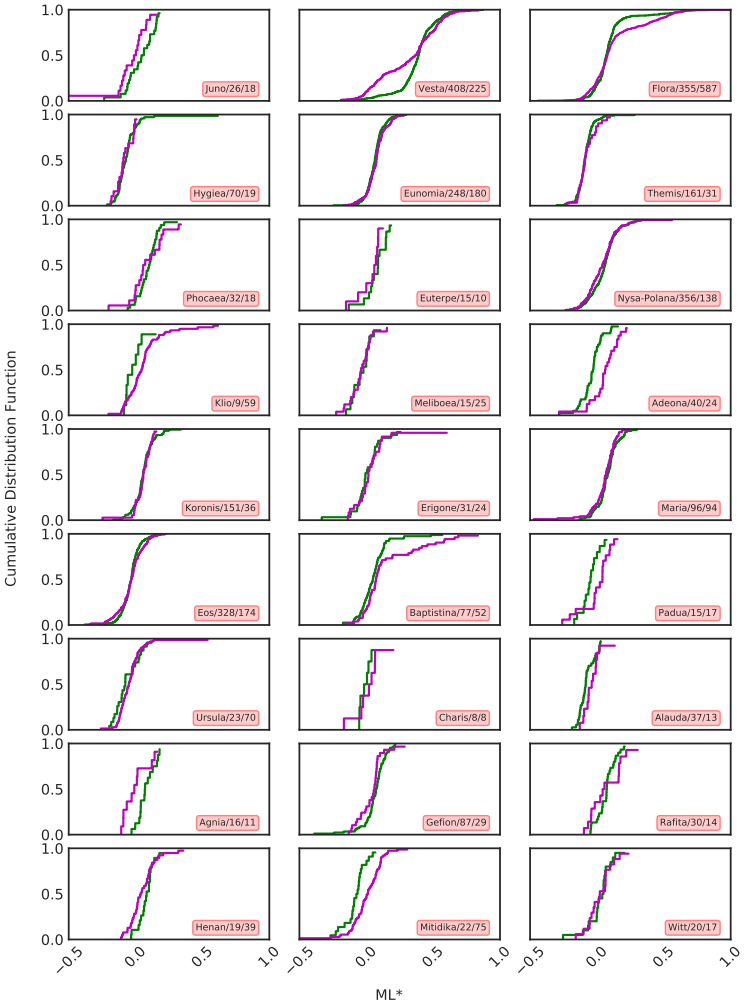

Fig. 10: Cumulative distribution functions for the 27 analyzed families (green) and their associated backgrounds (purple). The selected samples of background to analyze are drawn from the MOVIS database under the same conditions as the main family sample. The box in each plot shows the name of the family, and the number of objects from the family and from the background used for the analysis.

Table 4: Results for the Kolmogorov–Smirnov test used to compare the families to their corresponding backgrounds. The limits for the number of observed members (in both family and background) and their corresponding errors are the same as in Sect. 4.1. $D_{FAM-BGR}$ is the distance between the CDFs of the family and its background, and the $D_{Critical}$ is the critical distance, as in Table 3.

Family	N_{OBS}	N_{BGR}	$D_{FAM-BGR}$	$D_{Critical}$	Compatible
Juno	26	18	0.3162	0.4998	✓
Vesta	408	225	0.2626	0.1354	-
Flora	355	587	0.1467	0.1096	-
Hygiea	70	19	0.1504	0.4217	✓
Eunomia	248	180	0.1341	0.1596	✓
Themis	161	31	0.1513	0.3197	✓
Phocaea	32	18	0.2396	0.4802	✓
Euterpe	15	10	0.3333	0.6654	✓
Nysa–Polana	356	138	0.1295	0.1635	✓
Klio	9	59	0.3804	0.5833	✓
Meliboea	15	25	0.1467	0.5324	✓
Adeona	40	24	0.5833	0.4209	-
Koronis	151	36	0.1038	0.3023	✓
Erigone	31	24	0.1640	0.4432	✓
Maria	96	94	0.1190	0.2365	✓
Eos	328	174	0.1014	0.1529	✓
Baptistina	77	52	0.2173	0.2926	✓
Padua	15	17	0.4980	0.5774	✓
Ursula	23	70	0.2230	0.3918	✓
Charis	8	8	0.3750	0.8150	✓
Alauda	37	13	0.4179	0.5255	✓
Agnia	16	11	0.6023	0.6384	✓
Gefion	87	29	0.2874	0.3495	✓
Rafita	30	14	0.3286	0.5276	✓
Henan	19	39	0.3563	0.4560	✓
Mitidika	22	75	0.4982	0.3952	-
Witt	20	17	0.2118	0.5377	✓

p_{NIR} from NEOWISE and a^* from SDSS), that the family backgrounds are closely related to their family counterparts. This suggests further evidence of halos around the currently known families, confirming what has already been proposed by Parker et al. (2008), Carruba et al. (2013), and Masiero et al. (2013), among others: the definition of asteroid family needs to be updated including physical parameters to constrain family membership.

5. Summary

In the present work, we have conducted an analysis on the families present in the MOVIS catalog. To perform this analysis, we have developed a near-infrared parameter, based on the $Y - J$ and $J - Ks$ colors. In order to define this parameter, we have used those objects with observations in the Y, J, and Ks filters, and with errors in their determination below different thresholds, testing several configurations to construct the final ML^* definition (see Eq. 1). We carried out our analysis combining this parameter with the near-infrared albedos from NEOWISE and the a^* color from SDSS. Within the MOVIS catalog we have found 6299 asteroids, which belong to a total of 104 of the families defined in Nesvorný et al. (2015).

Using the ML^*, we have identified four different distributions within the MOVIS data: P1 and P2 (associated with primitive asteroids, i.e., B-, C-, X-types, and subclasses), rocky (associated with S-types and subclasses), and basaltic (associated with V-types). We compared these distributions with those of the families with $N_{OBS} \geq 8$ and $ML^*_{err} < 0.071$, using Kolmogorov–Smirnov tests. Out of the 43 analyzed families, we report 5 compatible with a P1 distribution, 10 compatible with a P2, and 19 compatible with a rocky population. The KS-test yielded rejections when comparing the other nine families with the four theoretical distributions. In these cases, we compared the families with mixed distributions, avoiding KS-test rejections for all of them. These results are summarized in Table 3. We note that, in general, for the families with a large number of objects, the trend is to be rejected by the KS-test, finding best fits using mixed distributions. This points to a general (although smooth) inhomogeneity in the family compositions.

We are confirming, using near-infrared photometry combined with NEOWISE and SDSS data, some results already known for several families. Vesta shows a small contamination of rocky and primitive asteroids (Licandro et al. 2017); Nysa–Polana presents a bimodality in its composition corresponding to the presence of two families (Cellino et al. 2001; Walsh et al. 2013; Milani et al. 2014; Dykhuis & Greenberg 2015); Eos is the only K-type family identified in the inner belt (Mothé-Diniz et al. 2005, 2008); and Hilda shows some bimodality inside the primitive region (De Prá et al. 2018). In addition, we found relevant results in our analysis related to the Ino and Baptistina families.

The Ino family shows a very different distribution of ML^* compared to the theoretical distributions that we propose, and also compared to all the other families; the best-fitting mixture is for a 60–40% rocky–basaltic combination. In addition, two of the V-type asteroids identified in Licandro et al. (2017) belong to this family. It would be very interesting to check if this com-

position is reflected in the spectroscopic data since there are no known basaltic families apart from Vesta.

Regarding the Baptistina family, if we use the data in the MOVIS catalog combined with the NEOWISE near-infrared albedos, we find that it presents a two-cluster distribution within the ML^* vs. p_{NIR} space. By comparing the ML^* distribution of Baptistina to that of a mixture of two theoretical populations, we find the best fit for a combination of 83–17% rocky-P2; in other words, the ML^* confirms this bimodality by itself. This can be explained if this family is the result of the breakup of a differentiated parent body (which would be unique to the main asteroid belt). Otherwise, this family presents high contamination from the Flora family rocky background. It can also be hypothesized that Baptistina is actually formed of two families, one formed of high-albedo rocky objects, and the other composed of primitive asteroids with moderately low albedos.

Finally, we used Kolmogorov–Smirnov tests to compare the background populations that we defined against their associated families. We report compatibilities between the families and their backgrounds in 23 out of the 27 studied cases (see Table 4). We show that the surrounding objects usually have a similar composition to that of the main family. This provides further evidence for the necessity of an update in the definitions of asteroid families: using only dynamical elements to address family membership will not give results that are as accurate as those that we would be able to obtain if we also took into account physical properties, such as the albedo, photometry, or even spectroscopy, whenever available.

Acknowledgements. *DM* gratefully acknowledges the Spanish Ministry of Economy and Competitiveness (MINECO) for the financial support received in the form of a Severo-Ochoa PhD fellowship, within the Severo-Ochoa International PhD Program. All the authors acknowledge support from the AYA2015-67772-R (MINECO, Spain), and from the Instituto de Astrofísica de Canarias. *JdL* acknowledges financial support from MINECO under the 2015 Severo Ochoa Program MINECO SEV-2015-0548. The work of *MP* was also supported by a grant from the Romanian National Authority for Scientific Research - UEFISCDI, project number PN-III-P1-1.2-PCCDI-2017-0371. The authors would also like to thank the referee for the comments and suggestions that helped to improve this article.

References

Bessell, M. S. 2005, ARA&A, 43, 293
Binzel, R. P. & Xu, S. 1993, Science, 260, 186
Bottke, Jr., W. F., Vokrouhlický, D., Rubincam, D. P., & Broz, M. 2002, The Effect of Yarkovsky Thermal Forces on the Dynamical Evolution of Asteroids and Meteoroids, ed. W. F. Bottke, Jr., A. Cellino, P. Paolicchi, & R. P. Binzel, 395–408
Brož, M. & Morbidelli, A. 2013, Icarus, 223, 844
Brož, M., Morbidelli, A., Bottke, W. F., et al. 2013, A&A, 551, A117
Carruba, V. 2013, MNRAS, 431, 3557
Carruba, V., Domingos, R. C., Nesvorný, D., et al. 2013, MNRAS, 433, 2075
Carvano, J. M., Hasselmann, P. H., Lazzaro, D., & Mothé-Diniz, T. 2010, A&A, 510, A43
Cellino, A., Zappalà, V., Doressoundiram, A., et al. 2001, Icarus, 152, 225
De Prá, M. N., Pinilla-Alonso, N., Carvano, J. M. F., et al. 2018, Icarus
DeMeo, F. E., Binzel, R. P., Slivan, S. M., & Bus, S. J. 2009, Icarus, 202, 160
DeMeo, F. E. & Carry, B. 2013, Icarus, 226, 723
Doressoundiram, A., Barucci, M. A., Fulchignoni, M., & Florczak, M. 1998, Icarus, 131, 15
Dykhuis, M. J. & Greenberg, R. 2015, Icarus, 252, 199
Florczak, M., Barucci, M. A., Doressoundiram, A., et al. 1998, Icarus, 133, 233
Florczak, M., Lazzaro, D., Mothé-Diniz, T., Angeli, C. A., & Betzler, A. S. 1999, A&AS, 134, 463
Fornasier, S., Lantz, C., Perna, D., et al. 2016, Icarus, 269, 1
Gil-Hutton, R. 2006, Icarus, 183, 93
Ishihara, D., Onaka, T., Kataza, H., et al. 2010, A&A, 514, A1
Ivezić, Ž., Lupton, R. H., Jurić, M., et al. 2002, AJ, 124, 2943
Ivezić, Ž., Tabachnik, S., Rafikov, R., et al. 2001, AJ, 122, 2749
Jarrett, T. H., Cohen, M., Masci, F., et al. 2011, ApJ, 735, 112
Kaiser, N., Burgett, W., Chambers, K., et al. 2010, in Proc. SPIE, Vol. 7733, Ground-based and Airborne Telescopes III, 77330E
Landsman, Z. A., Licandro, J., Campins, H., et al. 2016, Icarus, 269, 62
Licandro, J., Popescu, M., Morate, D., & de León, J. 2017, A&A, 600, A126
Mainzer, A., Bauer, J., Cutri, R. M., et al. 2014, ApJ, 792, 30
Mainzer, A., Grav, T., Bauer, J., et al. 2011, ApJ, 743, 156
Masiero, J. R., DeMeo, F. E., Kasuga, T., & Parker, A. H. 2015, Asteroid Family Physical Properties, ed. P. Michel, F. E. DeMeo, & W. F. Bottke, 323–340
Masiero, J. R., Grav, T., Mainzer, A. K., et al. 2014, ApJ, 791, 121
Masiero, J. R., Mainzer, A. K., Bauer, J. M., et al. 2013, ApJ, 770, 7
Masiero, J. R., Mainzer, A. K., Grav, T., et al. 2011, ApJ, 741, 68
Mayne, R. G., Sunshine, J. M., McSween, H. Y., Bus, S. J., & McCoy, T. J. 2011, Icarus, 214, 147
McCord, T. B., Adams, J. B., & Johnson, T. V. 1970, Science, 168, 1445
McMahon, R. G., Banerji, M., Gonzalez, E., et al. 2013, The Messenger, 154, 35
Milani, A., Cellino, A., Knežević, Z., et al. 2014, Icarus, 239, 46
Morate, D., de León, J., De Prá, M., et al. 2016, A&A, 586, A129
Moskovitz, N. A., Willman, M., Burbine, T. H., Binzel, R. P., & Bus, S. J. 2010, Icarus, 208, 773
Mothé-Diniz, T., Carvano, J. M., Bus, S. J., Duffard, R., & Burbine, T. H. 2008, Icarus, 195, 277
Mothé-Diniz, T., di Martino, M., Bendjoya, P., Doressoundiram, A., & Migliorini, F. 2001, Icarus, 152, 117
Mothé-Diniz, T., Roig, F., & Carvano, J. M. 2005, Icarus, 174, 54
Nesvorny, D. 2010, NASA Planetary Data System, 133
Nesvorny, D. 2012, NASA Planetary Data System, 189
Nesvorný, D., Brož, M., & Carruba, V. 2015, Identification and Dynamical Properties of Asteroid Families, ed. P. Michel, F. E. DeMeo, & W. F. Bottke, 297–321
Nesvorný, D., Jedicke, R., Whiteley, R. J., & Ivezić, Ž. 2005, Icarus, 173, 132
Newville, M., Stensitzki, T., Allen, D. B., & Ingargiola, A. 2014, LMFIT: Non-Linear Least-Square Minimization and Curve-Fitting for Python¶
Novaković, B., Cellino, A., & Knežević, Z. 2011, Icarus, 216, 69
Parker, A., Ivezić, Ž., Jurić, M., et al. 2008, Icarus, 198, 138
Popescu, M., Licandro, J., Carvano, J. M. F., et al. 2018, Submitted to A&A
Popescu, M., Licandro, J., Morate, D., et al. 2016, A&A, 591, A115
Reddy, V., Carvano, J. M., Lazzaro, D., et al. 2011, Icarus, 216, 184
Skrutskie, M. F., Cutri, R. M., Stiening, R., et al. 2006, AJ, 131, 1163
Stephens, M. 1970, Journal of the Royal Statistical Society. ser. B, 32, 115
Sutherland, W., Emerson, J., Dalton, G., et al. 2015, A&A, 575, A25
Tedesco, E. F., Gradie, J., Tholen, D. J., & Zellner, B. 1982, in BAAS, Vol. 14, Bulletin of the American Astronomical Society, 720
Vokrouhlický, D., Brož, M., Morbidelli, A., et al. 2006, Icarus, 182, 92
Walsh, K. J., Delbó, M., Bottke, W. F., Vokrouhlický, D., & Lauretta, D. S. 2013, Icarus, 225, 283
Waskom, M., Botvinnik, O., O'Kane, D., et al. 2017, mwaskom/seaborn: v0.8.1 (September 2017)
Wright, E. L., Eisenhardt, P. R. M., Mainzer, A. K., et al. 2010, AJ, 140, 1868
York, D. G., Adelman, J., Anderson, Jr., J. E., et al. 2000, AJ, 120, 1579

Appendices

Appendix A: Additional tables

Table A.1: Mean values of ML^* computed for the different families present in the MOVIS catalog. Families are ordered by the number of their homonym asteroid. In the third column we provide the family identification number from Nesvorný et al. (2015) (FIN) so that it is easier to directly compare this work to others. We also added the mean values of semimajor axis, eccentricity, and sine of inclination for each family, as well as the corresponding SDSS and/or NEOWISE data, whenever possible. The p_{NIR} and a^* are the computed mean and sigma from the data in the catalogs, excluding non-valid observations. We label the families as primitive 1 (P1), primitive 2 (P2), rocky (R), basaltic (B), and in the special case of Eos, K.

Fam. Name	Fam.	FIN	a (AU)	e	sin(i)	ML^*	N_{MOVIS}	p_{NIR}	$N_{NEOWISE}$	a^*	N_{SDSS}	Class
Pallas	2	801	2.758 ± 0.043	0.266 ± 0.016	0.544 ± 0.008	0.047 ± 0.062	3	0.203 ± 0.074	95	-	-	-
Juno	3	501	2.656 ± 0.026	0.235 ± 0.005	0.231 ± 0.004	0.045 ± 0.113	55	0.320 ± 0.144	271	0.062 ± 0.099	381	R
Vesta	4	401	2.357 ± 0.054	0.099 ± 0.011	0.115 ± 0.007	0.355 ± 0.097	801	0.522 ± 0.165	1878	0.117 ± 0.272	3934	93B - 7P2-R
Flora	8	402	2.265 ± 0.048	0.138 ± 0.015	0.087 ± 0.015	0.071 ± 0.087	601	0.393 ± 0.133	2605	0.093 ± 0.311	2844	R
Hygiea	10	601	3.153 ± 0.047	0.130 ± 0.015	0.090 ± 0.006	-0.114 ± 0.115	187	0.108 ± 0.044	2231	-0.108 ± 0.260	1147	67P1 - 33P2
Eunomia	15	502	2.622 ± 0.047	0.150 ± 0.009	0.227 ± 0.007	0.035 ± 0.091	396	0.385 ± 0.123	2164	0.125 ± 0.140	1691	R
Massalia	20	404	2.402 ± 0.032	0.162 ± 0.006	0.026 ± 0.002	0.037 ± 0.106	132	0.334 ± 0.144	289	0.068 ± 0.247	1299	R
Themis	24	602	3.139 ± 0.049	0.149 ± 0.014	0.024 ± 0.005	-0.121 ± 0.092	286	0.102 ± 0.036	2260	-0.110 ± 0.168	1134	95P1 - 5P2
Phocaea	25	701	2.330 ± 0.043	0.227 ± 0.029	0.398 ± 0.011	0.063 ± 0.083	60	0.365 ± 0.130	891	-	-	R
Euterpe	27	410	2.367 ± 0.034	0.190 ± 0.006	0.015 ± 0.002	0.054 ± 0.117	32	0.391 ± 0.157	58	0.102 ± 0.255	126	R
Euphrosyne	31	901	3.158 ± 0.034	0.196 ± 0.029	0.448 ± 0.006	-0.108 ± 0.115	53	0.086 ± 0.032	1493	-	-	P1
Nysa–Polana	44	405	2.382 ± 0.048	0.172 ± 0.019	0.044 ± 0.005	0.015 ± 0.107	779	0.242 ± 0.110	3206	0.075 ± 0.336	4479	90R - 10P2
Terpsichore	81	622	2.881 ± 0.023	0.186 ± 0.008	0.142 ± 0.004	0.057 ± 0.225	2	0.083 ± 0.037	82	-0.073 ± 0.046	35	-
Klio	84	413	2.381 ± 0.045	0.193 ± 0.008	0.165 ± 0.009	-0.102 ± 0.115	18	0.100 ± 0.034	330	-0.074 ± 0.196	105	P2
Sylvia	87	603	3.477 ± 0.056	0.066 ± 0.013	0.172 ± 0.004	-0.151 ± 0.112	9	0.080 ± 0.029	152	-0.061 ± 0.076	48	-
Aegle	96	630	3.055 ± 0.010	0.184 ± 0.002	0.284 ± 0.002	0.049 ± 0.086	4	0.106 ± 0.033	74	0.013 ± 0.039	26	-
Nemesis	128	504	2.735 ± 0.020	0.090 ± 0.004	0.085 ± 0.004	-0.089 ± 0.124	22	0.116 ± 0.055	437	-0.067 ± 0.193	267	-
Meliboea	137	604	3.149 ± 0.031	0.191 ± 0.013	0.253 ± 0.008	-0.067 ± 0.091	30	0.099 ± 0.040	292	-0.078 ± 0.185	114	P2
Vibilia	144	529	2.684 ± 0.012	0.191 ± 0.004	0.067 ± 0.002	-0.016 ± 0.076	2	0.113 ± 0.048	73	-0.077 ± 0.206	45	-
Adeona	145	505	2.644 ± 0.036	0.165 ± 0.006	0.202 ± 0.003	-0.064 ± 0.098	87	0.105 ± 0.049	1429	-0.079 ± 0.331	594	P2
Gallia	148	802	2.751 ± 0.031	0.133 ± 0.018	0.424 ± 0.005	0.042 ± 0.165	3	0.374 ± 0.161	44	-	-	-
Hilda	153	001	3.965 ± 0.003	0.181 ± 0.046	0.153 ± 0.009	-0.115 ± 0.096	29	0.077 ± 0.077	2	-	-	36P1 - 64P2
Koronis	158	605	2.892 ± 0.036	0.056 ± 0.015	0.037 ± 0.002	0.026 ± 0.094	281	0.351 ± 0.116	1039	0.087 ± 0.445	1248	R
Koronis(2)	158	621	2.868 ± 0.002	0.045 ± 0.000	0.038 ± 0.000	-0.178 ± 0.144	2	0.368 ± 0.146	6	0.049 ± 0.055	29	-
Erigone	163	406	2.368 ± 0.024	0.207 ± 0.005	0.088 ± 0.005	0.002 ± 0.105	74	0.093 ± 0.048	850	-0.039 ± 0.247	405	44P2 - 56R
Maria	170	506	2.609 ± 0.045	0.094 ± 0.012	0.254 ± 0.006	0.050 ± 0.099	185	0.377 ± 0.131	987	0.104 ± 0.191	873	R
Ino	173	522	2.757 ± 0.030	0.176 ± 0.003	0.233 ± 0.002	0.103 ± 0.107	27	0.361 ± 0.134	87	0.084 ± 0.149	128	60R - 40B
Eos	221	606	3.044 ± 0.055	0.072 ± 0.013	0.174 ± 0.008	-0.069 ± 0.091	599	0.218 ± 0.083	4024	0.044 ± 0.291	2709	K (25P1 - 55P2 - 20R)
Emma	283	607	3.051 ± 0.011	0.116 ± 0.005	0.159 ± 0.002	-0.075 ± 0.118	26	0.071 ± 0.025	315	-0.073 ± 0.113	102	-
Brasilia	293	608	2.853 ± 0.010	0.122 ± 0.002	0.259 ± 0.002	-0.144 ± 0.138	21	0.260 ± 0.108	130	-0.040 ± 0.210	163	-
Baptistina	298	403	2.276 ± 0.026	0.143 ± 0.007	0.098 ± 0.006	0.035 ± 0.095	149	0.312 ± 0.119	692	0.028 ± 0.115	603	R (83R - 17P2)
Clarissa	302	407	2.400 ± 0.008	0.107 ± 0.002	0.059 ± 0.001	-0.153 ± 0.147	4	0.080 ± 0.040	68	-0.129 ± 0.065	35	-
Chaldaea	313	415	2.403 ± 0.026	0.228 ± 0.007	0.192 ± 0.009	-0.043 ± 0.135	6	0.102 ± 0.029	132	-0.099 ± 0.093	37	-
Phaeo	322	530	2.772 ± 0.020	0.183 ± 0.010	0.162 ± 0.003	-0.164 ± 0.079	7	0.098 ± 0.037	146	-0.016 ± 0.062	45	-
Svea	329	416	2.451 ± 0.017	0.092 ± 0.006	0.276 ± 0.002	0.018 ± 0.168	1	0.086 ± 0.035	35	-0.073 ± 0.043	7	-
Padua	363	507	2.734 ± 0.027	0.043 ± 0.008	0.092 ± 0.003	-0.085 ± 0.099	44	0.102 ± 0.041	605	-0.033 ± 0.338	242	P2
Aeria	369	539	2.657 ± 0.036	0.056 ± 0.004	0.200 ± 0.004	0.091 ± 0.107	9	0.243 ± 0.116	52	-0.013 ± 0.106	72	-
Ursula	375	631	3.144 ± 0.042	0.083 ± 0.016	0.280 ± 0.008	-0.107 ± 0.116	70	0.101 ± 0.043	917	-0.035 ± 0.068	353	49P1 - 51P2
Aeolia	396	508	2.741 ± 0.003	0.168 ± 0.001	0.060 ± 0.001	-0.002 ± 0.127	9	0.153 ± 0.073	56	-0.034 ± 1.459	47	-
Chloris	410	509	2.755 ± 0.032	0.255 ± 0.006	0.152 ± 0.004	-0.027 ± 0.078	22	0.157 ± 0.074	193	-0.014 ± 0.145	121	R
Hungaria	434	003	1.934 ± 0.027	0.075 ± 0.012	0.360 ± 0.010	-0.039 ± 0.112	75	0.786 ± 0.169	88	-	-	P2
Hansa	480	803	2.631 ± 0.041	0.041 ± 0.028	0.374 ± 0.004	0.082 ± 0.121	37	0.402 ± 0.150	361	-	-	R
Veritas	490	609	3.170 ± 0.005	0.063 ± 0.004	0.160 ± 0.004	-0.129 ± 0.115	36	0.103 ± 0.042	713	-0.068 ± 0.109	314	P2
Misa	569	510	2.650 ± 0.023	0.178 ± 0.004	0.040 ± 0.003	-0.061 ± 0.154	12	0.085 ± 0.039	316	-0.075 ± 0.169	143	P2
Croatia	589	638	3.120 ± 0.032	0.031 ± 0.003	0.186 ± 0.001	-0.108 ± 0.119	8	0.084 ± 0.031	107	-0.040 ± 0.060	42	-
Brangane	606	511	2.583 ± 0.005	0.180 ± 0.001	0.167 ± 0.001	0.019 ± 0.058	4	0.176 ± 0.079	59	0.098 ± 0.166	47	-
Elfriede	618	632	3.188 ± 0.006	0.058 ± 0.001	0.274 ± 0.002	-0.087 ± 0.159	1	0.079 ± 0.028	38	-0.112 ± 0.053	11	-
Chimaera	623	414	2.436 ± 0.022	0.148 ± 0.006	0.256 ± 0.004	-0.014 ± 0.070	8	0.100 ± 0.047	79	-0.053 ± 0.041	27	-
Hector	624	004	5.290 ± 0.004	0.055 ± 0.001	0.325 ± 0.001	-0.111 ± 0.002	1	-	-	-	-	-
Charis	627	616	2.878 ± 0.029	0.051 ± 0.009	0.105 ± 0.005	0.015 ± 0.126	27	0.184 ± 0.079	71	0.147 ± 0.110	142	P2
Beagle	656	620	3.156 ± 0.006	0.152 ± 0.001	0.023 ± 0.001	-0.219 ± 0.142	2	0.102 ± 0.047	49	-0.104 ± 0.049	32	-
Dora	668	512	2.786 ± 0.015	0.196 ± 0.003	0.137 ± 0.002	-0.047 ± 0.088	64	0.085 ± 0.037	816	-0.119 ± 0.155	321	P2
Gersuind	686	804	2.597 ± 0.038	0.174 ± 0.010	0.297 ± 0.007	0.014 ± 0.104	15	0.210 ± 0.092	198	0.085 ± 0.118	68	P2
Alauda	702	902	3.165 ± 0.048	0.086 ± 0.041	0.376 ± 0.009	-0.105 ± 0.101	75	0.103 ± 0.031	1034	-	-	P1
Fringilla	709	623	2.886 ± 0.033	0.091 ± 0.019	0.293 ± 0.005	-0.071 ± 0.075	6	0.085 ± 0.041	105	-0.014 ± 0.070	33	-
Watsonia	729	537	2.787 ± 0.022	0.124 ± 0.010	0.297 ± 0.003	-0.048 ± 0.092	8	0.187 ± 0.067	64	0.065 ± 0.133	20	-
Sulamitis	752	408	2.441 ± 0.022	0.090 ± 0.003	0.088 ± 0.003	-0.017 ± 0.106	12	0.089 ± 0.042	174	-0.049 ± 0.062	60	-
Theobalda	778	617	3.178 ± 0.007	0.254 ± 0.005	0.247 ± 0.003	-0.089 ± 0.064	6	0.096 ± 0.037	177	-0.158 ± 0.192	88	-
Merxia	808	513	2.751 ± 0.031	0.135 ± 0.004	0.087 ± 0.002	0.069 ± 0.093	30	0.323 ± 0.130	114	0.075 ± 0.119	272	R
Juliana	816	641	2.992 ± 0.018	0.145 ± 0.004	0.229 ± 0.002	-0.032 ± 0.053	2	0.111 ± 0.057	43	-0.016 ± 0.038	18	-
Karin	832	610	2.865 ± 0.004	0.044 ± 0.001	0.037 ± 0.000	-0.001 ± 0.126	15	0.287 ± 0.137	30	0.032 ± 0.097	82	-
Naema	845	611	2.935 ± 0.012	0.036 ± 0.002	0.207 ± 0.001	-0.282 ± 0.157	8	0.091 ± 0.030	234	-0.088 ± 0.050	75	-

Table A.1: Continuation

Fam. Name	Fam.	FIN	a (AU)	e	sin(i)	ML^*	N_{MOVIS}	p_{NIR}	$N_{NEOWISE}$	a^*	N_{SDSS}	Class
Agnia	847	514	2.788 ± 0.017	0.073 ± 0.004	0.066 ± 0.004	0.016 ± 0.091	34	0.325 ± 0.131	128	0.044 ± 0.129	416	R
Ulla	909	903	3.550 ± 0.012	0.048 ± 0.004	0.308 ± 0.001	-0.107 ± 0.033	1	0.087 ± 0.021	20	-	-	-
Itha	918	633	2.861 ± 0.016	0.160 ± 0.004	0.210 ± 0.003	0.031 ± 0.077	3	0.346 ± 0.112	27	0.113 ± 0.131	19	-
Imhilde	926	639	2.988 ± 0.013	0.231 ± 0.002	0.255 ± 0.002	-0.097 ± 0.037	2	0.071 ± 0.018	20	-0.061 ± 0.048	13	-
Barcelona	945	805	2.624 ± 0.013	0.240 ± 0.023	0.514 ± 0.002	0.078 ± 0.085	7	0.434 ± 0.162	86	-	-	-
Astrid	1128	515	2.780 ± 0.016	0.049 ± 0.001	0.012 ± 0.002	-0.030 ± 0.116	7	0.072 ± 0.033	221	-0.064 ± 0.409	80	-
Terentia	1189	618	2.927 ± 0.012	0.072 ± 0.001	0.193 ± 0.001	0.088 ± 0.105	2	0.091 ± 0.039	44	-0.042 ± 0.062	16	-
Tina	1222	806	2.789 ± 0.010	0.093 ± 0.017	0.355 ± 0.003	-0.088 ± 0.112	4	0.197 ± 0.090	41	-	-	-
Datura	1270	411	2.235 ± 0.000	0.153 ± 0.000	0.092 ± 0.000	0.023 ± 0.049	3	0.387 ± 0.049	1	0.010 ± 0.030	1	-
Gefion	1272	516	2.763 ± 0.027	0.128 ± 0.012	0.158 ± 0.004	0.041 ± 0.092	178	0.354 ± 0.128	747	0.096 ± 0.108	743	R
Luthera	1303	904	3.220 ± 0.009	0.122 ± 0.006	0.322 ± 0.005	-0.069 ± 0.139	10	0.073 ± 0.024	135	-	-	-
Tirela	1400	612	3.128 ± 0.021	0.198 ± 0.007	0.289 ± 0.004	0.005 ± 0.116	48	0.287 ± 0.115	375	0.148 ± 0.436	340	R
Postrema	1484	541	2.753 ± 0.027	0.236 ± 0.006	0.284 ± 0.003	0.004 ± 0.162	4	0.099 ± 0.038	73	0.105 ± 0.411	21	-
Rafita	1644	518	2.592 ± 0.025	0.173 ± 0.007	0.132 ± 0.005	0.030 ± 0.086	48	0.337 ± 0.127	282	0.079 ± 0.171	350	R
Hanna	1668	533	2.788 ± 0.012	0.175 ± 0.004	0.073 ± 0.002	-0.030 ± 0.107	11	0.088 ± 0.048	120	-0.079 ± 0.069	52	-
Hoffmeister	1726	519	2.783 ± 0.014	0.048 ± 0.003	0.077 ± 0.003	-0.160 ± 0.116	38	0.072 ± 0.033	977	-0.094 ± 0.137	346	P1
Lucienne	1892	409	2.458 ± 0.014	0.096 ± 0.003	0.251 ± 0.001	0.027 ± 0.072	9	0.346 ± 0.138	27	0.065 ± 0.067	31	-
Schubart	1911	002	3.966 ± 0.001	0.192 ± 0.017	0.050 ± 0.002	-0.223 ± 0.159	17	0.113 ± 0.068	5	-	-	-
Henan	2085	532	2.705 ± 0.044	0.057 ± 0.006	0.040 ± 0.006	-0.002 ± 0.111	59	0.288 ± 0.115	186	0.100 ± 0.224	417	R
Mitidika	2262	531	2.595 ± 0.036	0.244 ± 0.016	0.218 ± 0.008	-0.065 ± 0.090	41	0.098 ± 0.036	653	-0.111 ± 0.087	188	P1
Xizang	2344	536	2.748 ± 0.028	0.156 ± 0.004	0.047 ± 0.003	0.009 ± 0.097	9	0.193 ± 0.080	54	0.023 ± 0.266	59	-
Witt	2732	535	2.735 ± 0.035	0.023 ± 0.011	0.107 ± 0.003	-0.018 ± 0.120	63	0.340 ± 0.134	89	0.153 ± 0.137	345	R
Jones	3152	538	2.629 ± 0.002	0.109 ± 0.001	0.214 ± 0.000	0.054 ± 0.146	1	0.077 ± 0.025	15	0.010 ± 0.038	3	-
Inarradas	3438	634	3.051 ± 0.009	0.180 ± 0.003	0.252 ± 0.001	0.045 ± 0.074	2	0.113 ± 0.032	24	-0.106 ± 0.036	13	-
Lixiaohua	3556	613	3.148 ± 0.009	0.198 ± 0.005	0.177 ± 0.002	-0.101 ± 0.082	24	0.066 ± 0.025	511	-0.057 ± 0.109	175	P1
Karma	3811	534	2.566 ± 0.021	0.106 ± 0.003	0.187 ± 0.002	-0.026 ± 0.133	7	0.105 ± 0.037	83	-0.055 ± 0.036	26	-
Konig	3815	517	2.573 ± 0.005	0.140 ± 0.001	0.152 ± 0.003	-0.036 ± 0.101	12	0.074 ± 0.036	239	-0.087 ± 0.165	67	-
Brucato	4203	807	2.610 ± 0.043	0.122 ± 0.027	0.475 ± 0.011	-0.096 ± 0.087	14	0.100 ± 0.038	272	-	-	P2
Iannini	4652	520	2.644 ± 0.001	0.268 ± 0.001	0.212 ± 0.000	0.112 ± 0.119	5	0.431 ± 0.152	20	0.006 ± 0.042	38	-
Ennomos	4709	009	5.304 ± 0.021	0.031 ± 0.005	0.462 ± 0.007	0.047 ± 0.096	2	-	-	-	-	-
Yakovlev	5614	625	2.873 ± 0.014	0.287 ± 0.006	0.139 ± 0.002	-0.237 ± 0.148	2	0.070 ± 0.036	44	-0.051 ± 0.613	17	-
Kazuya	7353	521	2.567 ± 0.002	0.146 ± 0.003	0.253 ± 0.001	0.057 ± 0.109	4	0.277 ± 0.141	13	0.021 ± 0.044	11	-
Anfimov	7468	635	3.054 ± 0.015	0.089 ± 0.001	0.060 ± 0.001	-0.134 ± 0.038	1	0.241 ± 0.108	12	0.224 ± 0.248	21	-
Telramund	9506	614	2.989 ± 0.013	0.071 ± 0.007	0.154 ± 0.003	0.028 ± 0.102	23	0.288 ± 0.124	104	0.080 ± 0.143	117	R
1996RJ	9799	006	5.231 ± 0.004	0.040 ± 0.000	0.527 ± 0.002	-0.073 ± 0.101	1	-	-	-	-	-
Lau	10811	619	2.926 ± 0.009	0.196 ± 0.007	0.111 ± 0.001	0.067 ± 0.193	3	0.162 ± 0.033	5	0.243 ± 0.056	13	-
1998YB3	15454	627	2.866 ± 0.009	0.220 ± 0.002	0.275 ± 0.001	-0.078 ± 0.096	6	0.071 ± 0.029	27	-0.066 ± 0.134	13	-
1999CG1	15477	628	2.892 ± 0.038	0.085 ± 0.008	0.088 ± 0.004	0.054 ± 0.136	5	0.146 ± 0.065	72	0.002 ± 0.177	49	-
1993FY12	18405	615	2.845 ± 0.007	0.106 ± 0.001	0.160 ± 0.001	-0.207 ± 0.153	3	0.251 ± 0.082	16	-0.049 ± 0.656	22	-
1999XT17	36256	629	2.937 ± 0.014	0.115 ± 0.003	0.185 ± 0.001	-0.061 ± 0.080	4	0.305 ± 0.088	17	0.225 ± 0.065	11	-
2000BY6	53546	526	2.722 ± 0.007	0.172 ± 0.001	0.249 ± 0.001	0.155 ± 0.022	2	0.208 ± 0.139	1	0.033 ± 0.049	13	-
2000UJ87	106302	637	3.106 ± 0.008	0.180 ± 0.003	0.060 ± 0.002	-0.353 ± 0.130	1	0.069 ± 0.031	13	-0.090 ± 0.307	10	-

Table A.2: Mean ML^*, p_{NIR}, and a^* for the background populations of the families with more than 40 asteroids observed in MOVIS, and with more than 10 asteroids in coincidence with the SDSS and NEOWISE databases.

Background of:	Fam. Number	ML^*	N_{MOVIS}	p_{NIR}	$N_{NEOWISE}$	a^*	N_{SDSS}
Vesta	4	0.262±0.099	469	0.156±0.476	150	0.018±0.112	13
Flora	8	0.096±0.103	1207	0.142±0.404	463	0.015±0.102	39
Hygiea	10	-0.126±0.123	79	0.056±0.117	49	-	-
Eunomia	15	0.040±0.098	342	0.129±0.373	184	-	-
Themis	24	-0.102±0.105	85	0.042±0.111	60	-	-
Nysa–Polana	44	0.009±0.111	343	0.116±0.294	105	0.030±0.072	13
Adeona	145	-0.020±0.105	57	0.108±0.266	32	-	-
Koronis	158	0.014±0.105	72	0.123±0.332	40	-	-
Erigone	163	0.041±0.114	57	0.109±0.253	19	-	-
Maria	170	0.015±0.096	188	0.133±0.378	98	-	-
Eos	221	-0.074±0.114	447	0.079±0.209	221	0.022±0.027	13
Baptistina	298	0.109±0.104	100	0.155±0.455	43	-	-
Ursula	375	-0.055±0.107	151	0.058±0.124	96	-	-
Alauda	702	-0.098±0.093	32	0.070±0.136	22	-	-
Gefion	1272	0.011±0.120	61	0.128±0.310	26	-	-
Mitidika	2262	-0.035±0.109	157	0.088±0.238	77	-	-

Appendix B: Auxiliary figures

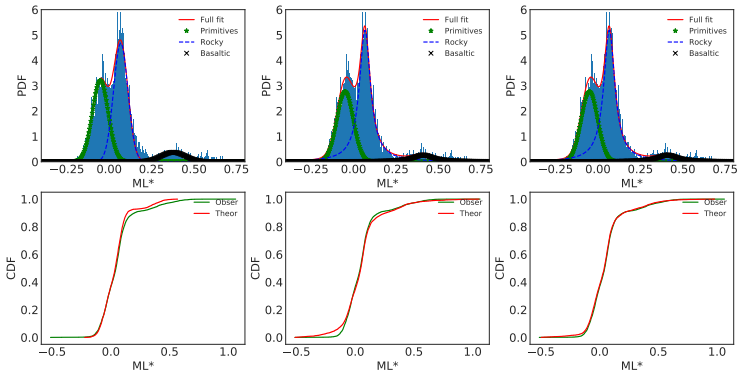

Fig. B.1: Graphical representation of the results of the fits for the case where we assumed three distributions: three Gaussians (left), three Lorentzians (center), one Gaussian for the primitive population and two Lorentzians for both rocky and basaltic populations (right). The upper plots represent the probability density functions associated with the ML^* distributions. The lower plots are the corresponding cumulative distribution functions.

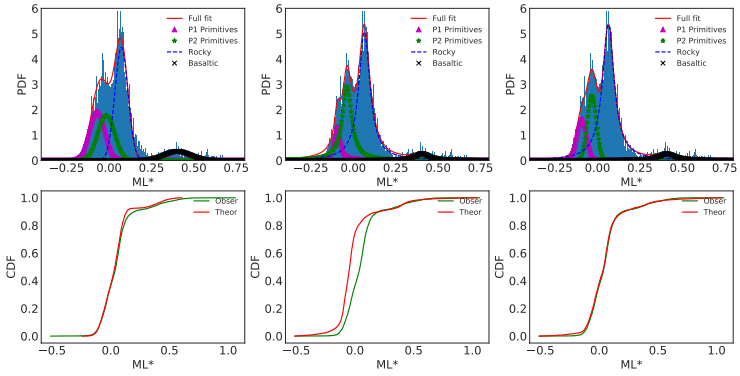

Fig. B.2: Same as Fig. B.1, but with four distributions: four Gaussians (left), four Lorentzians (center), two Gaussians for the two primitive populations, and two Lorentzians for both rocky and basaltic populations (right). We can see that the combinations in the right panels of Figs. B.1 and B.2 fit the observations accurately.

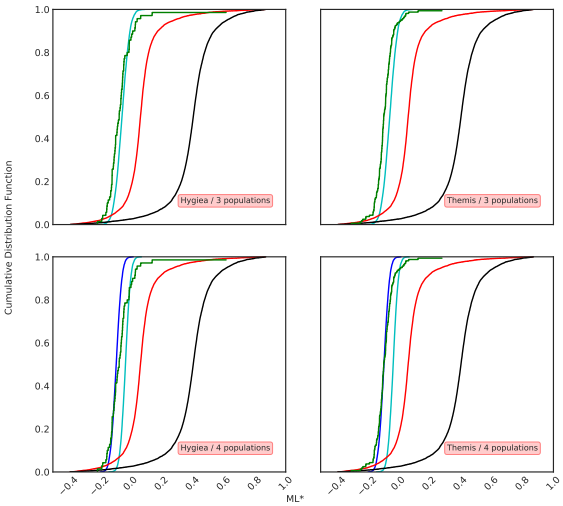

Fig. B.3: CDFs of the theoretical distributions defined for the case of a three-population fit and those defined for a four-population fit, compared to the primitive families with the highest number of objects in the MOVIS catalog (Hygiea and Themis). In the upper plots we show the three-population case (primitive in cyan, rocky in red, basaltic in black). The lower plots show the four-population case (P1 in blue, P2 in cyan).

Appendix C: Density plots of the detected families

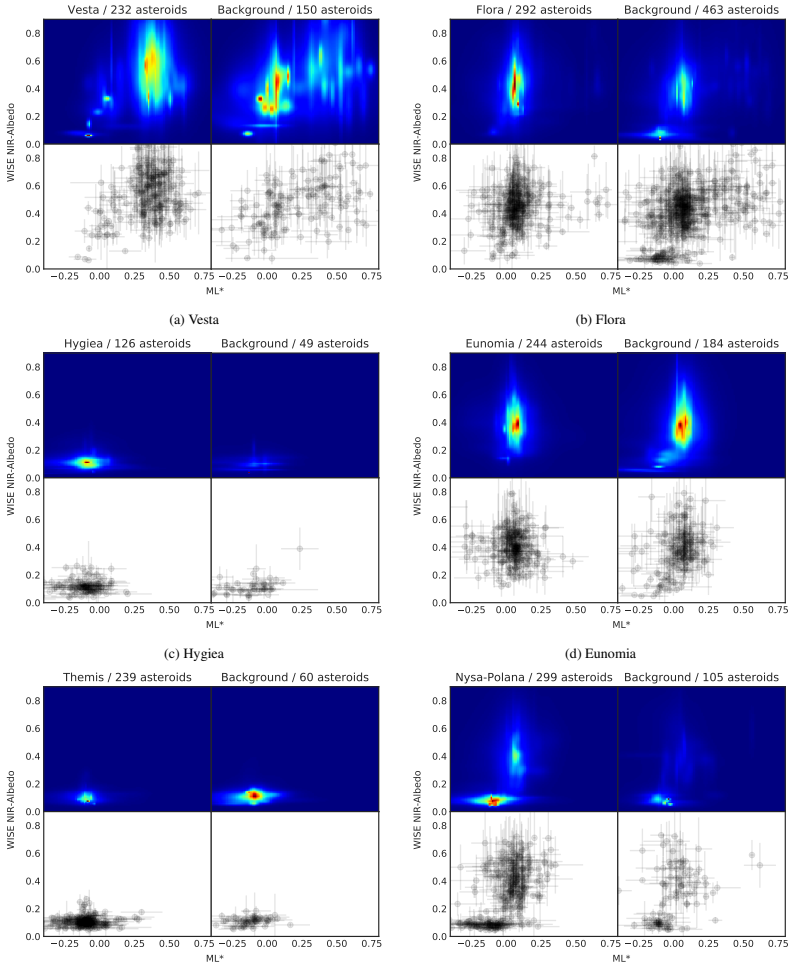

(a) Vesta (b) Flora

(c) Hygiea (d) Eunomia

(e) Themis (f) Nysa–Polana

Fig. C.1: Asteroid families detected within the MOVIS catalog, with at least 40 coincidences with NEOWISE, and with a background of at least ten asteroids. In these plots we represent ML^* vs. p_{NIR}. On the left, we represent the observed family, and on the right the background we defined for that same family. Upper plots are weighted density plots (see text for explanation), and lower plots are scatter representations of the observed asteroids, with the corresponding error bars.

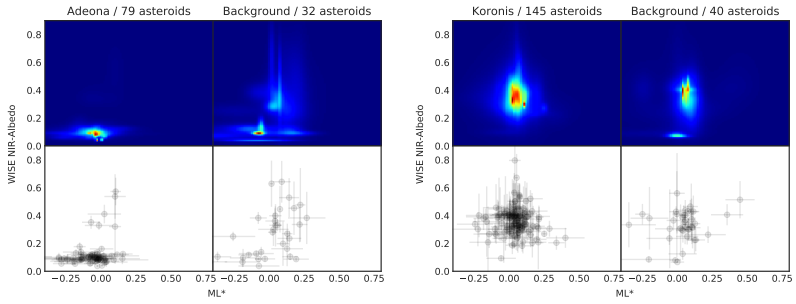

(g) Adeona (h) Koronis

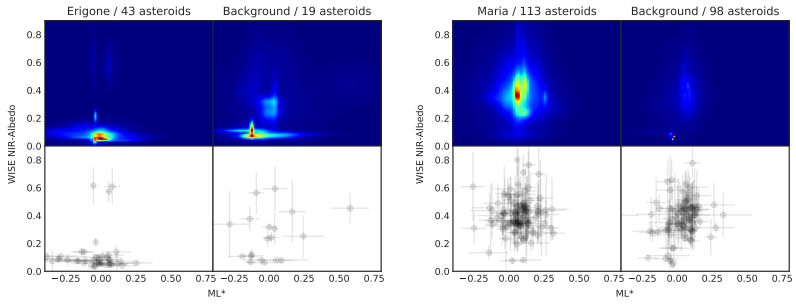

(i) Erigone (j) Maria

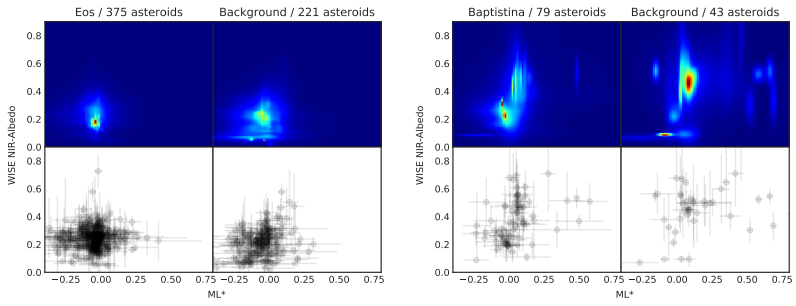

(k) Eos (l) Baptistina

Fig. C.1: Continued.

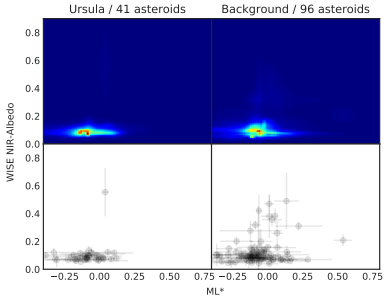

(m) Ursula

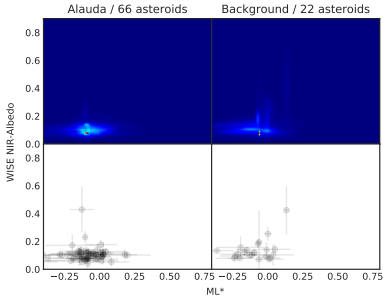

(n) Alauda

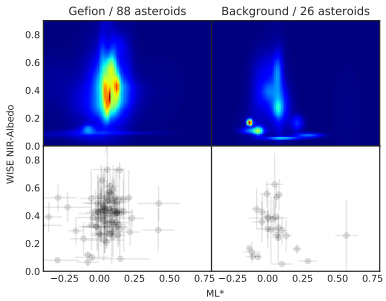

(o) Gefion

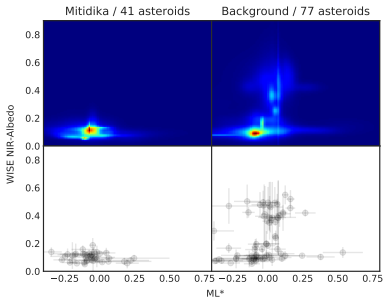

(p) Mitidika

Fig. C.1: Continued.

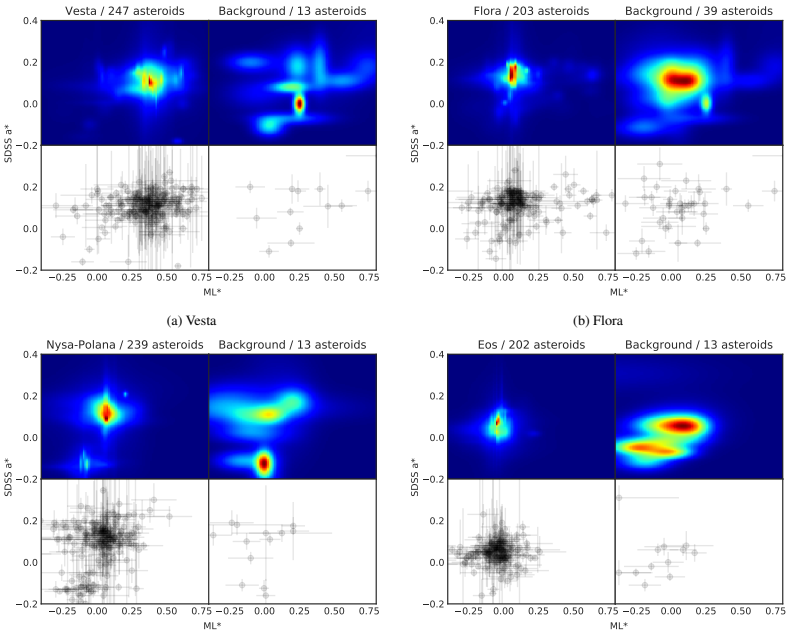

(a) Vesta (b) Flora

(c) Nysa–Polana (d) Eos

Fig. C.2: Asteroid families detected within the MOVIS catalog, with at least 40 coincidences with SDSS, and with a background of at least ten asteroids. In these plots we represent ML^* vs. a^*.

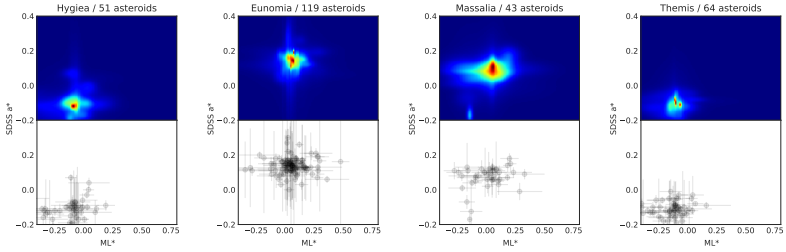

(a) Hygiea (b) Eunomia (c) Massalia (d) Themis

(e) Koronis (f) Maria (g) Baptistina (h) Gefion

Fig. C.3: ML^* vs. a^* for the asteroid families detected within the MOVIS catalog, with at least 40 coincidences with SDSS, and without a background (or the background that we defined had less than ten coincident asteroids with SDSS).

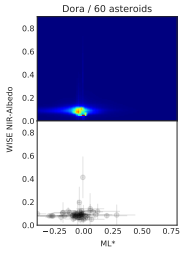

(a) Dora

Fig. C.4: ML^* vs. p_{NIR} for Dora, the only asteroid family in the MOVIS catalog with at least 40 coincidences with NEOWISE, and without a background (or the background that we defined had less than ten coincident asteroids with NEOWISE).

Figure 6.1: Acceptance letter from the editorial office of Astronomy & Astrophysics for the paper in the present Chapter: "Color study of asteroid families within the MOVIS catalog". Date of acceptance: 13-March-2018. DOI: https://doi.org/10.1051/0004-6361/201832780.

Subject: AA/2018/32780: paper sent to language-editor
From: aanda.paris@obspm.fr
Date: 15/03/18 09:38
To: damog@iac.es

15/03/2018

Mr David Morate

damog@iac.es

Our Ref. : AA/2018/32780

Dear Mr Morate,

I am pleased to inform you that your manuscript entitled "Color study of asteroid families within the MOVIS catalog" is now accepted for publication in Section 10. Planets and planetary systems of Astronomy and Astrophysics. The official date of acceptance is 13/03/2018.

The copyright of the paper is hereby transferred to ESO.

Your manuscript is being sent to an A&A English language Editor (LE) who will e-mail you the annotated paper once editing is completed. The time needed for language editing depends on the quality of the text, the length of the paper, and the workload of the LEs. The current average time for editing is 10 days.

With best wishes,

Jennifer Martin on behalf of
Thierry Forveille
A&A Editor in Chief

==========
NB: A&A now offers authors the possibility of being identified with non-Roman alphabets, such as Chinese, Japanese, Cyrillic characters.
http://www.aanda.org/index.php?option=com_content&task=view&id=954&Itemid=173

Chapter 7

Conclusions & future work

7.1 Conclusions

In the three papers that comprise this thesis work, we have analyzed the composition of several families in the main asteroid belt, using visible spectroscopy and near-infrared photometric data. Here, we list the main results obtained in the present work.

- The four low-inclination ($i < 8°$) primitive families in the inner main belt (i.e, Polana–Eulalia, Erigone, Sulamitis, and Clarissa) show spectra compatible with NEAs (101955) Bennu and (162173) Ryugu. Dynamically, according to Bottke et al. (2015), the probability of both asteroids originating in the Polana–Eulalia complex is higher than the probabilities regarding the rest of the families. In addition, according to compositional studies (de León et al. 2016; Pinilla-Alonso et al. 2016), Bennu and Ryugu have similar spectra to those of the Polana–Eulalia complex.

  The results obtained from the analysis of the spectra of asteroids in the Erigone, Sulamitis, and Clarissa families (Chapters 4 and 5) indicate that we cannot discard any of these families as possible sources of both NEAs. The three families present B-type spectra of asteroids compatible with Bennu, and C-type spectra of asteroids compatible with Ryugu.

  However, given the fraction of C- and B-types in the four low-inclination IMB primitive families, we can establish a compositional association: Bennu is more likely originated in the Polana–Eulalia or Clarissa families (higher percentage of B-types), while Ryugu might be originated in

any of the four families in the IMB (all of them show a C-type fraction ∼50%). The findings of both Hayabusa 2 and OSIRIS-REx missions will confirm their origin, and will provide "ground-truth" for the compositional results obtained in this thesis based in spectroscopy obtained from ground-based telescopes.

- We found traits of hydrated minerals on the surfaces of the asteroids in the Erigone and Sulamitis families from the presence of a broad and shallow absorption band, centered at 0.7 μm, in approximately half of both samples of primitive asteroids. This information will help to constrain the hydration levels of the different populations in the main belt, shedding light into the thermal history of the Solar System.

- We managed to develop an unsupervised algorithm for the detection of the absorption band at 0.7 μm related to hydrated minerals on the asteroid surfaces. This detection algorithm will be of great help for future analysis of other asteroid families or datasets with a high number of spectra, reducing the time of analysis and enhancing the results.

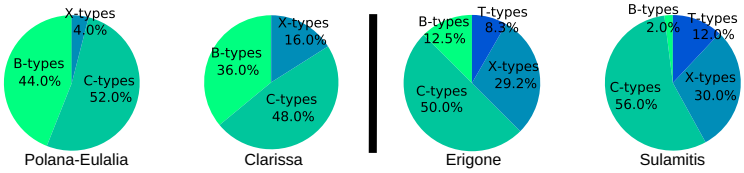

Figure 7.1: Pie chart representations of the taxonomical distribution of primitive classes for the four main primitive asteroid families located in the inner region of the main belt. The Polana–Eulalia complex and the Clarissa family (left) do not present the 0.7 μm band; Erigone and Sulamitis, the families on the right, do have the 0.7 μm band. The two groups have been separated to better visualize their differences.

- According to the visible spectral data obtained for the low-inclination primitive asteroid families in the inner main belt, we can differentiate two groups (see Fig. 7.1): the Polana-like group, showing homogeneous, featureless spectra in a continuum of slopes from blue to moderately red, and no 0.7 μm band (Polana–Eulalia complex and Clarissa family); and the Erigone-like group, which presents spectral diversity among primitive taxonomic classes and a majority of spectra with the 0.7 μm band associated to hydrated minerals on their surfaces (Erigone and Sulamitis collisional families). Up to now, there are no previous studies linking, in

a compositional way, two different families. The results presented here might be the first evidence of the common past of two asteroid collisional families.

- While the Erigone and the Sulamitis collisional families share similar properties regarding the spectra, family ages and visible albedos, we see that the Clarissa family has on average a slightly redder spectral slope and is significantly younger than the Polana–Eulalia complex. A possible explanation for these differences is the space weathering[1]. Laboratory experiments with carbonaceous chondritic material show that low albedo materials get bluer with space exposure age (Lantz et al. 2015, 2017). This has testable implications for Bennu and Ryugu, where older terrains would be expected to be bluer than younger surfaces.

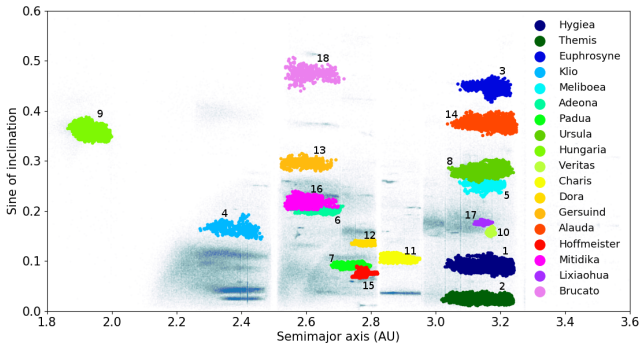

Figure 7.2: Distribution in the orbital parameter space (semimajor axis vs. sine of inclination) of the primitive families confirmed by MOVIS, plotted over the whole asteroid distribution of the main asteroid belt. It is easy to distinguish the Kirkwood gaps, associated to important resonances. Asteroid families near this regions are the most probable sources of primitive near-Earth asteroids. The families are numbered for a better identification within the figure: 1-Hygiea, 2-Themis, 3-Euphrosyne, 4-Klio, 5-Meliboea, 6-Adeona, 7-Padua, 8-Ursula, 9-Hungaria, 10-Veritas, 11-Charis, 12-Dora, 13-Gersuind, 14-Alauda, 15-Hoffmeister, 16-Mitidika, 17-Lixiaohua, and 18-Brucato.

[1]Space weathering refers to the surface alteration processes, i.e., ion irradiation and micrometeorite impacts, on atmosphere-less small bodies, that induce variations on the spectral properties of surface materials.

Table 7.1: Primitive families considered as possible sources of primitive NEAs according to their proximity to the main transport routes in the main belt. The semimajor axis, sine of inclination, and eccentricity, are the mean values for all the family members from Nesvorný et al. (2015).

Location	Family	Semimajor axis (A.U.)	Sine of inclination	Eccentricity
Inner belt	Klio	2.381	0.165	0.193
Mid belt	Gersuind	2.597	0.297	0.174
	Brucato	2.610	0.475	0.122
	Hoffmeister	2.783	0.077	0.048
	Dora	2.786	0.137	0.196
	Charis	2.878	0.105	0.051
Outer belt	Themis	3.139	0.024	0.149
	Ursula	3.144	0.280	0.083
	Hygiea	3.153	0.090	0.130
	Euphrosyne	3.158	0.448	0.196
	Alauda	3.165	0.376	0.086

- The analysis of the MOVIS database has provided a statistical way to qualitatively confirm[2], at least, 16 more primitive families throughout the main belt, which had not been spectroscopically addressed by previous studies[3], out of the 18 shown in Fig. 7.2. Since asteroid families are preferred over individual asteroids as possible sources of NEAs, the primitive families near the most prominent resonances would be the most probable sources of primitive NEAs. The IMB will be the most probable source, followed by the mid and outer regions (Bottke et al. 2002a). In Table 7.1 we propose, out of the 18 primitive families shown in Fig. 7.2, the most probable sources of NEAs according to their proximity to resonances in the main belt.

In addition to the confirmation of primitive asteroid families, the near-infrared data within the MOVIS catalog has provided two promising results that will need further study:

- The Ino family, which presents an anomalous ML^* distribution, does not match any of the proposed theoretical compositions in Morate et al. (2018b), neither is similar to the distribution of any other family. Given the results of the Kolmogorov–Smirnov test performed on its members,

[2]These families were already identified as primitive due to the spectrum of their parent body or the mean albedo of the family.

[3]Themis and Hygiea families have already been studied by means of spectroscopy (see Florczak et al. 1999 for Themis and Mothé-Diniz et al. 2001 for Hygiea).

this family could be a V-type candidate. The discovery of V-type asteroids outside the Vesta family in the middle and outer part of the asteroid belt have challenged current models of temperature variations in the early Solar System, suggesting the presence of several large bodies that suffered from differentiation. Up to now, there are only 4 published spectra of such asteroids (Ieva et al. 2016), and there are no other known basaltic families in the main belt apart from that of Vesta. Thus, the existence of a V-type family at ~ 2.76 A.U. would be a major discovery. However, we have to take into account that this result is based on a small amount of data (only 11 objects), an so, it needs for a more detailed study.

- The Baptistina collisional family has been previously addressed to be special to some degree, since it presents different taxonomies on its observed spectra. However, this result, from spectroscopy alone, was obtained from just 16 asteroids (Reddy et al. 2011). Combining MOVIS data with infrared albedos from NEOWISE, we confirm the presence of a two-cluster distribution within the ML^* vs. p_{NIR} space. There are several interesting explanations for this. The most compelling possibility would be that Baptistina is the result of the breakup of a differentiated parent body. This would be the first time that an asteroid family presents traits of different compositions among its members, indicating that the parent body presented several layers of different materials before the collision in which the family was formed.

7.2 Future work

The work presented in this thesis has provided insights on asteroid family composition and on the relationships that connect asteroid families and near-Earth asteroids, as well as the potential links that might exist between families. At the same time, this study has left newly opened questions that need to be addressed in the near future:

- As mentioned in Chapter 1, four additional primitive families in the inner main belt were defined during the period in which this thesis work was carried out: Klio, Chaldaea, Svea, and Chimaera. Their primitive status has been inferred from spectroscopy of the biggest member and/or photometric data of its members (Nesvorný et al. 2015). These high-inclination families ($i > 8°$) have a similar number of asteroids to that of Sulamitis and Clarissa (the small low-inclination primitive families studied in the present work), and they are also located very close to the 3:1 mean

motion resonance and the ν_6 secular resonance (even closer than some of the families of the low-inclination group). This means that these families are also possible sources of primitive NEAs (101955) Bennu and (162173) Ryugu.

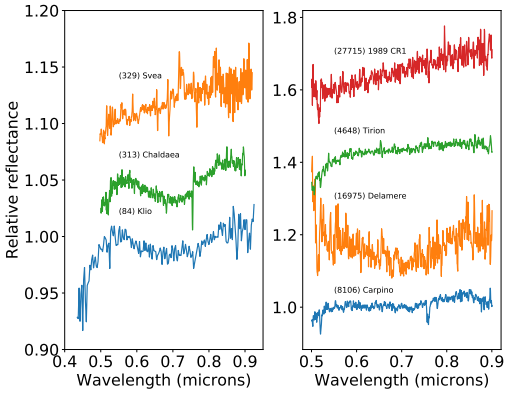

Figure 7.3: Reflectance spectra of asteroids from the inner main belt high-inclination families, with offsets in the vertical direction to improve visualization. Left panel: spectra of three of the parent bodies: (84) Klio from SMASS (Xu et al. 1995), (329) Svea from S3OS2 (Lazzaro et al. 2004), and (313) Chaldaea (from our GTC program). Right panel: preliminary reduction of some observed family members within the GTC program. The top two objects belong to the Klio family, and the lower two belong to the Chaldaea family. It is easy to recognize the absorption band centered at 0.7 μm in some of these spectra.

In addition, the spectra of some of their family members present the hydration signature at 0.7 μm. Thus, the study of these objects will also help to understand the distribution of the aqueous altered minerals on the inner main belt. Two observational programs were awarded time with the GTC to observe asteroids from these families (see Fig. 7.3). A total of 80 spectra have been obtained: 30 Klio, 19 Chaldaea, 23 Chimaera, and 8 Svea. Data are under reduction.

- The few visible spectra available for the identified primitive families in the MMB show, in several cases, the presence of the 0.7 μm band. Taking into account the results regarding the aqueous alteration that we presented in this thesis, we might expect a similar behavior for these families. These

families need to be spectroscopically addressed in a similar way to the ones studied in this thesis, since they might also be sources of NEAs. In addition, the study of these families will provide information on the variation of the primitive asteroids characteristics depending on their distance to the Sun. Rivkin (2012), using SDSS visible photometry, showed that the fraction of hydrated asteroids is higher in the mid belt than in the inner or outer regions (see Fig. 7.4). Thus, we expect a slightly higher percentage from spectroscopy (compared to the IMB results from this thesis) of primitive asteroids in the mid belt to confirm this result. At the moment, there is an observational program currently ongoing in the GTC to obtain data in the spectral range 0.5–0.9 μm of asteroids in three primitive families located in the mid main belt: Hoffmeister, Nemesis, and Padua.

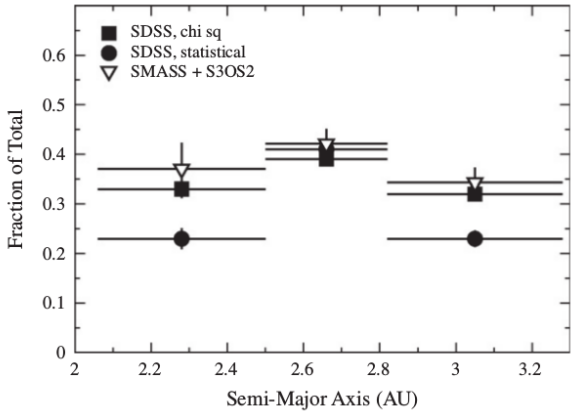

Figure 7.4: Variation of the total fraction of hydrated objects in the main belt with the semimajor axis, along with the variation seen in the combined SMASS and S3OS2 surveys. Horizonal error bars show the width of each bin, while vertical error bars show the 1-σ uncertainty in each measurement. Extracted from Rivkin (2012).

- As pointed out in Sect. 7.1, the results of the analysis of the MOVIS catalog in Chapter 6 regarding the Baptistina family is a preliminary finding, which should be addressed either by dedicated spectroscopic surveys, or by a higher statistical significance using spectrophotometric data from all-sky surveys, such as the J-PLUS survey (Javalambre Photometric

Local Universe Survey). J-PLUS is being conducted in the Observatorio Astrofísico de Javalambre (Teruel, Spain) with the T80 (a 0.80 m telescope). It is designed to obtain photometric data in 12 broad, intermediate, and narrow band filters, in the spectral range 0.35–1.0 μm, with a field of view of approximately 1.7 square degrees. Our group is part of this collaboration, and toghether with the *Grupo de Pequenos Corpos do Sistema Solar*, in the *Observatório Nacional* (Rio de Janeiro, Brazil), we are exploiting the data that the survey is producing to obtain a spectrophotometric catalog of Solar System objects, in a similar way as we did with the VISTA-VHS survey.

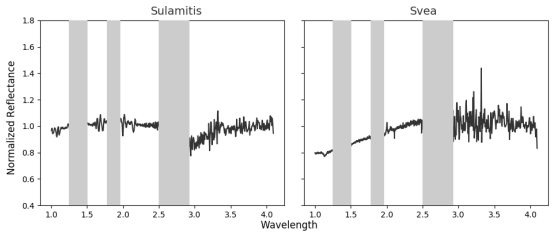

Figure 7.5: Spectra of (752) Sulamitis and (329) Svea obtained with the 3.0 m NASA IRTF. The grey regions in the figure represent the atmospheric absorption bands, where spectral data is not useful. There is a clear absorption band in the (752) Sulamitis spectrum, indicative of hydrated minerals in the asteroid surface, as expected, since the visible spectrum presents the 0.7 μm absorption band. The spectra of (329) Svea, on the right, does not show this 3.0 μm absorption band, neither presents the 0.7 μm band on its visible spectrum (see Fig. 7.3, left). Thus, it is unlikely for its members to show this feature in a significant proportion.

- In Sect. 1.4, we emphasized the importance of mapping the frequency of hydrated minerals on asteroids' surfaces through the main belt. The principal indicator of hydration is the absorption band centered near 3μm. The results of this thesis on the spectral analysis of the primitive families of the IMB point to the presence of this absorption band in a significant fraction of their members, mainly in the Erigone and Sulamitis families. We started an observational program with the 3.0 m NASA IRTF with the goal of studying the presence of hydrated minerals or water ice on the surface of the largest members of the eight most relevant primitive asteroid families in the IMB, testing how usual is the presence of OH/H_2O materials on the surface of these objects. This can be done by detecting and characterizing an absorption band centered around $\sim 2.7\mu$m, typi-

cally due to an OH absorption, or the H_2O bands near 2.9 and 3.1 μm. In Fig. 7.5 we show the first results of this observational program. The program aims to observe, at least, the parent bodies of the eight primitive families mentioned in this work: the Polana–Eulalia complex, and the Erigone, Sulamitis, Clarissa, Klio, Chaldaea, Svea, and Chimaera families. This information will help to understand the thermal history of the Solar System.

As a finishing remark to the present work, the James Webb Space Telescope, the next great space observatory, will be a powerful tool for the detailed study of primitive compositions in small bodies of the Solar System. This 6.0 m-class telescope, which will be located at the L2 Lagrange point of Earth's orbit, has been scheduled for launch on the year 2020. The science instruments, prepared to obtain spectroscopic and photometric data in the near- and mid-infrared spectral range (1.0–25 μm) will provide a wealth of information about the Solar System, planets orbiting other stars, distant stars and galaxies. This space telescope will be a major step in the study of the hydration features in the infrared spectra of asteroids, as it will significantly improve the data quality at that wavelength region. We should be aware of the potential of this telescope and take advantage of its instrumentation. Spectroscopic observations at these wavelengths with a space based telescope might even open new windows on the study of small bodies of the Solar System.

Bibliography

Abe, M., Kawakami, K., Hasegawa, S., et al. 2008, in Lunar and Planetary Science Conference, Vol. 39, Lunar and Planetary Science Conference, 1594

Binzel, R. P., & Xu, S. 1993, Science, 260, 186

Binzel, R. P., DeMeo, F. E., Burt, B. J., et al. 2015, Icarus, 256, 22

Bobrovnikoff, N. T. 1929, Lick Observatory Bulletin, 14, 18

Bottke, W. F., Morbidelli, A., Jedicke, R., et al. 2002a, Icarus, 156, 399

Bottke, W. F., Vokrouhlický, D., Walsh, K. J., et al. 2015, Icarus, 247, 191

Bottke, Jr., W. F., Vokrouhlický, D., Rubincam, D. P., & Broz, M. 2002b, The Effect of Yarkovsky Thermal Forces on the Dynamical Evolution of Asteroids and Meteoroids, ed. W. F. Bottke, Jr., A. Cellino, P. Paolicchi, & R. P. Binzel, 395–408

Bus, S. J., & Binzel, R. P. 2002, Icarus, 158, 146

Campins, H., de León, J., Morbidelli, A., et al. 2013, AJ, 146, 26

Campins, H., Morbidelli, A., Tsiganis, K., et al. 2010a, ApJ, 721, L53

Campins, H., Hargrove, K., Pinilla-Alonso, N., et al. 2010b, Nature, 464, 1320

Carvano, J. M., Hasselmann, P. H., Lazzaro, D., & Mothé-Diniz, T. 2010, A&A, 510, A43

Carvano, J. M., Mothé-Diniz, T., & Lazzaro, D. 2003, Icarus, 161, 356

Chapman, C. R., Morrison, D., & Zellner, B. 1975, Icarus, 25, 104

Cheng, A. F. 2002, Near Earth Asteroid Rendezvous: Mission Summary, ed. W. F. Bottke, Jr., A. Cellino, P. Paolicchi, & R. P. Binzel, 351–366

Clark, B. E., Ziffer, J., Nesvorny, D., et al. 2010, Journal of Geophysical Research (Planets), 115, 6005

Clark, B. E., Binzel, R. P., Howell, E. S., et al. 2011, Icarus, 216, 462

Cloutis, E. A., Hudon, P., Hiroi, T., Gaffey, M. J., & Mann, P. 2011, Icarus, 216, 309

Cunningham, C. 2016, Early Investigations of Ceres and the Discovery of Pallas

de León, J., Licandro, J., & Pinilla-Alonso, N. 2017, The Diverse Population of Small Bodies of the Solar System, 55

de León, J., Pinilla-Alonso, N., Campins, H., Licandro, J., & Marzo, G. A. 2012, Icarus, 218, 196

de León, J., Pinilla-Alonso, N., Delbo, M., et al. 2016, Icarus, 266, 57

De Prá, M. 2017, PhD thesis, Observatório Nacional, Rio de Janeiro

De Prá, M., Pinilla-Alonso, N., Carvano, J. M., et al. 2017, Icarus", doi:10.1016/j.icarus.2017.11.012

DeMeo, F. E., Alexander, C. M. O., Walsh, K. J., Chapman, C. R., & Binzel, R. P. 2015, The Compositional Structure of the Asteroid Belt, ed. P. Michel, F. E. DeMeo, & W. F. Bottke, 13–41

DeMeo, F. E., Binzel, R. P., Slivan, S. M., & Bus, S. J. 2009, Icarus, 202, 160

DeMeo, F. E., & Carry, B. 2013, Icarus, 226, 723

Florczak, M., Lazzaro, D., Mothé-Diniz, T., Angeli, C. A., & Betzler, A. S. 1999, A&AS, 134, 463

Fornasier, S., Lantz, C., Barucci, M. A., & Lazzarin, M. 2014, Icarus, 233, 163

Fulchignoni, M., Birlan, M., & Antonietta Barucci, M. 2000, Icarus, 146, 204

Hergenrother, C. W., Nolan, M. C., Binzel, R. P., et al. 2013, Icarus, 226, 663

Hirayama, K. 1918, AJ, 31, 185

—. 1923, Japan J. Astron. Geophys., 1, 55

—. 1928, Japan J. Astron. Geophys., 5, 137

Ieva, S., Dotto, E., Lazzaro, D., et al. 2016, MNRAS, 455, 2871

Kirkwood, D. 1867, Meteoric astronomy: a treatise on shooting-stars, fireballs, and aerolites.

Lantz, C., Brunetto, R., Barucci, M. A., et al. 2017, Icarus, 285, 43

—. 2015, A&A, 577, A41

Lauretta, D. S., Drake, M. J., Benzel, R. P., et al. 2010, Meteoritics and Planetary Science Supplement, 73, 5153

Lauretta, D. S., Balram-Knutson, S. S., Beshore, E., et al. 2017, Space Sci. Rev., 212, 925

Lazzaro, D., Angeli, C. A., Carvano, J. M., et al. 2004, Icarus, 172, 179

Licandro, J., Campins, H., Kelley, M., et al. 2011, A&A, 525, A34

McCord, T. B., Adams, J. B., & Johnson, T. V. 1970, Science, 168, 1445

McMahon, R. G., Banerji, M., Gonzalez, E., et al. 2013, The Messenger, 154, 35

McSween, Jr., H. Y. 1999, Meteorites and their Parent Planets, 322

Milani, A., & Knezevic, Z. 1990, Celestial Mechanics and Dynamical Astronomy, 49, 347

—. 1992, Icarus, 98, 211

Morate, D., de León, J., De Prá, M., et al. 2018a, A&A, 610, A25

—. 2016, A&A, 586, A129

Morate, D., Licandro, J., Popescu, M., & de León, J. 2018b, Accepted for publication in A&A

Mothé-Diniz, T., di Martino, M., Bendjoya, P., Doressoundiram, A., & Migliorini, F. 2001, Icarus, 152, 117

Nesvorny, D. 2012, NASA Planetary Data System, 189

Nesvorný, D., Brož, M., & Carruba, V. 2015, Identification and Dynamical Properties of Asteroid Families, ed. P. Michel, F. E. DeMeo, & W. F. Bottke, 297–321

Opik, E. J. 1951, Proc. R. Irish Acad. Sect. A, vol. 54, p. 165-199 (1951)., 54, 165

Pinilla-Alonso, N., de León, J., Walsh, K. J., et al. 2016, Icarus, 274, 231

Popescu, M., Birlan, M., & Nedelcu, D. A. 2012, A&A, 544, A130

Popescu, M., Licandro, J., Morate, D., et al. 2016, A&A, 591, A115

Reddy, V., Carvano, J. M., Lazzaro, D., et al. 2011, Icarus, 216, 184

Rivkin, A. S. 2012, Icarus, 221, 744

Rivkin, A. S., Thomas, C. A., Howell, E. S., & Emery, J. P. 2015, AJ, 150, 198

Russell, C. T., McSween, H. Y., Jaumann, R., & Raymond, C. A. 2015, The Dawn Mission to Vesta and Ceres, ed. P. Michel, F. E. DeMeo, & W. F. Bottke, 419–432

Sutherland, W., Emerson, J., Dalton, G., et al. 2015, A&A, 575, A25

Takir, D., & Emery, J. P. 2012, Icarus, 219, 641

Tholen, D. J. 1984, PhD thesis, University of Arizona, Tucson

Tsuda, Y., Yoshikawa, M., Abe, M., Minamino, H., & Nakazawa, S. 2013, Acta Astronautica, 91, 356

Vilas, F. 2008, AJ, 135, 1101

Vilas, F., & Gaffey, M. J. 1989, Science, 246, 790

Walsh, K. J., Delbó, M., Bottke, W. F., Vokrouhlický, D., & Lauretta, D. S. 2013, Icarus, 225, 283

Wetherill, G. W. 1976, Geochim. Cosmochim. Acta, 40, 1297

—. 1979, Icarus, 37, 96

Wisdom, J. 1983, Icarus, 56, 51

Xu, S., Binzel, R. P., Burbine, T. H., & Bus, S. J. 1995, Icarus, 115, 1

York, D. G., Adelman, J., Anderson, Jr., J. E., et al. 2000, AJ, 120, 1579

Zappala, V., & Cellino, A. 1994, in IAU Symposium, Vol. 160, Asteroids, Comets, Meteors 1993, ed. A. Milani, M. di Martino, & A. Cellino, 395

Zappala, V., Cellino, A., Farinella, P., & Knezevic, Z. 1990, AJ, 100, 2030

Zellner, B. 1973, in BAAS, Vol. 5, Bulletin of the American Astronomical Society, 388

Zellner, B., Tholen, D. J., & Tedesco, E. F. 1985, Icarus, 61, 355